INVESTIGATION OF TEMPERATURE PROFILE IN HIGH TEMPERATURE
PEM FUEL CELL

A THESIS SUBMITTED TO
THE GRADUATE SCHOOL OF NATURAL AND APPLIED SCIENCES
OF
MIDDLE EAST TECHNICAL UNIVERSITY

BY

DİLARA GÜLÇİN ÇAĞLAYAN

IN PARTIAL FULFILLMENT OF THE REQUIREMENTS
FOR
THE DEGREE OF MASTER OF SCIENCE
IN
CHEMICAL ENGINEERING

JUNE 2016

Approval of the thesis:

INVESTIGATION OF TEMPERATURE PROFILE IN HIGH TEMPERATURE PEM FUEL CELL

submitted by **DİLARA GÜLÇİN ÇAĞLAYAN** in partial fulfillment of the requirements for the degree of **Master of Science in Chemical Engineering Department, Middle East Technical University** by,

Prof. Dr. Gülbin Dural Ünver
Dean, Graduate School of **Natural and Applied Sciences**   _____

Prof. Dr. Halil Kalıpçılar
Head of Department, **Chemical Engineering**   _____

Prof. Dr. İnci Eroğlu
Supervisor, **Chemical Engineering Dept., METU**   _____

Assoc. Prof. Dr. Yılser Devrim
Co-supervisor, **Energy Systems Eng. Dept., Atılım Uni.**   _____

Examining Committee Members:

Assoc. Prof. Dr. Görkem Külah
Chemical Engineering Dept., METU   _____

Prof. Dr. İnci Eroğlu
Chemical Engineering Dept., METU   _____

Assoc. Prof. Yılser Devrim
Energy Systems Engineering Dept., Atılım University   _____

Assoc. Prof. Dr. Serkan Kıncal
Chemical Engineering Dept., METU   _____

Asst. Prof. Dr. Berker Fıçıcılar
Chemical Engineering Dept., 19 Mayıs University   _____

Date: June 23, 2016

I hereby declare that all information in this document has been obtained and presented in accordance with academic rules and ethical conduct. I also declare that, as required by these rules and conduct, I have fully cited and referenced all material and results that are not original to this work.

Name, Last name: Dilara Gülçin ÇAĞLAYAN

Signature　　　　:

ABSTRACT

**INVESTIGATION OF TEMPERATURE PROFILE IN HIGH
TEMPERATURE PEM FUEL CELL**

Çağlayan, Dilara Gülçin

M.Sc., Department of Chemical Engineering

Supervisor: Prof. Dr. İnci Eroğlu

Co-supervisor: Assoc. Prof. Dr. Yılser Devrim

June 2016, 104 pages

High temperature polymer electrolyte membrane fuel cells (HT-PEMFC) are promising alternative energy sources for the future. As an advantageous tool in the design of a system, modeling requires less time compared to the experiments as well as its low cost. This study includes both isothermal and non-isothermal three-dimensional mathematical models for a HT-PEMFC having an active area of 25 cm^2. Governing equations are solved by using Comsol Multiphysics 5.0 "Batteries & Fuel Cells" module, which is a commercial software package that solves partial differential equations by using finite element method.

Temperature has a crucial role in the operation of HT-PEMFC because of the exothermic reaction taking place at the catalyst layer. Influence of the temperature on the performance is studied for a single channel and triple mixed serpentine geometry with an isothermal model. It is seen that the fuel cell performance is

enhanced as the operation temperature increases due to enhanced reaction kinetics and increased proton conductivity of PBI membrane. Higher proton conductivity yields in a decrease in the ohmic losses of the cell.

The temperature distribution within the cell is obtained with a non-isothermal three-dimensional model. There is an increase in the temperature approximately 0.31 ^{o}C at the operation voltage of 0.45 V, this value lowers at higher operation voltages. It is concluded that exothermic reaction in the cathode catalyst layer does not have a significant effect on the temperature; therefore, isothermal assumption is valid for the system.

Keywords: HT-PEM fuel cells, Fuel cell modeling, Temperature distribution, Comsol Multiphysics

ÖZ

YÜKSEK SICAKLIK PEM YAKIT PİLİNİN SICAKLIK PROFİLİNİN ARAŞTIRILMASI

Çağlayan, Dilara Gülçin

Yüksek Lisans, Kimya Mühendisliği Bölümü

Tez Yöneticisi: Prof. Dr. İnci Eroğlu

Ortak Tez Yöneticisi: Doç. Dr. Yılser Devrim

Haziran 2016, 104 sayfa

Yüksek sıcaklık polimer elektrolit membran yakıt pilleri (HT-PEMFC) gelecek için umut vaad eden alternatif enerji kaynaklarıdır. Tasarım aşamasında faydalı bir araç olan modelleme, deneylerle karşılaştırıldığında düşük maliyetinin yanısıra daha az zaman gerektirir. Bu çalışma 25 cm^2 aktif alana sahip bir HT-PEM yakıt pilinin hem eşsıcaklıklı hem de eşsıcaklıklı olmayan üç boyutlu matematiksel modellerini içermektedir. Korunum denklemleri, kısmi diferansiyel denklemlerin sonlu element metodunu kullanan ticari bir paket program olan Comsol Multiphysics 5.0 "Batteries & Fuel Cells" modülü ile çözülmüştür.

Yakıt pilinin katalizör tabakasında gerçekleşen egzotermik reaksiyon sayesinde HT-PEM yakıt pillerinin operasyonunda sıcaklık çok önemli bir role sahiptir. Sıcaklığın performans üzerindeki etkisi eşsıcaklıklı tekli ve üçlü serpantin akış kanalına sahip

modellerle incelenmiştir.Artan reaksiyon kinetiği ve PBI membranın proton iletkenliği sayesinde, operasyon sıcaklığı arttıkça performansta iyileşmeler görülmüştür. Yüksek proton iletkenliği hücredeki ohmik kayıpların azalmasına sebep olmaktadır.

Hücre içindeki sıcaklık dağılımı, eşsıcaklıklı olmayan üç boyutlu bir model ile elde edilmiştir. 0.45 V operasyon geriliminde sıcaklıkta 0.31 ^{o}C artış görülmüştür, bu değer gerilim daha yüksek olduğunda azalır. Katot katalizör tabakasındaki egzotermik reaksiyonun sıcaklık üzerinde büyük bir etkisinin olmadığı ve eşsıcaklıklı varsayımının sistem için doğru olduğu sonucuna varılmıştır.

Anahtar kelimeler: Yüksek sıcaklık PEM yakıt pilleri, yakıt pili modellemesi, sıcaklık dağılımı, Comsol Multiphysics

Faber est suae quisque fortunae,

To those who are the artisans of their own fortune,

ACKNOWLEDGMENTS

TABLE OF CONTENTS

LIST OF TABLES

TABLES

LIST OF FIGURES

FIGURES

xviii

LIST OF SYMBOLS

Symbol	Definition	Unit
C	Concentration	mol m^{-3}
C$_p$	Specific heat	J kg^{-1} K^{-1}
D$_{ij}$	Binary diffusion coefficient	m^2 s^{-1}
E	Cell voltage	V
E$_a$	Proton conducting activation energy	J mol^{-1} K^{-1}
F	Faraday's constant	96485 C
I	Current	A
i	Transfer current density	A m^{-2}
k	Thermal conductivity	W m^{-1} K^{-1}
k$_p$	Permeability	m^2
M	Molar mass	kg mol^{-1}
N	Mass flux rate	kg m^{-2} s^{-1}
P	Pressure	Pa
R	Universal gas constant	J K^{-1} mol^{-1}
R$_{ohm}$	Ohmic resistance	m^2 S^{-1}
S$_T$	Source term	J m^{-2} s^{-1}
T	Temperature	K
u	Velocity	m s^{-1}
U$_o$	Thermodynamic equilibrium potential	V
x	Molar fraction	-
w	Mass fraction	-

Greek letters

α	Transfer coefficient	-
ε	Porosity	-
∅	Phase potential	V
μ	Dynamic viscosity	$kg\ m^{-1}\ s^{-1}$
η	Overpotential	V
κ	Proton conductivity	$S\ m^{-1}$
ρ	Fluid density	$kg\ m^{-3}$

Subscripts and superscripts

a: Anode

c: Cathode

e: Electrolyte phase

eff: Effective

ex: Exchange

i, j: Species i,j

ref: Reference conditions

s: Solid phase

LIST OF ABBREVIATIONS

1D	One-dimensional
2D	Two-dimensional
3D	Three-dimensional
AFC	Alkaline fuel cell
CFD	Computational fluid dynamics
DMFC	Direct methanol fuel cell
GDL	Gas diffusion layer
HT-PEMFC	High Temperature PEM fuel cell
I	Isothermal
MEA	Membrane electrode assembly
MCFC	Molten carbonate fuel cell
NI	Non-isothermal
OCV	Open circuit voltage
PAFC	Phosphoric acid fuel cell
PBI	Polybenzimidazole
PEMFC	Polymer electrolyte membrane fuel cell
PFSA	Perfluorosulfonic acid
SOFC	Solid oxide fuel cell

CHAPTER 1

1. INTRODUCTION

Energy is an essential necessity for the human being. Increasing population and the technological developments make the energy requirement increase year by year. Energy is a necessity in every aspect of life such as domestic life, transportation, industrial processes and so on. Diminution of the fossil fuels and increase in the pollutant emissions divert the researchers' attention seeking alternatives for clean and renewable energy resources. Figure 1.1 shows the contribution of individual energy sources on the world electricity production. As it is seen from the figure, the predicted demand for total energy increases year by year as well as the contribution of renewable energy sources.
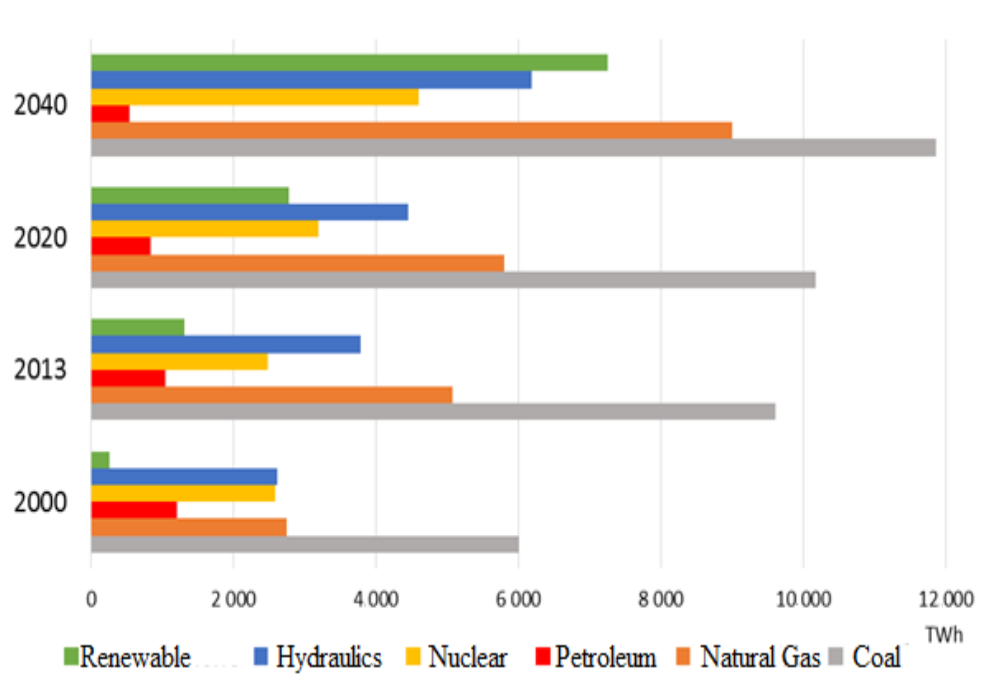
Figure 1.1 Contribution of Energy Sources on Electricity Production (2000-2040) [1]

Hydrogen is the most promising alternative energy carrier as a secondary form of the energy. It does not exist freely in the nature, yet it can be produced from primary energy sources. Energy yield of the hydrogen is 122 kJ/g, which is approximately 3 times higher than the hydrocarbon fuels. As a clean fuel because of its carbon free content, using hydrogen in fuel cells is the most promising way attracting researchers' attention to produce electricity.

Fuel cells are electrochemical devices that directly and continuously convert chemical energy content of the feed into the direct current electricity as long as the feed is supplied. When they are compared to the internal combustion engines, fuel cells have higher efficiency because of the direct conversion of the chemical energy into electricity. They have fast response to power demand, long cell and stack life, low corrosion, no moving parts and low cost. In addition, they are quiet and considered as "zero emission engine" because they only produce electrical power, water and heat.

The first observation and the demonstration of fuel cells were made in 1930's. Then in 1842, Sir William Grove developed the first fuel cell producing electricity with the combination of hydrogen and oxygen with the help of platinum electrode and sulfuric acid electrolyte. Grove named this fuel cell as gaseous voltaic battery. Despite the invention on fuel cell was in 1939, the first construction and evaluation of a 5 kW fuel cell stack was completed in 1952 by an English engineer, Francis T. Bacon. Figure 1.2 shows the fuel cell history timeline [2].
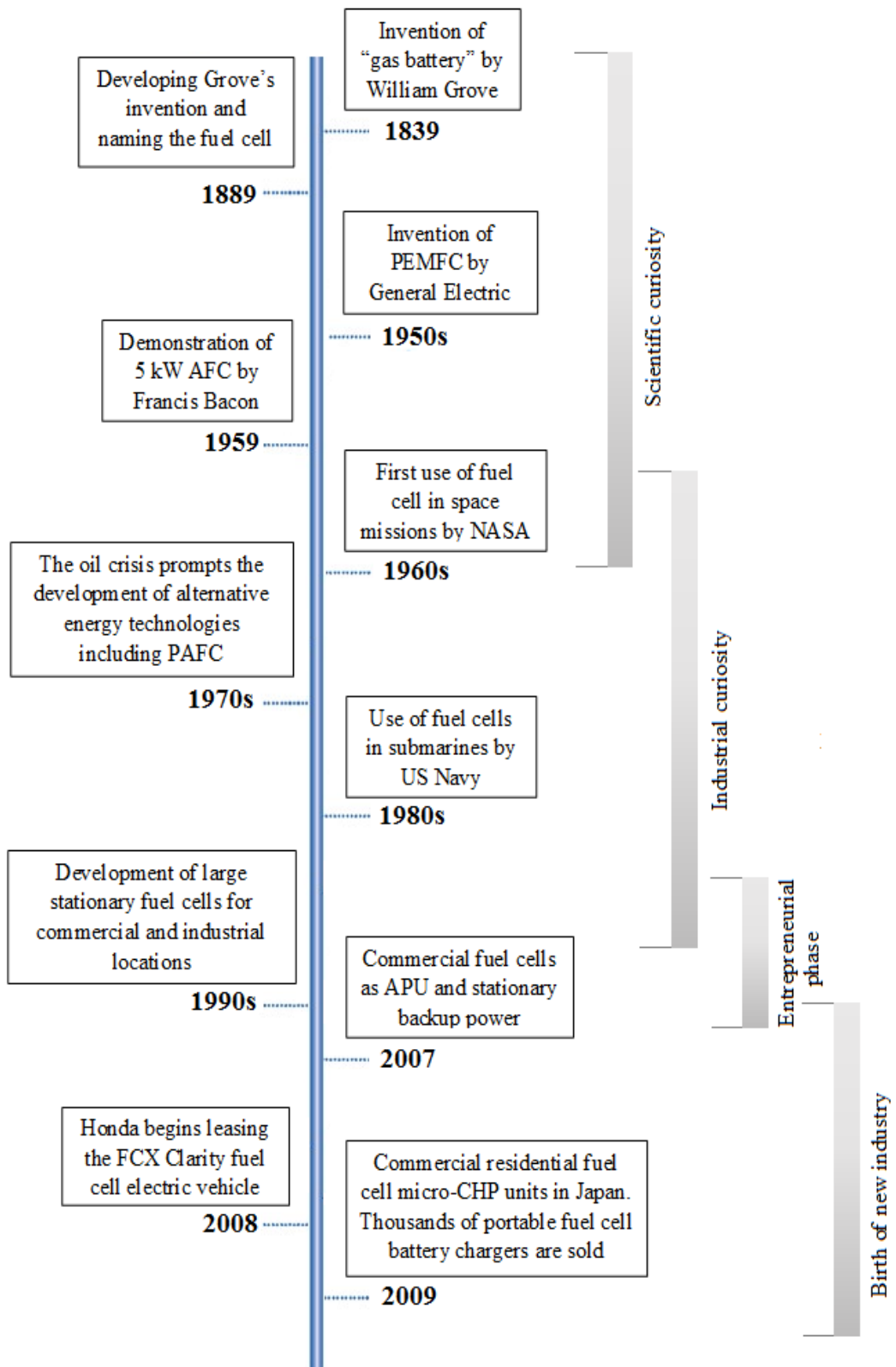
Figure 1.2 Fuel Cell History Timeline

Fuel cells are categorized by the electrolyte type included in the system. The electrolyte determines the characteristics of the operation such as operation

3

temperature, feed type and so on. Solid oxide fuel cell (SOFC), molten carbonate fuel cell (MCFC), alkaline fuel cell (AFC), Phosphoric acid fuel cell (PAFC), direct methanol fuel cell (DMFC) and Polymer electrolyte membrane fuel cell (PEMFC) are some types of fuel cells.

Fuel cells consists of components which have specific roles for the system. These are flow channels, gas diffusion layers, catalyst layers and membrane. Oxidation and reduction reactions of reactants take place at the catalyst layers. Typically, oxidation in the anode side and reduction in the cathode side. The protons generated in the redox reaction pass through the membrane; whereas, electrons pass through an external circuit to complete the system. The catalyst layers are followed by gas diffusion layers, which have a role in the homogeneous dispersion of the reactants through the surface. There are gas flow channels, in which the reactant gases flow, in contact with the gas diffusion layers.

PEM Fuel Cells include a polymer electrolyte acting as an insulator for the electrons and conductor for the protons. The electrolyte characteristics highly depends on the operation conditions such as the operation temperature and pressure. PEM Fuel Cells can be classified into two groups according to their operation temperature: PEM Fuel Cells operating between 50-100 ^{o}C and High Temperature PEM Fuel Cells (HT-PEMFC) operating between 100-200 ^{o}C. PEMFCs include a perfluorosulfonic acid (PFSA) polymer membrane electrolyte acting as an electron insulator and proton conductor Nafion® produced by DuPont has become an industrial standard for the temperature range of 50-100 ^{o}C due to its high ionic conductivity, chemical stability, mechanical strength and flexibility. However, these properties of Nafion® are only valid at highly hydrated states and temperatures up to 80 ^{o}C. The ionic conductivity of the Nafion® strongly depends on the humidity; in other words, lower humidity yields to lower ionic conductivity in the membrane. Therefore, water and thermal management have become crucial in the PEM fuel cells operating at low temperatures. The system must be well humidified; on the other hand, excess humidification may cause flooding which is not desired. CO tolerance of the fuel cell is comparably low. Few amount of CO content in the feed stream causes a significant decrease in the fuel cell performance. Therefore,

4

alternative membranes have been investigated to overcome the drawbacks of low temperature operation.

HT-PEMFCs include polybenzimidazole (PBI) membranes which have good mechanical strength, high chemical and thermal stability at high temperatures. Although the ionic conductivity of PBI membranes are low, it increases when they are doped with a strong acid such as sulfuric or phosphoric acid. The material used for the sealing of HT-PEMFC is Viton, which is one of the most widely used elastomers. High temperature operation has the advantage of faster reaction kinetics with the presence of single phase. As the operation temperature increases, the tolerance to the CO increases. This advantage is more pronounced when the fuel cell system is combined with a reformer, since reformate gas contains 2-3% CO. Recovery of waste heat in the high temperature operation is much simpler when it is compared with the low temperature because of the higher temperature gradient. On the other hand, material degradation becomes more significant as the temperature increases. The time required to achieve steady operation is higher as opposed to the low temperature operation.

Modeling of fuel cells has become important recently, since it is able to explicate all the mass, momentum and energy transport mechanism taking place within the system. In addition, the fundamentals of the transport phenomena occurring within the system is revealed by the modeling in such cases where it is not possible to identify them by the experiments. With an appropriate model, it is possible to design and optimize the system with less experiments required. Moreover, the behavior of the system to the alterations related to the operation conditions can be foreseen with the help of modeling.

The aim of this thesis is to develop the temperature profile in a HT-PEMFC by using relevant three-dimensional model that elucidates the transport phenomena taking place within the system. The HT-PEMFC which is aimed to be modeled has both for commercial membrane produced by Danish Power Systems and the developing membrane produced by FCRC research group. The active area of HT-PEMFC is 25 cm^2 including phosphoric acid doped PBI membrane. In addition to the temperature profile, the sole effect of key parameters on the fuel cell performance is aimed to be

investigated, such as operation temperature, pressure, and flow rate of reactants. With the help of the non-isothermal model results, an appropriate cooling strategy is aimed to be designed in order to have better fuel cell performance with the optimum operation conditions.

CHAPTER 2

2. HIGH TEMPERATURE PEM FUEL CELL TECHNOLOGY

2.1. Fundamentals and Operation of HT-PEMFC

HT-PEM Fuel Cells consist of a polymer membrane, electrodes, gas diffusion layers and bipolar plates. Figure 2.1 shows a typical representation of the PEM fuel cell with its components. Gas diffusion layers, catalyst layers and membrane constitute membrane electrode assembly (MEA).
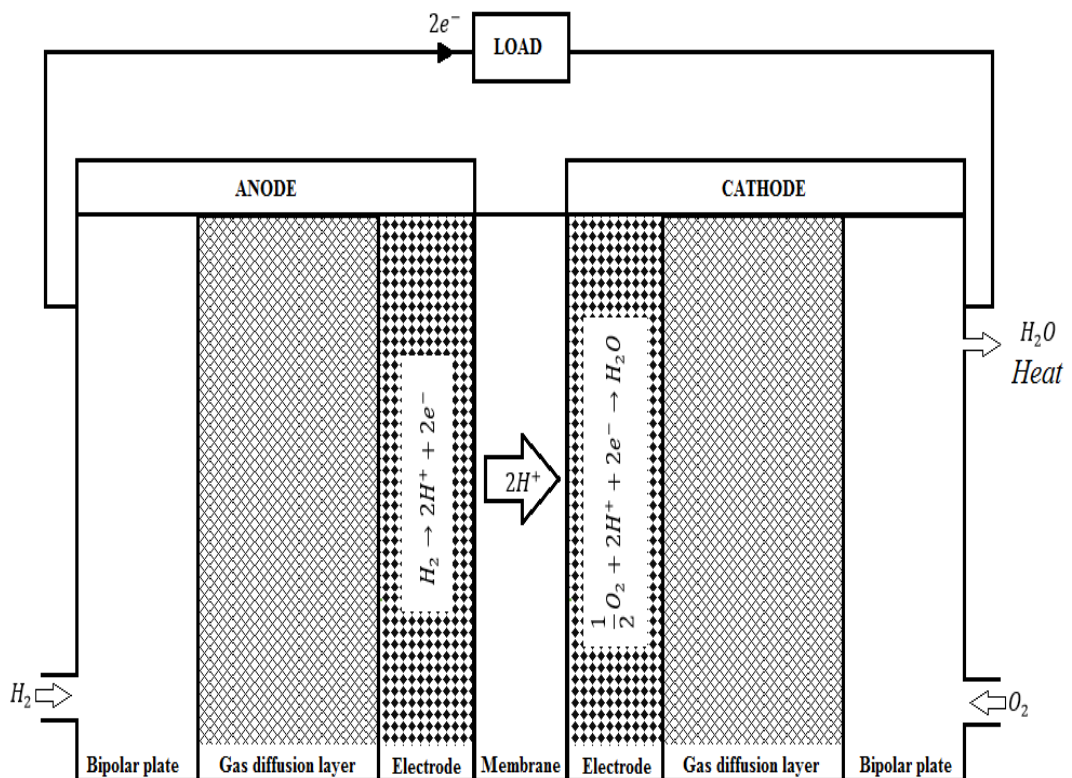
Figure 2.1 Representation of the PEM fuel cell

Reactants fed from anode and cathode inlets diffuse through the gas diffusion layer and reach electrodes at which oxidation and reduction reactions take place. Hydrogen splits into its protons and electrons at the anode catalyst layer as it is written in the Equation 2.1. The protons pass through the membrane; whereas, the electrons completes the circuit by flowing through an external path. At the cathode catalyst layer, oxygen reacts with protons and electrons coming from the anode compartment and form water and heat as it is written in the Equation 2.2.

Anode half-reaction: $H_2 \rightarrow 2H^+ + 2e^-$ $E^0 = 0\,V$ (2.1)

Cathode half-reaction: $\frac{1}{2}O_2 + 2H^+ + 2e^- \rightarrow H_2O$ $E^0 = 1.2291\,V$ (2.2)
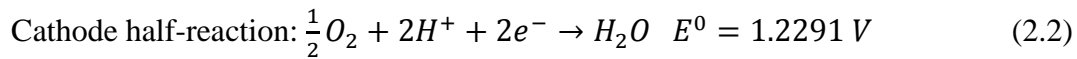
The theoretical cell potential of the fuel cell is 1.229 V when the potential of anode and cathode half-reactions are taken into account. However, three types of voltage loss cause the potential of the cell to drop. These are mainly activation losses, ohmic losses and concentration losses as shown in the Figure 2.2. Activation losses are caused by the energy requirement for the bonding and breaking of chemical bonds in the anode and cathode compartments. Ohmic losses result from the resistance to proton transfer through electrolyte and the resistance to electron transfer through the collector plates. Concentration losses arises from drop of the reactant gases especially at high current densities due to their considerable consumption [3].
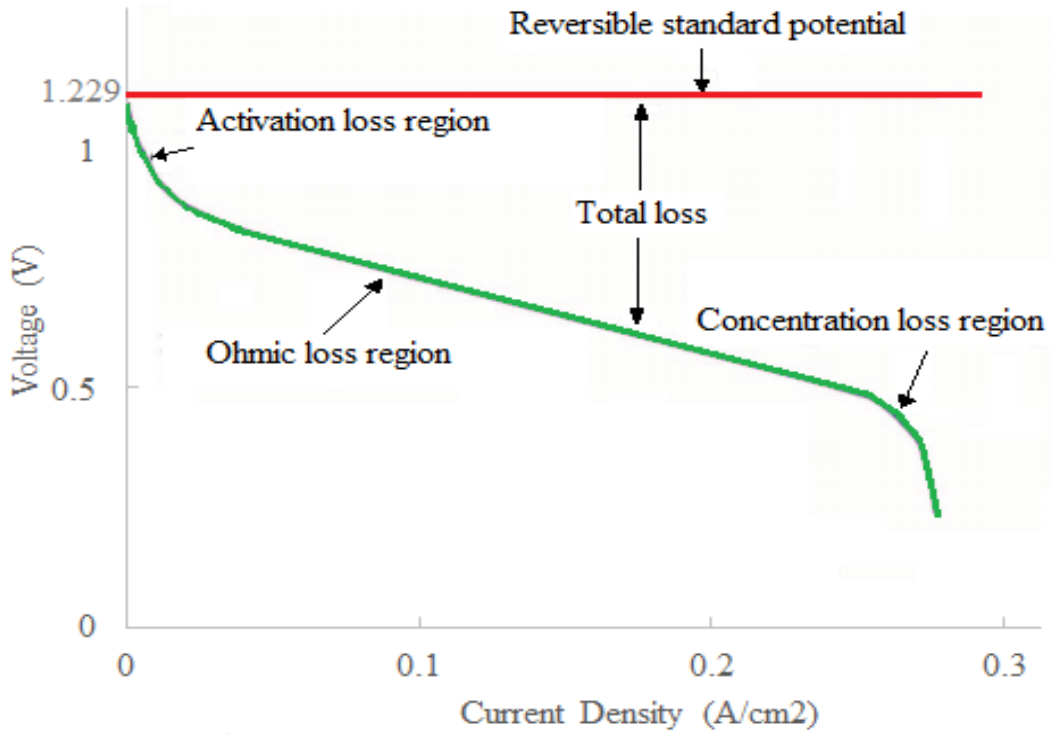
Figure 2.2 Polarization curve of a HT-PEMFC with various losses

Figure 2.3 shows the individual losses and their change with respect to the current density. The behavior of these losses can be explained by Equation 2.3 which illustrates the different loss terms and their relation with cell voltage.

$$E = U_o - \frac{RT}{\alpha F} ln\left(\frac{i}{i_0}\right) - R_{ohm}i - \frac{RT}{nF} ln\left(\frac{i_L}{i_L - i}\right) \tag{2.3}$$

where E is the cell voltage (V), R is the universal gas constant (J mol^{-1} K^{-1}), T is temperature (K), i is current density (A m^{-2}), i$_0$ is the exchange current density (A m^{-2}), F is Faraday's constant (C), R$_{ohm}$ is the ohmic resistance, n is the number of transferred electrons with the reaction and i$_L$ is the limiting current density (A m^{-2}). Second term in the right hand side stands for the activation losses, third term is for the ohmic losses and the last term is for the concentration losses taking place within the system. By taking into account all these losses occurring within the fuel cell, the typical shape of polarization curve is obtained.

9
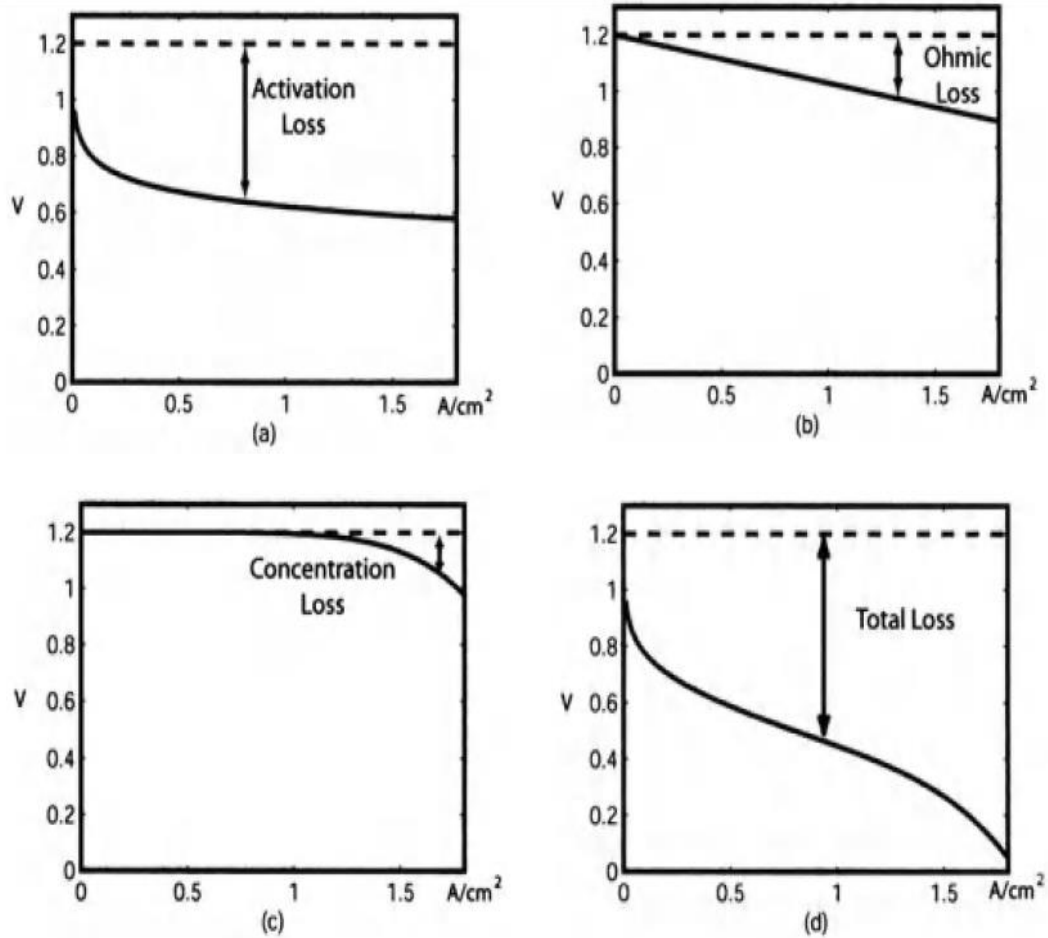
Figure 2.3 Voltage drops caused by different types of losses in fuel cell: (a) activation losses only; (b) ohmic losses only; (c) concentration losses only; (d) total losses[3]

A single cell generally produces about 0.6-0.7 V because of the activation, ohmic and mass transfer losses within the system and to attain the maximum power. In order to have higher power values, single cells are connected in series to form a stack. Depending on the required power, the number of cells within the system can be increased or decreased.

2.2. HT-PEMFC Components

2.2.1. Bipolar plates

Metallic, polymeric and graphite materials are used in the bipolar plates. Graphite is most preferred among the other materials used in bipolar plates due to its resistance to corrosion. Conductivity of some materials used in bipolar plates is as follows: C polymer approximately 100 S m^{-1}, graphite 10^5 S m^{-1}, gold 4.5x10^9 S m^{-1}, Fe alloys 5.3x10^8 S m^{-1}, Ti 2.4x10^7 S m^{-1}. Although metallic materials have higher conductivity, they are not preferred because of their high cost and low resistance to corrosion. The manufacturing process of polymeric materials are rather easy and cheap compared with the metallic and graphite materials; however, the major drawback in the polymeric materials is the low conductivity. Adding graphite to the polymeric material increases the conductivity of the bipolar plate; on the other hand, as the amount of graphite material increases the mechanical properties of the material decrease undesirably, which makes manufacturing more difficult and expensive [4].

Various types of flow channel configurations are investigated for the fuel cells to distribute the reactant gases uniformly. Some of the most commonly used flow channel configurations are shown in Figure 2.4. Although straight flow channel geometries assures uniform distribution, it is valid only in ideal cases. Especially straight flow with small manifolds fails to distribute reactants uniformly, since most of the gases flow through the channels adjacent to the manifolds. In the criss-cross geometry, the drawbacks of straight channels are aimed to be overcome by the addition of flow channels perpendicular to the straight ones. However, a significant improvement in the performance is not observed. In small active areas, serpentine flow channel is usually used, because it flows through the entire area. It is not preferred in larger active areas because of high pressure drop. Therefore, multichannel serpentine flow channels are used in the fuel cells having large active area, since it has the same advantages with single serpentine. Mixed serpentine flow channels resembles the multichannel serpentine flow channels; on the other hand, it provides mixing in every turn decreasing the effect of channel blocking [2].

11
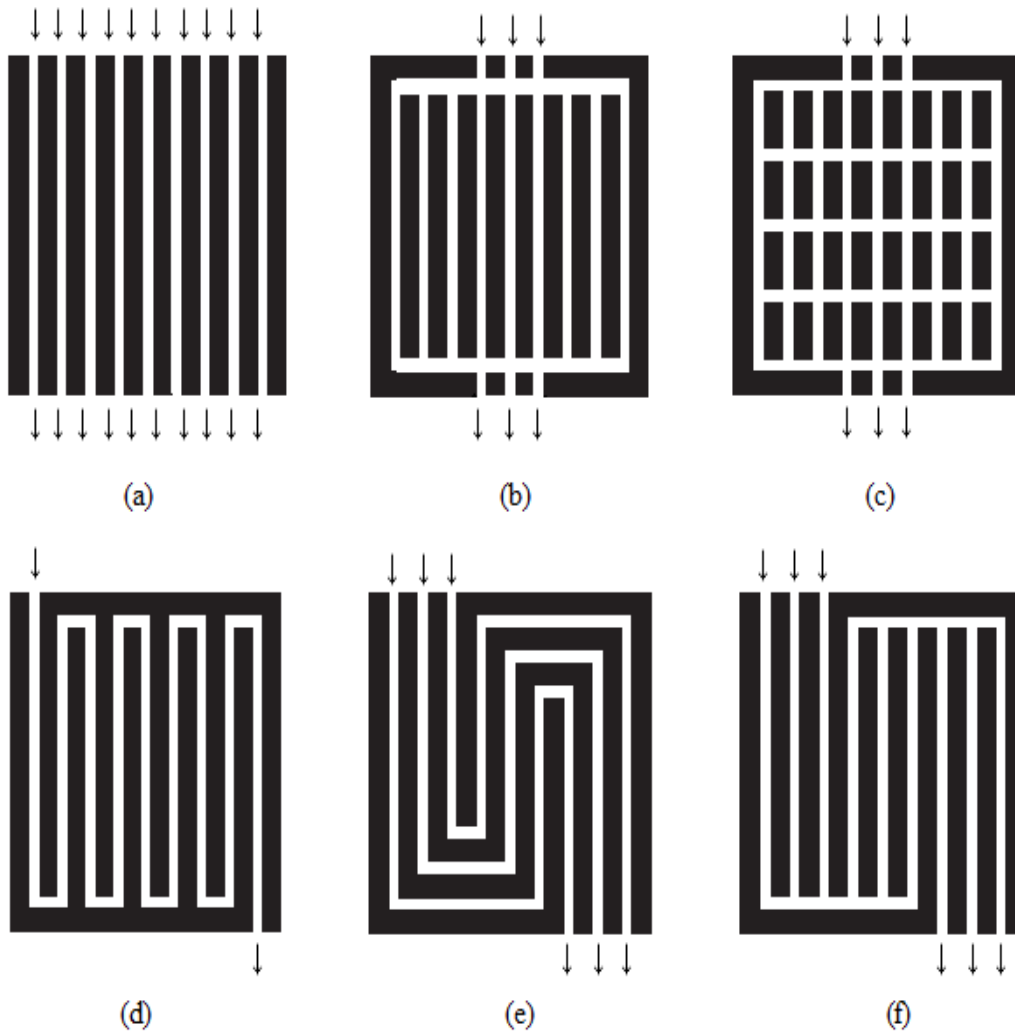
Figure 2.4 Flow Field Configurations used in Fuel Cells (a, b) Straight, (c) criss-cross, (d) single channel serpentine, (e) multichannel serpentine, (f) mixed serpentine [2]

2.2.2. Gas Diffusion Layers

Gas diffusion layer (GDL) has a porous structure that enhances the diffusion of the reactant gases from the flow channels to the active sites of the catalyst. GDL is a thick layer which increases protection and mechanical strength for the catalyst layer. It is generally made of carbon paper or carbon cloth to ensure the structural strength for the electrons [5]. Moreover, GDL is an electron conductor transferring electrons from catalyst layers to the bipolar plates.

2.2.3. Catalyst Layers

Electrode is a layer placed between the gas diffusion layer and the electrolyte in which the electrochemical reactions take place. Platinum is the catalyst that is used most frequently used in the PEMFC. In order to have higher power densities with lower ohmic losses, a thin catalyst layer is required with higher platinum loading per unit area.

There exist two different procedures followed in the preparation of the catalyst layers. The slurry including electrocatalyst is deposited on the gas diffusion layer. The membrane is pressed with the coated gas diffusion layers in order to attain desired contact. However, in this approach the ionic contact resistance between the electrolyte and the catalyst layers is higher than desired. As a second approach, the slurry containing electrocatalyst is deposited on the membrane. In this case, the interfacial resistance is decreased in addition to the enhanced Pt utilization [6].

2.2.4. Electrolyte

Phosphoric acid doped polybenzimidazole (poly[2,2-(m-phenylene)-5,5-bibenzimidazole]; PBI) is considered to be the most promising among the alternative membranes by virtue of its high proton conductivity, high thermal stability and high fuel cell performance [7]. Synthesis and the molecular structure of PBI membrane is given in Figure 2.5.

Figure 2.5 Synthesis of PBI membrane [7]

Thermal stability of PBI membranes has been examined. Weight loss is approximately 13% at the temperatures up to 150 °C for pure PBI due to the loss of absorbed water. On the other hand, no further significant weight loss is observed for the temperatures between 150-500 °C, meaning that it is thermally stable at that range. Substantially higher weight loss occurs above 500 °C because of the polymer oxidation [8]. In order to increase the proton conductivity of PBI membrane, the membrane is doped with several inorganic acids such as sulfuric acid, phosphoric acid, perchloric acid, nitric acid and hydrobromic acid [9–13]. Phosphoric acid is the most promising one among these acids because it provides good proton conductivity, high thermal stability as well as its low vapor pressure.

The proton conductivity of PBI membrane depends on several factors such as acid doping level and relative humidity of the membrane. Acid doping level of the membrane is calculated by doped moles of phosphoric acid per repeated unit of PBI by taking the weight difference of doped and undoped membranes [14]. At constant temperature and relative humidity, the proton conductivity of PBI membrane increases with increasing acid doping level [9,14,15]. Relative humidity also affects

the proton conductivity of PBI membrane; however, this dependence is more pronounced at higher temperatures. For instance, when the relative humidity is increased from 5.6 to 20% the proton conductivity of PBI membrane increases from 3 to 4 S m^{-1} at 140 ∘C, whereas the proton conductivity increases from 4 to 7 S m^{-1} when the relative humidity increases from 1 to 5% [14]. Proton conductivity as a function of acid doping level and temperature is studied by Hjuler et. al [16] at 100 ∘C and 180 ∘C. It is seen that conductivity is proportional to temperature; on the other hand, the same behavior is not observed for acid doping level. Moreover, the fuel cell performance of pure hydrogen and reformate gas is investigated. It is concluded that use of reformate gas instead of pure hydrogen yields in approximately 5% loss in the power density.

The protons, positively charged hydrogen ions, evolved in anode half-reaction passes through the membrane by following proton hoping mechanism as shown in Figure 2.6. The proton diffuse through the molecules by hydrogen bonding. It sticks to the phosphoric acid and causes another hydrogen ion to leave.
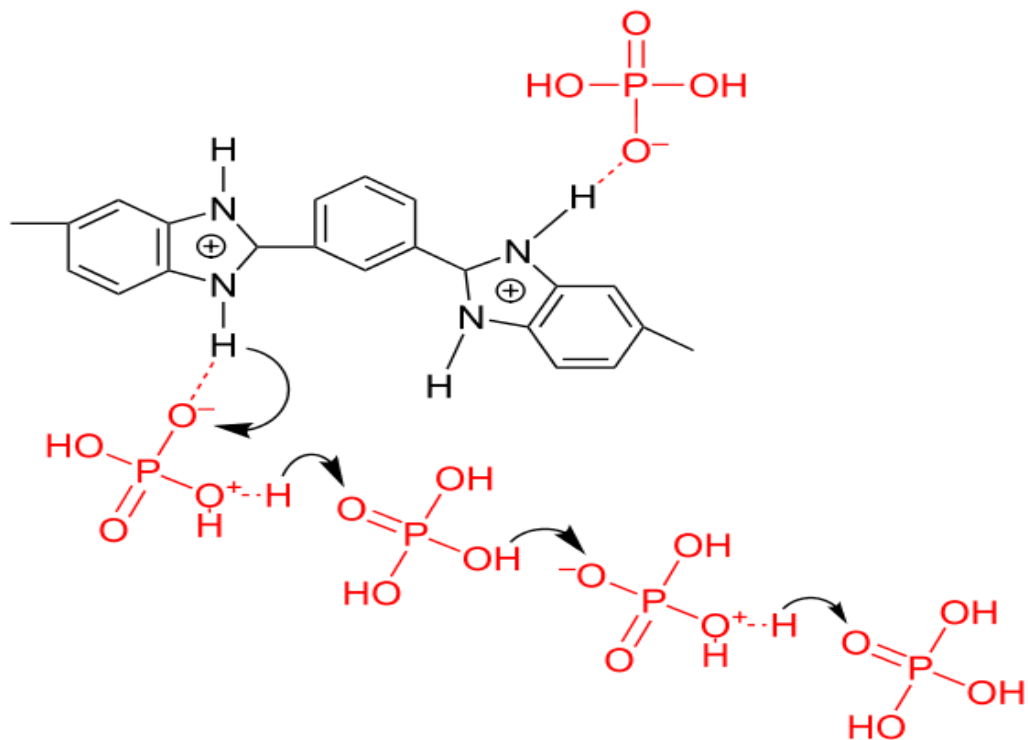
Figure 2.6 Interaction between phosphoric acid and PBI membrane for proton transfer [17]

15

2.3. HT-PEMFC Experimental Results Available in Literature

There are several works published in literature with different operating conditions. Table 2.1 lists some of the works conducted with an active area less than 50 cm^2. Researchers have investigated the influence of operation temperature, stoichiometric excess of anode and cathode feeds and pressure. It is seen that changing anode stoichiometric excess does not have a significant effect on the fuel cell performance. Therefore, the studies have mainly focused on the stoichiometric excess of cathode feed taking into account the partial pressure of oxygen in the air. Increase in operation temperature, stoichiometric excess and pressure enhances the performance of the fuel cell. Table 2.2 lists the experimental conditions performed for commercial size HT-PEMFCs, which have an active area larger than 100 cm^2. In some of the commercial size applications, reformate gas was used as anode fuel in order to observe influence of carbon monoxide and carbon dioxide on the performance of the HT-PEMFC.

Table 2.1 List of experimental conditions on HT-PEMFC published in literature

Author	Year	Active Area (cm^2)	Fuel Type	Operation Temperature	Stoichiometric Excess (A/C)	Pressure
Korsgaard et al. [18]	2006	45.16	H$_2$/Air Reformate/Air	120-180 ^{o}C	(2.5/2, 2.5/3, 2.5/5)	Ambient
Hu et al. [19]	2006	7.8	H$_2$/O$_2$	150 ^{o}C	NA	0.2 MPa backpressure
Zhang et al. [20]	2007	2.6	H$_2$/Air	120-200 ^{o}C	(1.5/2) (1.5/4) (1.5/6) (1.5/10)	Ambient
Scott et al. [21]	2007	9	H$_2$/O & H$_2$/Air	125-175 ^{o}C	1.5/2.2	1-2 bar
Ubong et al. [22]	2009	45	H$_2$/Air	120-180 ^{o}C	(1.2/2) (1.2/2.5) (1.2/3)	Ambient, 25 psig backpressure
Wannek et al. [23,24]	2009	14.4	H$_2$/Air	160 ^{o}C	(2/2) (3/3) (6/6)	Ambient
Parrondo et al [25]	2010	3.24	H$_2$/O$_2$	160-200 ^{o}C	1.2/2	Ambient
Su et al. [26]	2012	5	H$_2$/O$_2$	160-200 ^{o}C	NA	Ambient
Steenberg et al [27]	2012	10	H$_2$/Air	NA	4/4	NA
Bezmalinovic et al[28]	2014	50	H$_2$/Air	160 ^{o}C	(1.3/1.5)(1.3/2)(1.3/3)	1 atm backpressure
Sun et al. [29]	2015	16 cm^2	H$_2$/Air	170 ^{o}C	2/3.5	1 atm backpressure
Devrim et al. [30]	2016	5 cm^2	H$_2$/Air	140-180 ^{o}C	1.5/2.5	NA

Table 2.2 List of experimental conditions on HT-PEMFC published in literature with commercial size MEA

Author	Year	Active Area	Fuel Type	Operation Temperature	Stoichiometric Ratio (A/C)	Pressure
Li et al.[*](review) [31]		256 cm^2	H$_2$/Air	170 ^{o}C	NA	Ambient
Juelich/FuMa-Tech			H$_2$/Air	180 ^{o}C		Ambient
BASF-PEMEAS Sartorius	2009		H$_2$/Air	160 ^{o}C		Ambient
Plug Power Volkwagen Sartorius			H$_2$/Air	160 ^{o}C		3 bar
Lüke et al. [32]	2012	200 cm^2	H$_2$/Air Reformate/Air	160 ^{o}C	2/2	NA
Hjuler et. al [8]	2012	140 cm^2	H$_2$/Air Reformate/Air	160 ^{o}C	1.3/3	Ambient
Janßen et al. [33]	2013	320 cm^2	H$_2$/Air Reformate/Air	160-180 ^{o}C	1.6/2 2.7/2	NA
Samsun et al. [34]	2014	340 cm^2	Reformate/Air	160 ^{o}C	1.2/2	NA

18

2.4. HT-PEMFC Modeling Available in Literature

Cheddie and Munroe [35] developed the first mathematical model for the HT-PEMFC. In their one-dimensional (1D) model, they studied the effect of the cathode feed flow rate as well as the conductivity of the electrolyte. They compared the performance curves of air and oxygen both by model and experiments. The results show that using pure oxygen as cathode feed yields in better fuel cell performance. In addition, they obtained the polarization curve for different electrolyte conductivities ranging from 1.87 S m^{-1} to 17 S m^{-1}. It is seen that the best performance is obtained with high conductivity and oxygen as cathode feed, since higher electrolyte conductivity results in lower ohmic losses.

In their paper, Cheddie and Munroe [36] investigated the effect of GDL porosity, catalyst activation, Pt weight fraction and membrane conductivity on the fuel cell performance. The porosity of the GDL do not have a significant impact on the activation loss and ohmic loss regions; however, the concentration loss region, at which gas transport limitations are observed, is highly affected by the GDL porosity. High porosity yields in higher permeability of gases which enhances the performance. On the other hand, as the porosity increases the amount of solid region decreases, which causes decrease in the effective thermal and ionic conductivity affecting performance negatively. Therefore, it is concluded that there occurs an optimum porosity for the GDL.

In their three-dimensional (3D) model, Peng and Lee [37] studied the effect of temperature on the fuel cell performance in the range of 125-160 ^{o}C and found out that increasing temperature provides better fuel cell performance. They constructed both isothermal and non-isothermal models in order to investigate the effect of isothermal assumption on the modeling. At 0.6 V, the maximum difference in current density between isothermal and non-isothermal models is 35 A m^{-2} under collector land areas. Moreover, they obtained the temperature distribution in the midway section of the fuel cell having approximately 2 ^{o}C difference at high current densities whereas this value drops down to 0.1 ^{o}C at low current densities.

In their paper, Scott et. al [21] developed a 1D isothermal model. Effect of operation pressure and temperature on the fuel cell performance is analyzed. The model results show that increasing pressure and temperature enhances the fuel cell performance. At 175 °C peak power densities of 1 bar and 2 bar operations are 4850 W m^{-2} and 6300 W m^{-2}, respectively. The fuel cell performance is amended by the increasing temperature. In addition to temperature and pressure, influence of the platinum loading on the cathode catalyst layer is studied. The predicted power densities increase with increasing Pt loading; on the other hand, higher power density per unit mass of platinum is obtained at low Pt loading.

The influences of operation temperature and air stoichiometry on the performance are examined by Ubong et. al [22] using a 3D isothermal model. Higher temperatures are favorable for better fuel cell performance. On the other hand, it is seen that increasing stoichiometric excess of the air does not have a significant effect on the power density. Enhancement in the power density is insignificant with increasing stoichiometric excess of air as long as enough air is fed to the system.

Lobato et. al [38] constructed a 3D isothermal model to investigate the effect of flow channel geometry on the fuel cell performance. Three different flow channel geometries are used in the model: 4-step serpentine, parallel and pin-type. By assuming hydrogen concentration do not have an effect on the cathode performance because of its sufficient amount, they modeled only the cathode compartment. The best performance among the three flow channel geometries is obtained with serpentine flow channels. However, the performance of pin-type and serpentine flow channel are approximately the same at low current densities. In addition, the effect of cathode inlet flow rate is studied for five different flow rates. At low current densities, the flow rate does not have a significant effect on the performance because of the low demand for oxygen. It is seen that higher amount of feed gives better performance especially at high current densities at which diffusion effect is observed. Influence of the operation temperature on the fuel cell performance is also modeled. According to the model, higher operation temperature gives better fuel cell performance because of the increase in the electrolyte conductivity.

Kvesić et. al [39] developed a 3D non-isothermal computational fluid dynamics (CFD) model for a five cell short stack with an active area of 200 cm^2. The model validation is performed by measuring local temperature and local current density with a plate located between 3rd and 4th cell in the stack. The model results and measured local temperature values do not have a significant variation, the maximum temperature difference is approximately 1%.

Su et. al [26] built a two-dimensional (2D) non-isothermal model in order to investigate the effect of operation temperature and PBI loading on the fuel cell performance. Enhanced reaction kinetics and mass transport processes increases the performance as the operation temperature increases. On the other hand, there occurs degradation as PBI loading increases from 5 wt % to 30 wt %. Increase in PBI loading results in blocked oxygen transport as well as decrease in the Pt volume fraction.

Proposing a 3D non-isothermal model, Krastev et. al [40] studied the influence of pure hydrogen and syngas on the fuel cell performance. Due to the reduction in hydrogen concentration and presence of carbon monoxide in the anode feed, the fuel cell performance diminished. Moreover, the performance curve for PBI and pyridine membranes is obtained by using pure hydrogen and syngas. It is seen that PBI membrane both with pure hydrogen and syngas provides better results when the power densities are compared with the pyridine membranes.

In their study, Sun et. al [41] studied the effect of GDL porosity, GDL thickness and cell temperature on the fuel cell performance by using a 2D model. It is deduced that increasing the GDL porosity from 0.2 to 0.5 enhances the fuel cell performance because of the proportionality between effective diffusivity and GDL porosity. This results in enhancement of oxygen molecule transport to the cathode catalyst layer making the reaction rate to be faster. The fuel cell performance decreases by using thicker GDL. Thicker GDL raises the concentration over-potential.

Table 2.3 illustrates some of the mathematical models in regard to chronological order. As it is seen from the table, model dimension varies with respect to the publication year. Most of the models have been developed for steady-state case in order to examine the effect of model parameters on the fuel cell performance. On

the other hand, there exist dynamic models to observe the behavior of the system at the start-up. Figure 2.7 shows a representation of model domain used in 1D and 2D models of HT-PEMFC. Only z-direction is taken into account for the 1D models; on the other hand, xz-plane or yz-plane can be used in the 2D models. Both 1D and 2D models fail to predict the behavior of the system in the remaining dimensions. For the solution technique of 2D and 3D models, Comsol Multiphysics and ANSYS-Fluent are used. There exist both 2D and 3D models in recent years. 2D models fail to predict all the phenomena occurring within the system since they do not take into account the third dimension. 3D models require more time when they are compared with the 2D models; however, an appropriate and validated model could elucidate the system behavior in all aspects. 3D models given in Table 2.3 are either modeled with a single channel domain or only the cathode compartment is taken into account by neglecting anode overpotential. This current study includes 3D model of a single cell with the consideration of entire active area and flow channels.
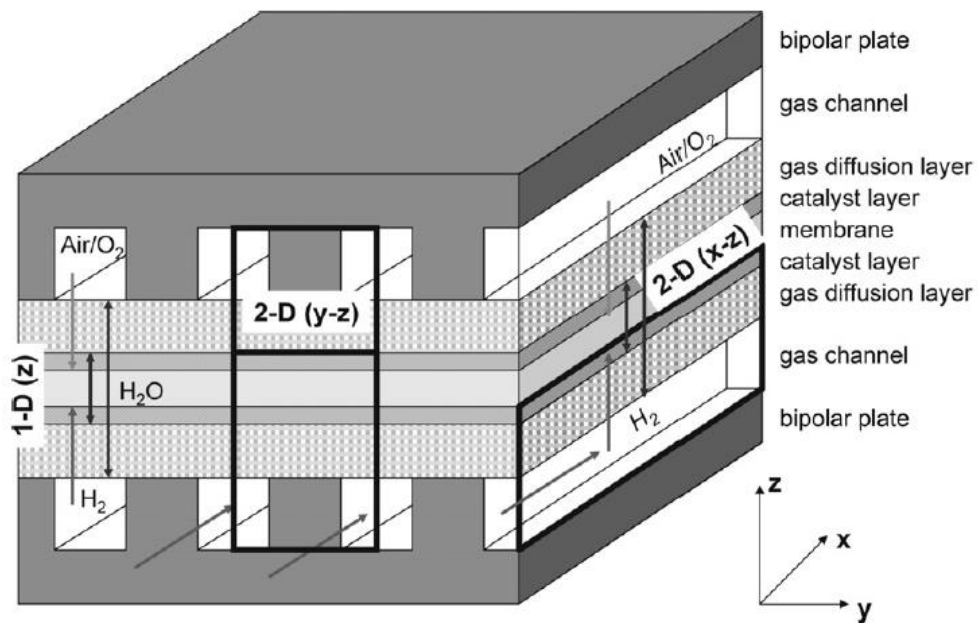
Figure 2.7 Model domains used in 1D and 2D models of HT-PEMFC [2]

Table 2.3 Solution technique of mathematical models for HT- PEMFC in literature

Authors	Year	Model Dimension	Model Domain	Solution Technique	I/NI
Cheddie & Munroe [35,36]	2006	1D	Single cell	Runge-Kutta Method	NI
Cheddie & Munroe [42]	2006	3D	Single channel	FEMLAB 3.1i	NI
Hu et al. [19]	2006	2D	Half cell yz-plane	FEMLAB	I
Peng & Lee [37]	2006	3D	Single channel	FLUENT 6.1	NI
Cheddie & Munroe [43]	2007	2D	Single cell xz-plane	FEMLAB 3.1i	NI
Scott et al. [21]	2007	1D	Single cell	Comsol Multiphysics	I
Ubong et al. [22]	2009	3D	Single channel	Comsol Multiphysics	I
Lobato et al. [38]	2010	3D	Single half-cell	Comsol Multiphysics	I
Siegel et al. [44]	2011	3D	Single cell	Comsol Multiphysics	NI
Reddy & Jayanti [45]	2012	3D	Single channel	ANSYS-Fluent	NI
Kvesić et al. [39,46]	2012	3D	Single cell+cooling	ANSYS-Fluent	NI
Su et al. [26]	2012	2D	Single cell yz-plane	Comsol Multiphysics	NI
Chippar & Ju [47]	2013	3D	Single channel	FLUENT	NI
Bezmalinović et al. [28]	2014	2D	Single cell xz-plane	Comsol Multiphysics	I
Lang et al. [48,49]	2015	2D	Single cell xz-plane	Finite Element Method	NI
Elden et al. [50]	2016	2D	Single cell yz-plane	Comsol Multiphysics	NI
Caglayan et. al [51,52]	2016	3D	Single cell	Comsol Multiphysics	I

CHAPTER 3

3. MODEL DEVELOPMENT

3.1. Three-Dimensional Isothermal Model

Three-dimensional single cell models with triple mixed serpentine type of flow channel are built for numerical modeling. The single cell having an active area of 25 cm^2 includes phosphoric acid doped PBI membrane. Model of the cell is solved by a commercial software package, Comsol Multiphysics 5.0 Batteries and Fuel Cell Module. The numerical solution is obtained by using finite element method. The representation of the model domain can be found in Figure 3.1. Dimensions of each component in the modeling domain are tabulated in Table 3.1. Air and hydrogen are used feed with the stoichiometric coefficients of 2.5 and 1.5, respectively. Graphite material is used in the bipolar plates. Cell voltage is taken as 0.6 V; on the other hand, parametric sweep is used in order to obtain the polarization plot. General parameters used in the modeling are given in Table 3.2.

Table 3.1 Dimensions of HT-PEM fuel cell components used in the model

Description	Value	Units
Active Area	25	cm^2
Channel Height	7.5 x 10^{-4}	m
Channel Width	7.5 x 10^{-4}	m
Rib Width	1.5 x 10^{-3}	m
GDL Width	5.5 x 10^{-4}	m
Electrode Thickness	2.5 x 10^{-5}	m
Membrane Thickness	7.5 x 10^{-5}	m
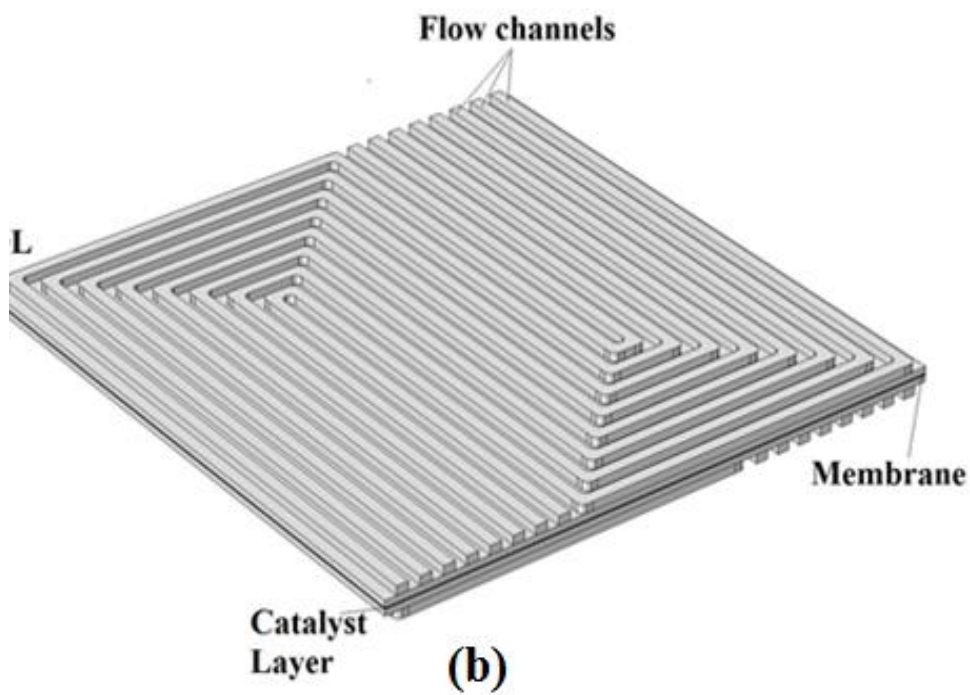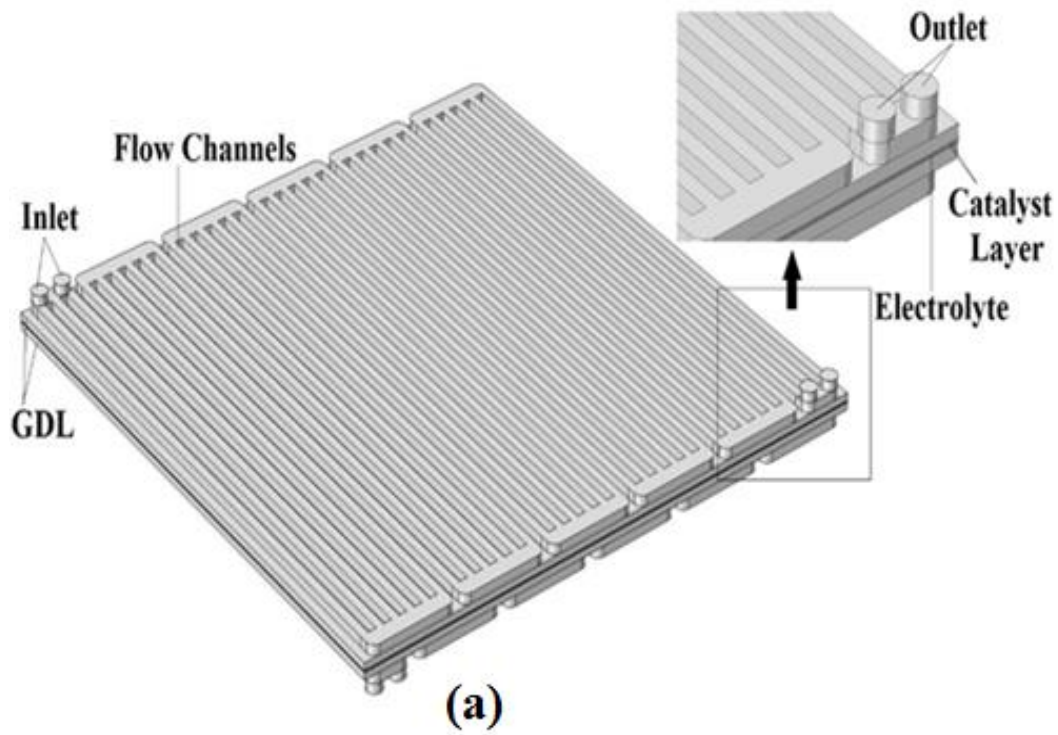
Figure 3.1 Isothermal model domains (a) triple mixed serpentine (b) serpentine

Table 3.2 Parameters used in Comsol Multiphysics at 165 °C

Parameter	Value	Unit
GDL Porosity	0.5	-
GDL Permeability	3×10^{-12}	m^2
GDL Electric Conductivity	687.5	S/m
Anode Viscosity [53]	1.144×10^{-5}	Pa s
Cathode Viscosity [53]	2.465×10^{-5}	Pa s
H_2-H_2O Binary Diffusion Coefficient [54]	41.9×10^{-6}	$m^2\ s^{-1}$
N_2- H_2O Binary Diffusion Coefficient [54]	144×10^{-6}	$m^2\ s^{-1}$
O_2-N_2 Binary Diffusion Coefficient [54]	34.2×10^{-6}	$m^2\ s^{-1}$
O_2-H_2O Binary Diffusion Coefficient [54]	49.2×10^{-6}	$m^2\ s^{-1}$
Oxygen Reference Concentration [22]	40.88	mol m^{-3}
Hydrogen Reference Concentration [22]	40.88	mol m^{-3}

3.1.1. Assumptions

- Steady state
- Laminar flow
- All reactants and products are in gaseous phase
- All gases and water obey the ideal gas law
- Operation is performed under isothermal conditions
- No crossover of gases and water through the membrane
- The physical properties of the components are constant
- GDL is composed of isotropic and homogeneous porous materials.

3.1.2. Governing Equations

Conservation equations are employed in order to develop a mathematical model for the system. These are basically the conservation of mass, conservation of momentum, conservation of charge and conservation of energy for the non-isothermal models. In order to simplify the equations related to each specified system, assumptions are taken into account. The model domain is analyzed in four parts: flow channels, gas diffusion layers, catalyst layers and the membrane.

3.1.2.1. Flow Channels

For the incompressible mass transport in the flow channels Navier-Stokes equation can be applied as in the Equation 3.1, with simplified form of the continuity equation written in Equation 3.2.

$$\rho(u.\nabla)u + \nabla p - \nabla.\mu(\nabla u + (\nabla u)^T) = 0 \tag{3.1}$$

$$\nabla.(\rho u) = 0 \tag{3.2}$$

Where u is the velocity vector (m s^{-1}), ρ is the gas mixture density (kg m^{-3}), p is the pressure term (N m^{-2}) and μ denotes the dynamic viscosity of the mixture (kg m^{-1} s^{-1}).

Mass transport of each species within the system can be explained by the general form of Maxwell-Stefan equation.

$$\nabla.\left[-\rho w_i \sum_j \left(D_{ij}\nabla x_j + (x_j - w_j)\frac{\nabla p}{p}\right) + \rho w_i u\right] = 0 \tag{3.3}$$

Where w_i is the mass fraction of the species i in the mixture, and D_{ij} denotes the binary diffusion coefficient (m^2 s^{-1}).

3.1.2.2. GDL

The transport phenomena occurring in the GDL, which is a porous system, can be elucidated by the Darcy's law. The generation term must be added to the Navier-Stokes equation.

$$\rho(u.\nabla)u + \nabla p - \nabla.\mu(\nabla u + (\nabla u)^T) = -\frac{\mu}{k_p}u \tag{3.4}$$

Where k_p denotes the permeability of gas diffusion layer (m^2). Finally, a charge balance must be performed in the GDL as shown in Equation 3.5;

$$\nabla.\left(\kappa_s^{eff}\nabla\emptyset_s\right) = 0 \tag{3.5}$$

Where κ_s^{eff} denotes the effective ionic conductivity of the solid phase (S m^{-1}) and $\emptyset_s$ is the phase potential.

3.1.2.3. Catalyst Layer

The simplified form of the Butler-Volmer equation can be used in order to calculate the local current density. The individual equations for anode and cathode compartments are given in Equation 3.6 and Equation 3.7, respectively.

$$i_a = i_a^{ex} \left(\frac{C_{H_2}}{C_{H_2}^{ref}} \right)^{0.5} \left[\frac{\alpha_a + \alpha_c}{RT} F \eta_a \right] \tag{3.6}$$

$$i_c = i_c^{ex} \left(\frac{C_{O_2}}{C_{O_2}^{ref}} \right) \left[exp \left(-\frac{\alpha_c F \eta_c}{RT} \right) \right] \tag{3.7}$$

Where i_a and i_c are the transfer current densities (A m^{-2}) corresponding to the electrochemical reaction at the anode and cathode catalyst layers, respectively; C_{H_2} and C_{O_2} are the concentration (mol m^{-3}) for hydrogen and oxygen; η_a and η_c are the potential difference between solid matrix and the electrolyte; α_a and α_c are the transfer coefficients for anode and cathode.

3.1.2.4. Electrolyte

For the electrolyte, because of crossover of gases through the membrane is neglected; therefore, only charge balance   is considered.

$$\nabla. (\kappa_e \nabla \emptyset_e) = 0 \tag{3.8}$$

κ_e denotes the   proton conductivity (S m^{-1}) of the phosphoric acid doped PBI membrane and $\emptyset_e$ is the phase potential at the electrolyte.

3.1.3. Boundary Conditions

- Continuity at all boundaries
- No slip for all channel walls
- Suppress backpressure
- Constrain outer edges set to zero for both inlet and outlet
- Bipolar plates on the both side of the cell set to electric ground and cell operation potential

3.2. Three-Dimensional Non-Isothermal Model

The non-isothermal model is developed for the HT-PEMFC with triple mixed serpentine flow channel geometry. In addition to the equations used in isothermal model, conservation of energy is applied for the system. The thermal properties used in the non-isothermal model is given in Table 3.3.

Table 3.3 Thermal properties of components used in non-isothermal model

Description	Value	Unit
Thermal conductivity of GDL [50]	1.15	W m^{-1} K^{-1}
Thermal conductivity of membrane [47]	0.95	W m^{-1} K^{-1}
Thermal conductivity of hydrogen [55]	0.204	W m^{-1} K^{-1}
Thermal conductivity of air [55]	0.03	W m^{-1} K^{-1}
Specific heat capacity of hydrogen [55]	14400	J kg^{-1} K^{-1}
Specific heat capacity of air [55]	1010	J kg^{-1} K^{-1}
Specific heat capacity of GDL [55]	1050	J kg^{-1} K^{-1}
Specific heat capacity of membrane [47]	1650	J kg^{-1} K^{-1}

3.2.1. Assumptions

- Steady state
- Laminar flow
- All reactants and products are in gaseous phase
- All gases and water obey the ideal gas law
- No crossover of gases and water through the membrane
- The physical properties of the components are constant
- GDL is composed of isotropic and homogeneous porous materials.

3.2.2. Governing Equations

Conservation of energy is employed in the non-isothermal model as well as the conservation of mass, momentum and charge equations used in the isothermal model.

$$\nabla.\left(\rho C_p u T\right) = \nabla(k^{eff}\nabla\text{T}) + S_T \qquad (3.9)$$

30

$$\rho C_p = \varepsilon(\rho C_p)_f + (1 - \varepsilon).(\rho C_p)_s \qquad (3.10)$$

Where T is temperature (K), C_p is the specific heat (J kg^{-1} K^{-1}), k^{eff} is the effective thermal conductivity (W m^{-1} K^{-1}) and S$_T$ is the source term in the energy balance varying for each component in the model domain. Subscript f is used for the fluid phase, whereas s is used for the solid matrix. There is no source term in the flow channels and GDL. The source term for the catalyst layers is given below;

$$S_T = i_c \left(\eta + T\frac{dU_o}{dT} \right) + \frac{I^2}{\kappa^{eff}} \qquad (3.11)$$

Where η is the overpotential (V), U$_o$ is the thermodynamic equilibrium potential (V) which depends on temperature as given below [56];

For anode; $U_o = 0$ \qquad (3.12)

For cathode; $U_o = 1.23 - 9.10^{-4}(T - 298.15)$ \qquad (3.13)

Generation term for the membrane is given below;

$$S_T = \frac{I^2}{\kappa^{eff}} \qquad (3.14)$$

$$\eta = \emptyset_s - \emptyset_e - U_o \qquad (3.13)$$

3.2.3. Boundary Conditions

- Continuity at all boundaries
- No slip for all channel walls
- Suppress backpressure
- Constrain outer edges set to zero for both inlet and outlet
- Thermal insulation for all walls
- Bipolar plates on the both side of the cell set to electric ground and cell operation potential

3.3. Comsol Multiphysics

For the modeling and simulations of the physics-based problems, Comsol Multiphysics is used as a commercial software based on numerical methods in the solution of partial differential equations. By coupling the appropriate physics related to the problem, the transport phenomena occurring within the system can be solved. When a system is aimed to be modeled, first geometry tool should be used in order to draw the system geometry and built the modeling domain. System parameters can be introduced as a list with denoted symbols or they can be directly written to the related parts. Each physics contain specific equations; for instance, "secondary current distribution" includes conservation of charge, "reacting flow in porous media" includes conservation of species and "heat transfer in porous media" is used to take into account the conservation of energy within the system. By using proper assumptions and boundary conditions related conservation equation can be simplified.

CHAPTER 4

4. THREE-DIMENSIONAL MODELING OF A HIGH TEMPERATURE POLYMER ELECTROLYTE MEMBRANE FUEL CELL AT DIFFERENT OPERATION TEMPERATURES[1]

4.1. Introduction

Fuel cells are electrochemical reactors that directly convert chemical energy to the electrical energy. The direct conversion of chemical energy to the electrical energy yields higher efficiency compared to the internal combustion engines. Moreover, fuel cells have high power density, low or zero emissions, long cell and stack life and low corrosion. Thus, they can be considered as promising alternative energy source for the future [57]. Polymer electrolyte membrane fuel cell (PEMFC) includes a polymer electrolyte acting as an electron insulator and proton conductor [2]. The electrolyte is usually Nafion® produced by DuPont or another perfluorinated polymer [58]. Nafion® has become an industrial standard for the PEMFCs operating at 50-100 °C, because of its high proton conductivity, chemical stability, mechanical strength and flexibility. On the other hand, these properties are only valid at highly hydrated states and temperatures up to 80 °C [59]. It is seen that lower humidity yields to lower conductivity in the membrane [9]. Thus, water and thermal management play a key role in the fuel cells operating at low temperature. In addition, at low temperatures CO tolerance of the fuel cell is relatively low [36]. Even few amount of CO content in the feed stream decreases the cell performance significantly [60]. Therefore, alternative membranes have been investigated in order

---

[1] Caglayan DG, Sezgin B, Devrim Y, Eroglu I. Int J Hydrogen Energy 2016;41:10060–70.

to overcome these problems related to the PEMFC operating at temperatures lower than 100 ℃ [4,36].

Polybenzimidazole (PBI) membranes have been developed for the fuel cells operating at temperatures above 100 ℃. They have good mechanical strength, high chemical and thermal stability at high temperatures [25,61]; moreover, their ionic conductivity is high when they are doped with a strong acid such as phosphoric [7] or sulfuric acid [15,42,62]. In addition to the high conductivity, high temperature operation also has the advantage of having faster reaction kinetics with a single phase. High temperature PEMFC are more tolerant to CO and recovery of waste heat is much simpler compared to the low temperature operation [6,61,63]. Despite these advantages, material degradation and slow start-up are the major drawbacks of this type of fuel cell [38].

Modeling of fuel cells has gained importance in recent years, because it elucidates the transport phenomena occurring within the system [64]. Moreover, modeling reveals the fundamentals of the processes occurring within the system, which cannot be determined by experiments in the current state [43]. Detailed three-dimensional mathematical models of the fuel cell performance have been reported previously in the literature. Ju et al. [56] investigated the influence of GDL thermal conductivity, relative humidity of inlet streams and operating voltage on the cell performance by developing a three-dimensional non-isothermal model. Sun et al. [41] studied the effect of cell temperature, GDL porosity and GDL thickness on the cell performance in their two-dimensional, single phase model. Kvesic et al. [46] presented a three-dimensional non-isothermal model to analyze the performance of a high temperature PEMFC stack operated on reformate gas as well as the effect of co-flow and counter-flow of anode, cathode and cooling oil. Moreover, Krastev et al. [40] developed a three-dimensional non-isothermal single cell model in order to analyze the effect of anode gas composition on the performance of the high temperature PEMFC. The effect of temperature on the performance of the cell was previously investigated both experimentally and theoretically. Cheddie and Munroe [42] built a three-dimensional model to investigate the effect of oxygen flow rate on the cell performance and temperature variation along the cell. In addition, they compared the performance curves of their current model with a two-dimensional model that

they developed in their previous study [36]. In their three-dimensional half-cell model Lobato et al. [38] studied the influence of the inlet flow rate of oxygen, the temperature and flow channel geometry: 4-step geometry, parallel and pin-type. Ubong et al. [22] conducted both experimental and numerical work to investigate the effect of operation temperature, pressure and air stoichiometry on the performance of the high temperature PEMFC. In their study, a three-dimensional model of a single cell with triple serpentine flow channels was built. However, the models are more limited in terms of entire cell and its components. There are few models that take into account all mass, momentum and ion transport within the entire active area and flow channels. Various models have been reported in the literature; nevertheless, most of them are based on single channel geometry. In the literature, there is the inadequacy of the change of parameters from inlet to the outlet of the compartments.

It is reported that the ionic conductivity of the PBI membrane is highly dependent on the temperature [15]. Moreover, temperature affects the reaction kinetics; in other words, higher temperature leads to faster kinetics. Therefore, it is seen that temperature has a significant effect on the cell performance when reaction kinetics and membrane ionic conductivity are taken into account. In a high temperature PEMFC stack design, cooling is an important problem. The strategy of cooling has to be well established before the manufacturing. The cell temperature may vary from one cell to another in a stack that may cause variation in the performance of the cells. Therefore, it is important to investigate the influence of the temperature on the performance during the design stage. In this study, an isothermal, three-dimensional model of a single cell is built for the selected channel geometry and design parameters. The model is solved by Comsol Multiphysics 5.0 Batteries and Fuel Cell Module for different temperatures in the range of 100-180 °C. In this manuscript our purpose is to investigate the sole effect of the temperature on the performance of a single high temperature PEMFC. The originality of this study comes from its solution method and consideration of the entire active area and all components of a single cell. There are very few experimental data reported in literature on temperature dependency of ionic conductivity of PBI membrane and the performance of high temperature PEMFC reported with the same membrane

35

electrode assembly. In the present work the temperature dependency of ionic conductivity has been simulated from experimental data reported for the PBI membrane produced by Danish Power Systems [65]. The design parameters such as air and fuel flow rates, PEMFC active area, channel geometry, channel dimensions, PBI membrane properties were selected from another study of our research group. Experimental polarization data reported in this issue by Sezgin et al. [51] at 160 $^{\circ}$C for a single cell high temperature PEMFC are used to validate the model for both single channel and triple mixed serpentine flow channels. The models also predict the air flow cathode flux, pressure distribution in the cathode and anode flow channels, reactant and product concentration distributions, and corresponding electric current density produced by the fuel cell.

4.2. Model Development

A three-dimensional single cell model with triple mixed serpentine type of flow channel is built for numerical modeling. The cell model, which contains PBI membrane doped with phosphoric acid as electrolyte, is solved by a commercial software package, Comsol Multiphysics 5.0 Batteries and Fuel Cell Module. The numerical solution performed in the program is obtained using finite element method. The representation of modeling domain can be found in Figure 4.1. The dimensions of each component in the modeling domain are tabulated in Table 4.1Air and pure hydrogen are fed to the cathode and anode inlets of the single cell having an active area of 25 cm^2. The stoichiometric coefficients of air and hydrogen are taken as 2.5 and 1.5, respectively. Operating voltage is taken as 0.6 V; however, parametric sweep is used in order to obtain the polarization plot. The effect of temperature on the fuel cell performance is modeled by using single flow channel model which requires less computational time. Numerical values of general parameters used in the computation are listed in Table 4.2. The parameters are used for both single flow channel model and triple mixed serpentine flow channel model.

(a)

(b)
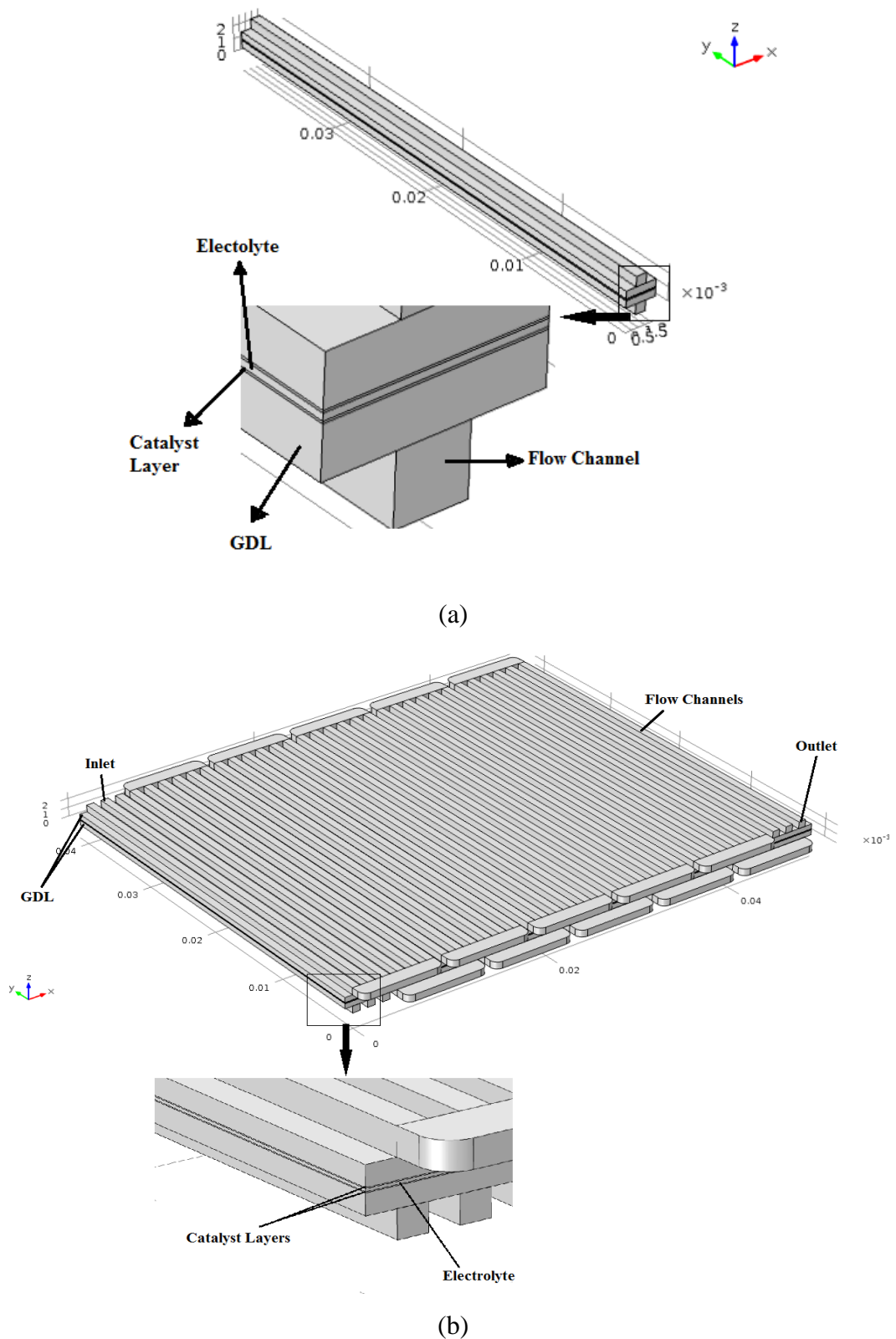
Figure 4.1 Components of the domain used in Comsol Multiphysics model (a) Single flow channel geometry (b) Triple mixed serpentine flow channel geometry

Table 4.1 The geometric properties of HT- PEM fuel cell used in the simulation

Description	Value	Units
Active Area	25	cm^2
Cell Length	4×10^{-2}	m
Channel Height	7.5×10^{-4}	m
Channel Width	7.5×10^{-4}	m
Rib Width	1.5×10^{-3}	m
GDL Width	5.5×10^{-4}	m
Electrode Thickness	2.5×10^{-5}	m
Membrane Thickness	7.5×10^{-5}	m

Table 4.2 General parameters used in simulation (Operation temperature is taken as 160^oC)

Description	Value	Units
GDL Porosity	0.5	-
GDL Permeability	3×10^{-12}	m^2
Inlet H_2O Mass Fraction(cathode)	0.001	-
Inlet O_2 Mass Fraction(cathode)	0.231	-
Anode Inlet Molar Flow Rate	7.71×10^{-5}	mol s^{-1}
Cathode Inlet Molar Flow Rate	3.05×10^{-4}	mol s^{-1}
Anode Inlet Flow Velocity	1.37	m s^{-1}
Cathode Inlet Flow Velocity	5.43	m s^{-1}
Anode Viscosity [53]	1.135×10^{-5}	kg m^{-1} s^{-1}
Cathode Viscosity [53]	2.464×10^{-5}	kg m^{-1} s^{-1}
Cell Temperature	433	K
Pressure	1.2×10^5	Pa
Cell Voltage	0.6	V
Oxygen Reference Concentration [22]	40.88	mol m^{-3}
Hydrogen Reference Concentration [22]	40.88	mol m^{-3}
Membrane Conductivity	19.06	S m^{-1}

4.2.1. Assumptions

- Steady state
- Laminar flow
- All reactants and products are in gaseous phase
- All gases and water obey the ideal gas law
- Operation is performed under isothermal conditions
- No crossover of gases and water through the membrane
- The physical properties of the components are constant
- GDL is composed of isotropic and homogeneous porous materials.

4.2.2. Equations

Basic conservation equations are used in order to obtain a mathematical model for the system. These are the conservation of mass, conservation of momentum and the conservation of charge. At this stage, conservation of energy is not used since the system is assumed to operate under isothermal conditions. For the simultaneous solution of these equations, the assumptions should be taken into account. Several simplifications can be done for the system components using these assumptions. The system is analyzed in three parts: flow channels, gas diffusion layers and the membrane. By the help of the assumptions and boundary conditions, the conservation equations for each compartment are obtained.

4.2.2.1. Flow Channel

Navier-Stokes equation for the incompressible mass transport in the flow channels and continuity equations can be applied for the system.

$$\rho(u.\nabla)u + \nabla p - \nabla.\mu(\nabla u + (\nabla u)^T) = 0 \tag{4.1}$$

$$\nabla.(\rho u) = 0 \tag{4.2}$$

where u is the velocity vector (m s^{-1}), ρ is the gas mixture density (kg m^{-3}), p is the pressure term (N m^{-2}) and μ is the dynamic viscosity of the mixture (kg m^{-1} s^{-1}).

Mass transport of each species can be explained by the general form of Maxwell-Stefan relation.

$$\nabla.\left[-\rho w_i \sum_j \left(D_{ij}\nabla x_j + (x_j - w_j)\frac{\nabla p}{p}\right) + \rho w_i u\right] = 0 \qquad (4.3)$$

where w_i the mass fraction of the species i in the mixture is, D_{ij} is the binary diffusion coefficient ($m^2 s^{-1}$).

4.2.2.2. Gas diffusion layer

Darcy's law can be used in order to explain the phenomena occurring in the gas diffusion layer. The generation term must be added to the Navier-Stokes equation.

$$\rho(u.\nabla)u + \nabla p - \nabla.\mu(\nabla u + (\nabla u)^T) = -\frac{\mu}{k_p}u \qquad (4.4)$$

where k_p is the permeabilityof gas diffusion layer (m^2). A charge balance must be performed in the GDL;

$$\nabla.\left(\kappa_s^{eff}\nabla\emptyset_s\right) = 0 \qquad (4.5)$$

where κ_s^{eff} is the effective ionic conductivity of the solid phase (S m^{-1}) and $\emptyset_s$ is the phase potential.

4.2.2.3. Catalyst Layer

In order to calculate the local current density, simplified Butler-Volmer equation for anode and cathode can be used;

$$i_a = i_a^{ex}\left(\frac{C_{H_2}}{C_{H_2}^{ref}}\right)^{0.5}\left[\frac{\alpha_a+\alpha_c}{RT}F\eta_a\right] = 0 \qquad (4.6)$$

$$i_c = i_c^{ex}\left(\frac{C_{O_2}}{C_{O_2}^{ref}}\right)\left[exp\left(-\frac{\alpha_c F\eta_c}{RT}\right)\right] = 0 \qquad (4.7)$$

where i_a and i_c are the transfer current density (A/m^2) corresponding to the electrochemical reaction at the anode and cathode catalyst layers, respectively;

C_{H_2} and C_{O_2} are the concentration (mol m^{-3}) for hydrogen and oxygen; η_a and η_c are the potential difference between solid matrix and the electrolyte; α_a and α_c are the transfer coefficients for anode and cathode.

4.2.2.4. Electrolyte

Crossover of gases through the membrane is neglected; therefore, only charge balance is considered for the electrolyte.

$$\nabla.(\kappa_e \nabla \emptyset_e) = 0 \qquad\qquad (4.8)$$

κ_e is the ionic conductivity (S m^{-1}) of the phosphoric acid doped PBI membrane and $\emptyset_e$ is the phase potential at the electrolyte.

4.2.3. Boundary Conditions

- Continuity at all boundaries
- No slip for all channel walls
- Suppress backpressure
- Constrain outer edges set to zero for both inlet and outlet
- Bipolar plates on the both side of the cell set to electric ground and cell operation potential

4.3. Results

4.3.1. Temperature Influence

Figure 4.2 illustrates the polarization curves of a single high temperature PEMFC simulated at different operating temperatures ranging from 100 °C to 180 °C. In order to decrease the computational time required by Comsol Multiphysics, 0.1 V sweep rate and single flow channel geometry are used to obtain the polarization curve. The anode and cathode feed are composed of hydrogen and air with the stoichiometric ratios of 1.5 and 2.5, respectively. Voltage vs current density plots coincide at high operating voltages down to 0.7 V, where temperature does not influence the average current density significantly. The drastic decrease in the

voltage is caused by the activation barrier of the chemical reaction taking place in the system within this region. The activation loss is not significantly affected by the operation temperature in the model; thus, the performance at low current densities is approximately the same for given temperature values.
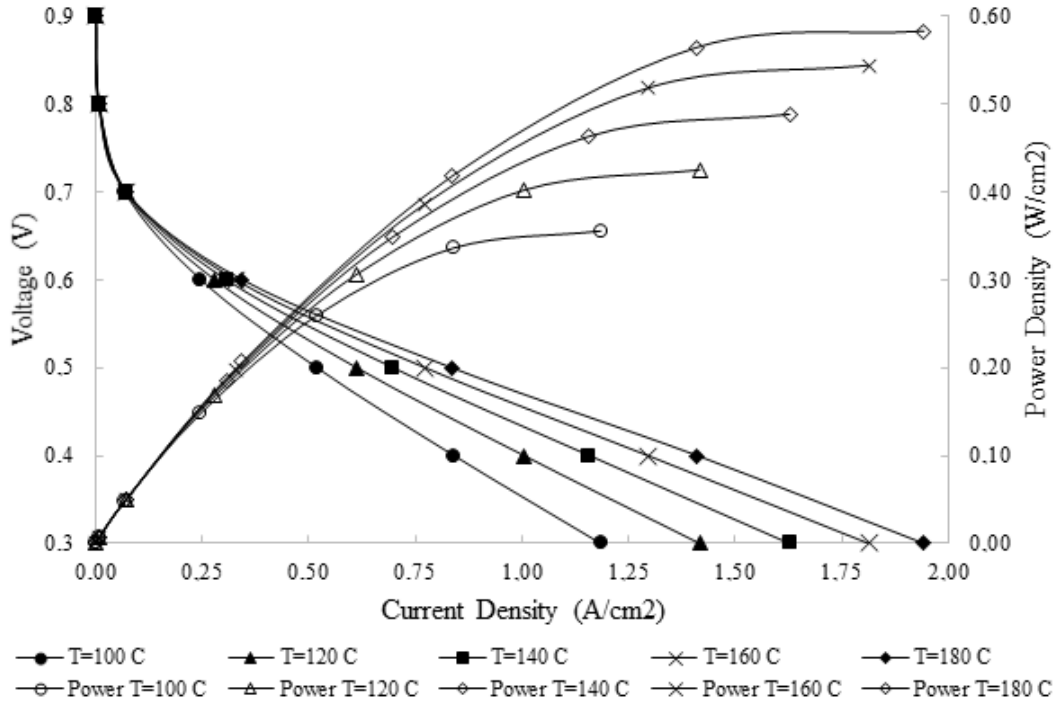
Figure 4.2 Simulated polarization curve of a single HTPEMFC obtained at different operating temperatures from single flow channel.

Ohmic losses which are the linear part of the polarization curve are mainly due to the membrane resistance; therefore, they are affected by the ionic conductivity of the membrane. It is known that the ionic conductivity of the membrane is function of temperature according to their proton migration mechanism. The following relation is suggested for phosphoric acid doped PBI membranes [9],

$$\kappa_e = \frac{A}{T} exp \left(\frac{-E_a}{R.T} \right) \tag{4.9}$$

where A is the pre-exponential factor (S m^{-1} K^{-1}), E_a is the proton conducting activation energy (J mol^{-1}), T is the temperature (K) and R is the ideal gas constant (J mol^{-1} K^{-1}). The PBI membrane ionic conductivities were reported as 7.2 S m^{-1} at

100 °C and 24.8 S m^{-1} at 180 °C [8]. The data are fitted to the Eq. 9, and the following empirical relation is obtained;

$$\kappa_e = \frac{8.88 \; X \; 10^6}{T} exp\left(\frac{-3022.6}{T}\right) \tag{4.10}$$

It can be seen that the current and power densities increase with increasing temperature which is similar to the results reported in the literature [16, 18-20]. The power density calculated at 0.5 V at 100 °C, 120 °C, 140 °C, 160 °C and 180 °C are 0.26 W cm^{-2}, 0.31 W cm^{-2}, 0.35 W cm^{-2}, 0.39 W cm^{-2} and 0.42 W cm^{-2}, respectively. The power density increase is 19% if the operation temperature is raised from 100 °C to 120 °C; however, it is 7.6% if the temperature is increased from 160 °C to 180 °C. The temperature effect on high temperature PEMFC performance is more pronounced at lower temperatures than at higher temperatures [20].

4.3.2. Model Validation

The polarization curves obtained for single flow channel model and triple mixed serpentine flow channel model are compared with experimental data in Figure 4.3. The experimental polarization data obtained by Danish Power Systems [51] were used to validate the presented two models. Data were taken from a single cell with an active area of 25 cm2 PBI membrane at 160 °C. Both the single flow channel and triple mixed serpentine flow channel models predict lower current densities for the operating voltages greater than 0.6 V. This deviation from experimental data can be easily seen at the operating voltage of 0.7 V. Experimental data show an average current density of 0.1 A cm^{-2} at 0.7 V; however, this value is 0.07 A cm^{-2} for the single flow channel model and 0.04 A cm^{-2} for the multiple flow channel model. This deviation from experimental data can be explained by the activation losses which are caused by the reaction kinetics. Better fit between the model and experimental results can be obtained by enhancing the kinetic parameters that are used in the model. By taking the operating voltage as 0.6 V, the predicted average current density for both models is 0.33 A cm^{-2}, which is very close to the experimental data 0.34 A cm^{-2}. For the operating voltages less than 0.6 V, there is a good agreement between the single flow channel model and the experimental data.

43

However, the triple mixed serpentine flow channel model predicts higher current densities than the experimental data. These deviations can be caused by the distribution of the current density. Figure 4.4 shows the current density distribution at 0.6 V for the triple mixed serpentine flow channel model. As it is seen in the figure, there are some points at which the local current density has very high values. The performance of triple mixed serpentine model does not coincide with the single channel other than 0.6 V. The difference in the performance of models can be explained by the difference in their flow channel geometries. In the single channel model, the flow is considered for a small area (0.9 cm^2); therefore, the concentration of oxygen in the cathode does not change significantly. In triple mixed serpentine geometry, the area is taken as 25 cm^2, therefore the oxygen concentration varies significantly. This difference in the concentration variation is highly pronounced and has a negative effect on the average current density at high voltages where kinetic losses are important.   Consideration of larger membrane area caused over estimation of current density at low voltages where the ohmic losses become significant. Therefore, the results of single flow channel model can be taken as a good approximation to investigate the influence of parameters.
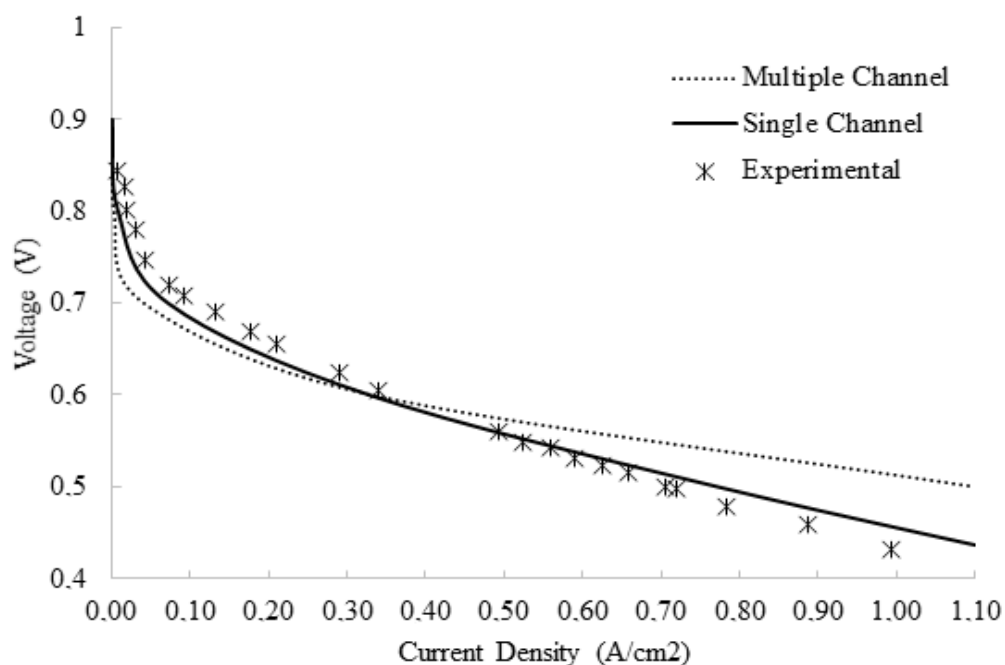
Figure 4.3 Comparison of single flow channel and triple mixed serpentine flow channel models with experimental data at 160 °C
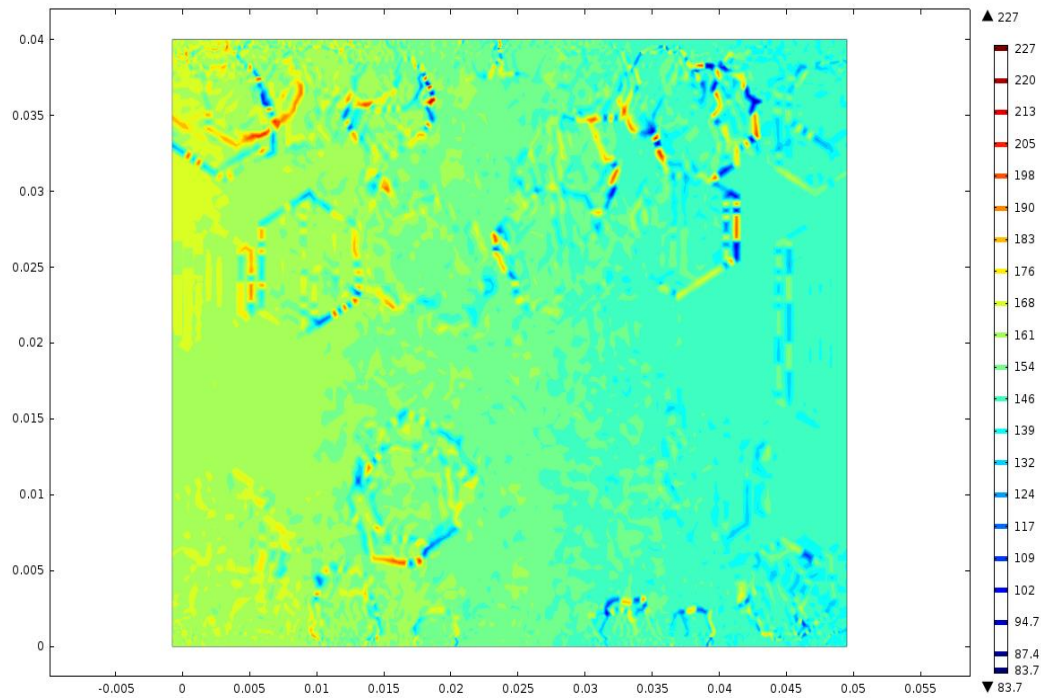
Figure 4.4 Predicted current density distribution at 160 ^{o}C and operating voltage of 0.6 V for triple mixed serpentine flow channel model

4.3.3. Transport Characteristics

The conditions that were used in the model validation section are used in order to investigate the transport characteristics. Figure 4.5 shows the pressure variation along the cathode and anode flow channels at 160 ^{o}C and operating voltage of 0.6 V. The pressure drop along the anode flow channels is 100 Pa and the pressure drop along the cathode flow channels is predicted as 1950 Pa. Although the pressures at both anode and cathode decreases, the pressure drop in the cathode compartment is much higher when it is compared to the pressure drop in the anode compartment. The cathode feed is composed of 21 % oxygen and 79 % inert gases; thus, the velocity of cathode feed is about four times higher than the velocity of the anode feed. Therefore, higher velocity in the cathode compartment caused a significant pressure drop in the cathode compartment.
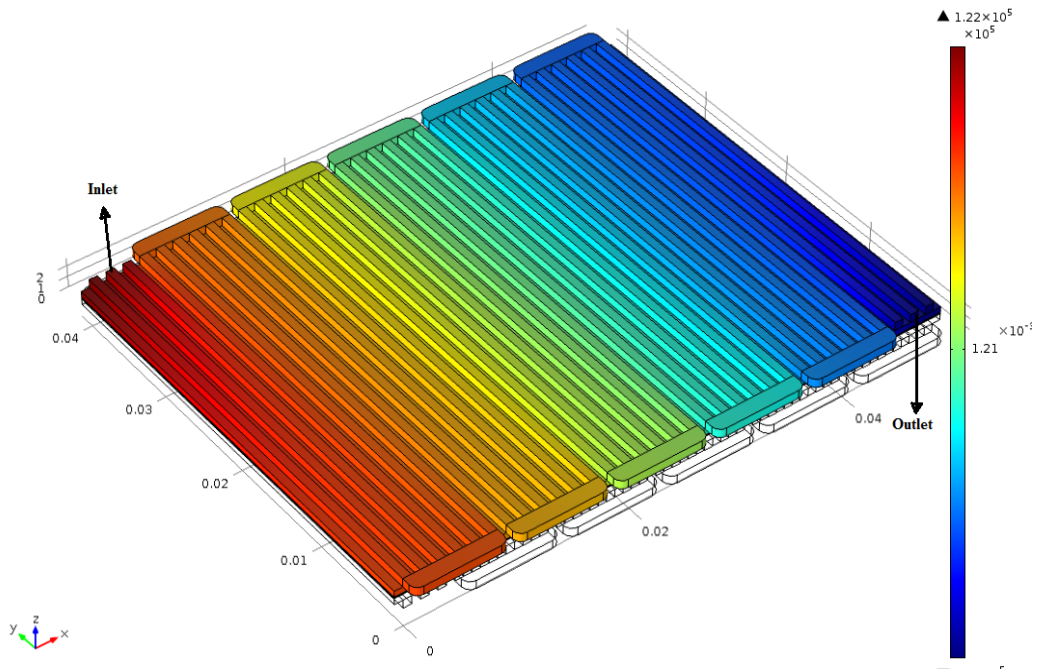
(a)
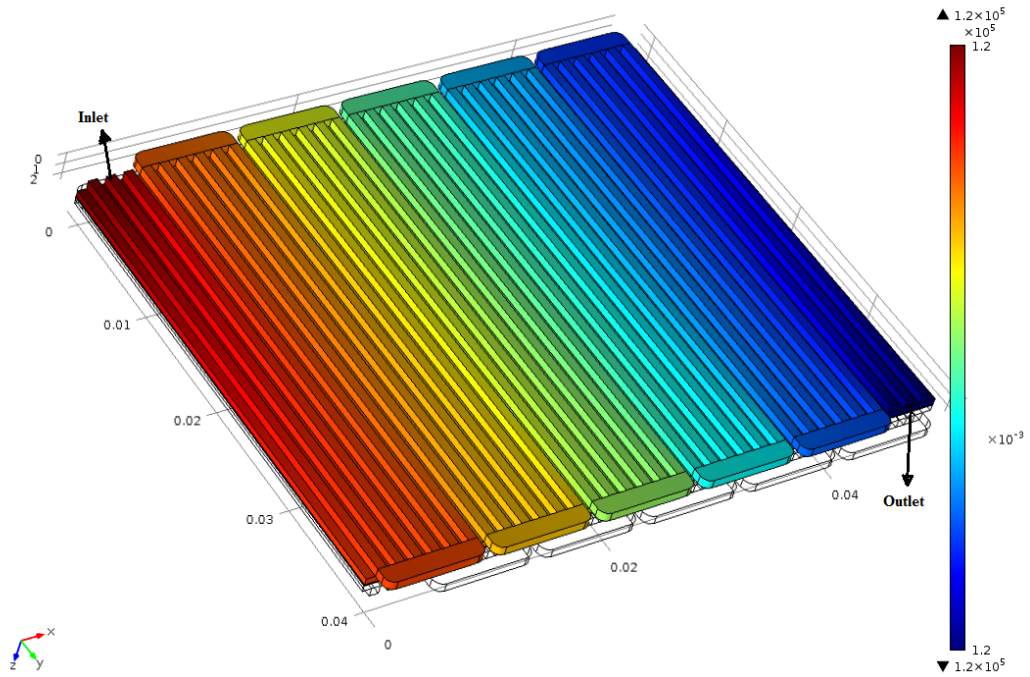
(b)

Figure 4.5 Pressure distribution at the flow channels at 160 °C and operating voltage of 0.6 V (a) cathode (1950 Pa pressure drop), (b) anode (100 Pa pressure drop)

Figure 4.6 shows the concentration profile of the oxygen at 160 °C and operating voltage of 0.6 V. Excess oxygen is fed to the system, since the stoichiometric ratio is taken as 2.5. Oxygen concentration decreases from 7 to 5.8 mol m^{-3}. Figure 4.7 shows the concentration profile of the water in the cathode flow channels. Water concentration increases from 0.05 to 2 mol m^{-3} since the reaction is occurring in the cathode compartment.
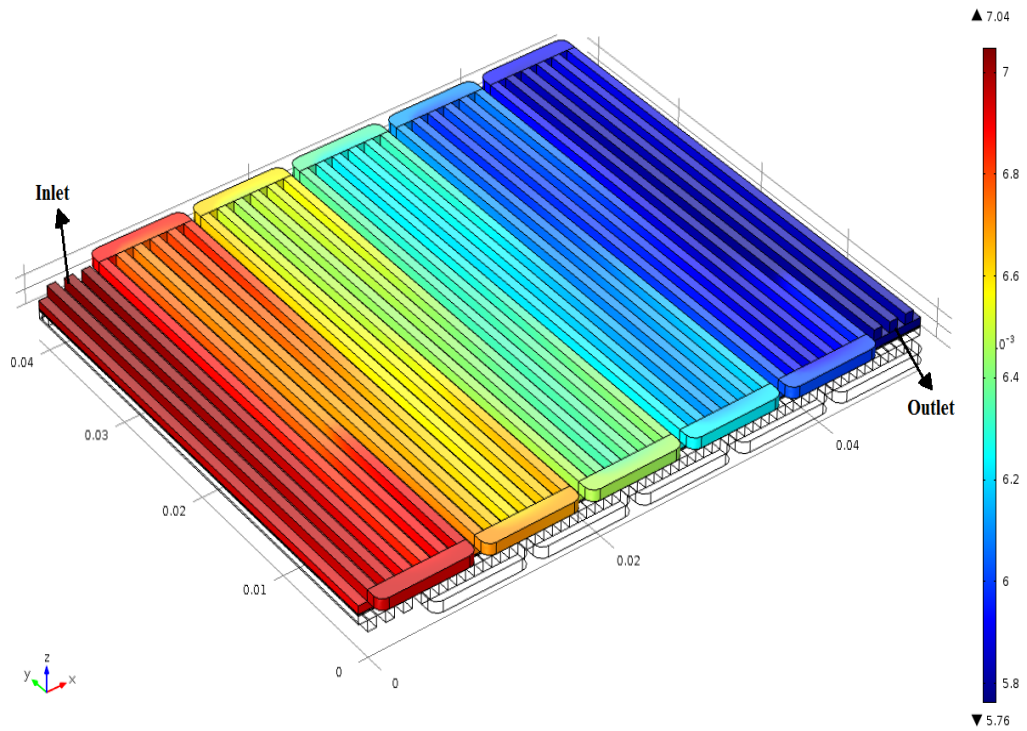
Figure 4.6 Concentration profile of the oxygen along the cathode flow channel operating at 160 °C and 0.6 V (mol m^{-3})
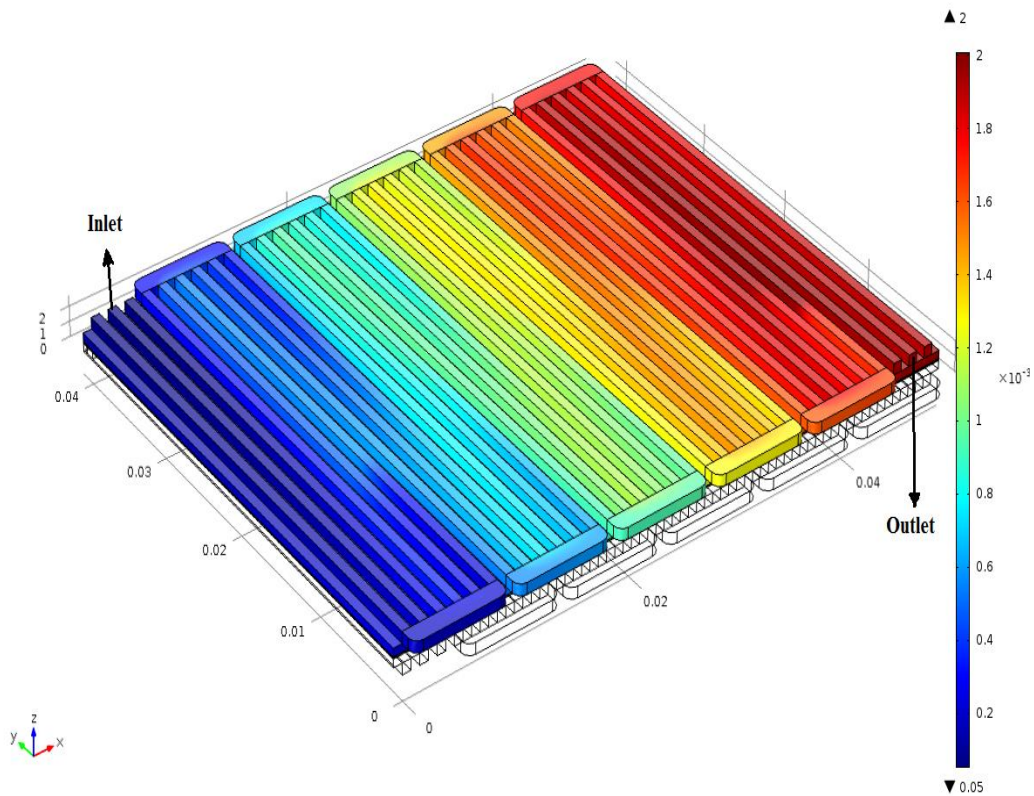
Figure 4.7 Concentration profile of the water along the cathode flow channel operating at 160 °C and 0.6 V (mol m^{-3})

Anode feed is composed of 99.999 % hydrogen and 0.001 % water. The mole fraction of the hydrogen does not change along the anode flow channel and also the concentration of the hydrogen remains as 33.3 mol m^{-3}. The insignificant change in the concentration is attributed to the small pressure drop (100 Pa) and the purity of hydrogen.

Three potential values were chosen at 160 °C and each generated local current density distribution at the electrolyte was presented in Figure 4.8. As expected, current density at 0.5 V has the highest values. Average current density on the surface is 500 A m^{-2}; however, the local current density reaches to 800 A m^{-2} at some points. The average current density at 0.7 V and 0.9 V are around 20 A m^{-2} and 1.7 A m^{-2}, respectively. The concentration has a crucial role in the local current density calculation. Thus, the highest current density is observed at the inlets. The change in the concentration is recognizable at 0.5 V due to the consumption of the reactants;

48

therefore, the variation in the local current density distribution along the flow channels becomes apparent at that voltage. As the operating voltage decreases, non-uniformities in the local current density distribution increase.
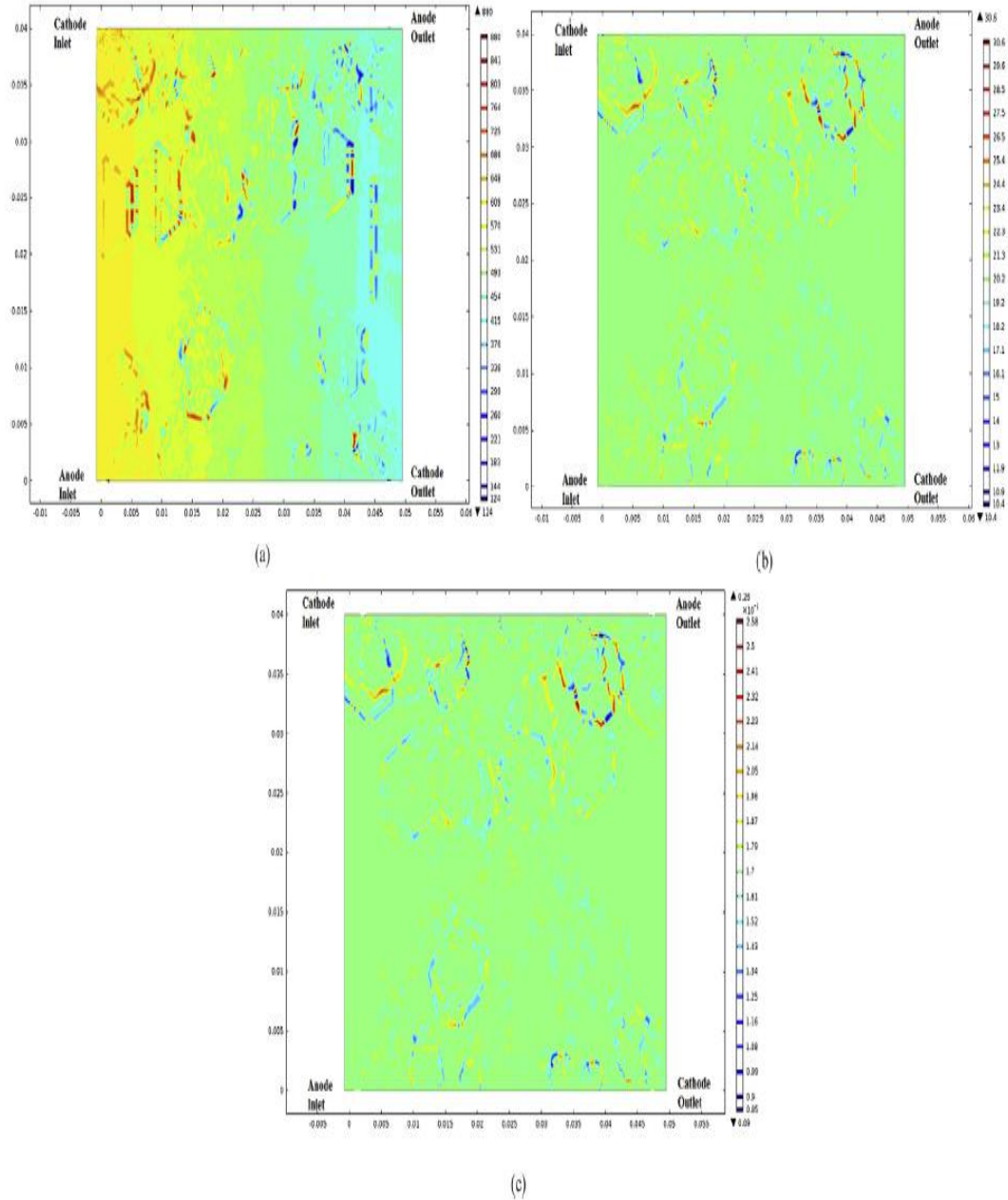
Figure 4.8 Predicted current density distribution at 160 °C operating temperature
(a) V=0.5 V (b) V=0.7 V (c) V=0.9 V

4.4. Conclusion

A three-dimensional model for the high temperature PEMFC having an active area of 25 cm^2 is developed. A single cell with phosphoric acid doped PBI membrane is used in the model. The flow channel geometry is taken as triple mixed serpentine. Steady-state, isothermal, single phase are the main assumptions for the model. The model predicts the polarization plot, concentration profile of each species within the system and pressure distribution. A single flow channel model is used to investigate the effect of the operation temperature on the performance of the fuel cell. The temperature range is taken as 100-180 ^{o}C. It is seen that increasing temperature results in an enhancement in the cell performance. This is mainly because of the faster reaction kinetics and higher membrane proton conductivity. The predicted power densities at 0.5 V at 100 ^{o}C, 120 ^{o}C, 140 ^{o}C, 160 ^{o}C and 180 ^{o}C are   0.26 W cm^{-2}, 0.31 W cm^{-2}, 0.35 W cm^{-2}, 0.39 W cm^{-2} and 0.42 W cm^{-2}, respectively. The temperature influence on high temperature PEMFC performance is more pronounced between 100-120 ^{o}C than between 160-180 ^{o}C.   The experimental data validate both the single channel and the triple mixed serpentine flow channel models at 0.6 V and 160 ^{o}C. The difference in performance curves were mainly caused by the active area taken into account. Larger membrane area caused over estimation of current density at low voltages where the ohmic losses become significant. Therefore, the results of single flow channel model can be taken as a good approximation to investigate the influence of parameters. The predicted current density distribution obtained at different operating voltages   show that at high operating voltages the local current density is almost uniform; whereas, decreasing operating voltage causes non-uniformities in the local current density.

CHAPTER 5

5. EFFECT OF KEY PARAMETERS ON THE PERFORMANCE OF THREE-DIMENSIONAL ISOTHERMAL MODEL

The electrochemical properties of Membrane Electrode Assembly (MEA highly depend on the manufacturing process, especially the conditions employed during the synthesis of the PBI membrane. The change in the proton conductivity of PBI membrane altered the conditions used in the modeling and performance tests. In Chapter4, the performance data of a commercial MEA produced by Danish Power Systems has been taken into consideration for the verification of the model. In the scope of this chapter, the change in the model results with use of PBI membrane being developed by FCRC team is studied. Therefore, a new model is developed to analyze HT-PEMFC in which PBI membrane having lower proton conductivity. PBI membrane used as electrolyte in HT-PEMFC system is synthesized by Devrim et al. [30].The experimental procedure is given in detail in Appendix C. In this chapter the influence of flow channel geometry on the performance of HT-PEMFC is also studied by comparing the model results of triple mixed serpentine and serpentine flow channel geometries.

5.1. Influence of Operation Temperature on the Performance

Proton conductivities of PBI membrane were reported as 6.08 S m^{-1} at 140 $^{\circ}$C, 7.11 S m^{-1} at 165 $^{\circ}$C and 9.41 S m^{-1} at 180 $^{\circ}$C [30]. The dependence of proton conductivity on the temperature is given by the Equation 4.9. Figure 5.1 illustrates the temperature dependency of the data by the linear fit. The linearized form of Eqn. 4.9 is given as;

$$\ln(\kappa_e T) = \ln A - \frac{-E_a}{R.T} \qquad (5.1)$$
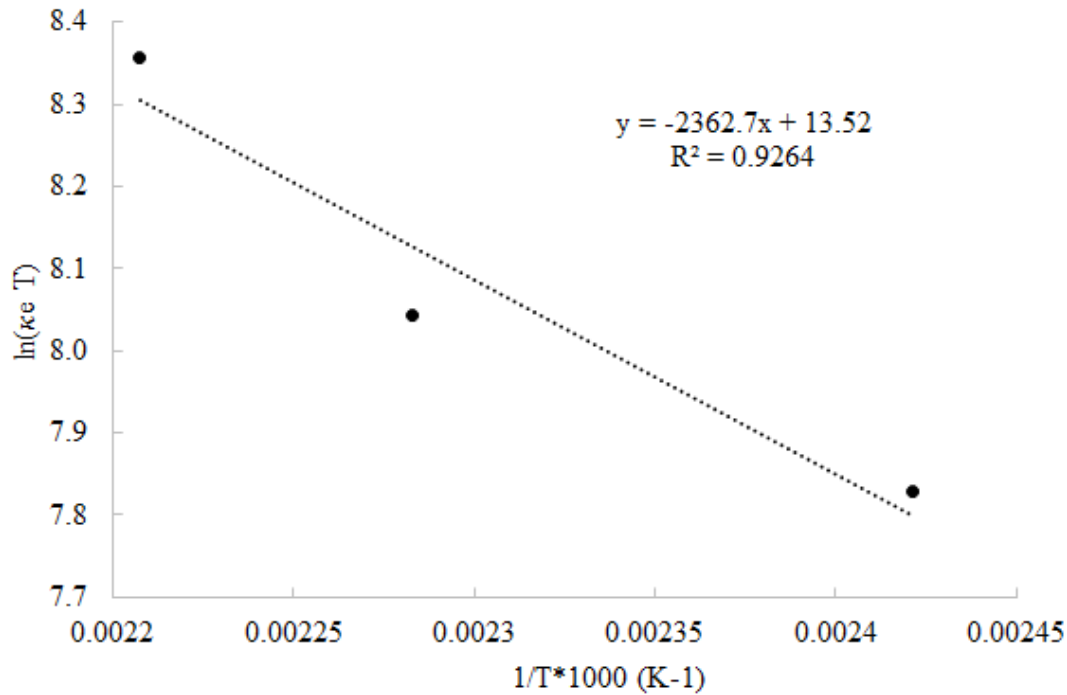
Figure 5.1 Temperature dependence of proton conductivity

When the data are fitted to determine the proton conductivity of PBI membrane at different operation temperatures, the following empirical relation is obtained;

$$\kappa_e = \frac{7.44 \; X \; 10^5}{T} exp\left(\frac{-2362.7}{T}\right) \tag{5.2}$$

The pre-exponential factor for PBI membrane is found as $7.44 \; x \; 10^5$ S m^{-1} K^{-1}; whereas, the activation energy is determined to be 19.6 kJ mol^{-1} K^{-1}. Figure 5.2 shows the change in the proton conductivity of commercial and developing PBI membranes at different temperatures. The commercial membrane has higher proton conductivity; moreover, it is highly affected by the temperature. On the other hand, the proton conductivity of developing PBI membrane is not high. Its value is not significantly affected by the temperature. In their study, Sezgin et al. [51] investigated the influence of membrane proton conductivity on the performance of the HT-PEMFC by changing the proton conductivity between 10 to 20 S m^{-1}. The best match between the model results and experimental data was observed when the proton conductivity is taken as 14 S m^{-1}. It can be concluded that the proton conductivity of the electrolyte affects the performance, especially by decreasing the

ohmic losses and shifting the performance upwards. Therefore, proton conductivity has an important role in the performance of HT-PEMFC.
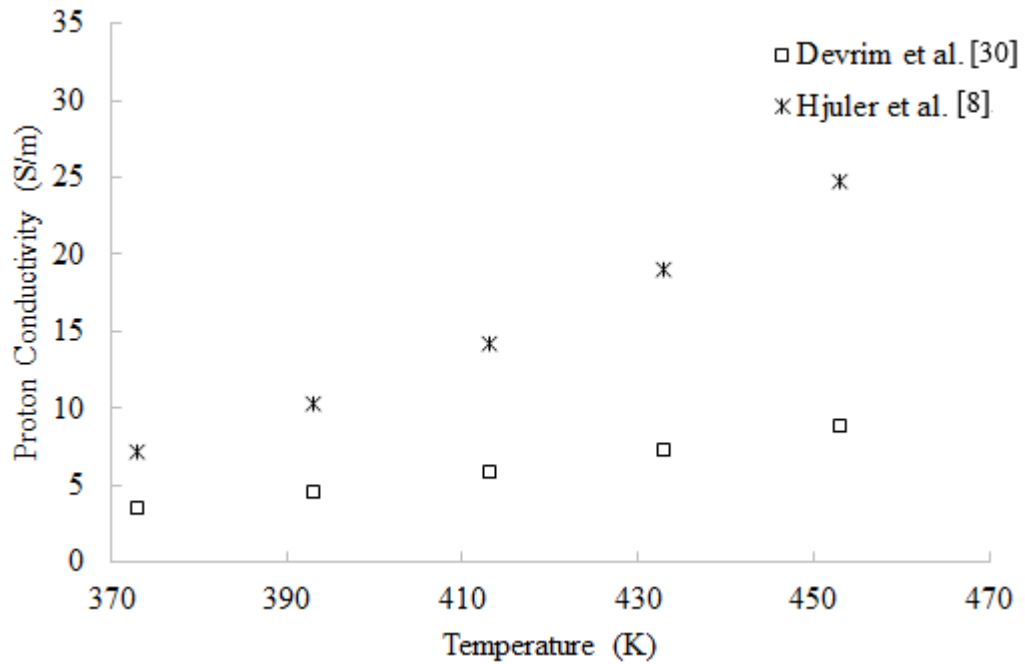
Figure 5.2 Proton conductivity of commercial and developing PBI membranes

Table 5.1 shows the data used in the model in order to investigate the effect of the temperature on the performance of HT-PEMFC with developing MEA. The inlet velocities of the anode and cathode compartments are different than the ones given in Table 4.2, since the domain has been changed. In the current model, inlet manifolds are also taken into account. The velocity of gases are affected by the inlet cross-sectional area of the anode and cathode compartments, because the volumetric flow rates are same in both models. For specified active area, which has a value of 25 cm^2, the molar flow rates of the reactants and inlet volumetric flow rates are the same since inlet conditions do not change. Different cross-sectional area yields in difference in the inlet velocities of reactants fed to the anode and cathode compartment.

Table 5.1 Parameters used in the model of HT-PEMFC with developing MEA

Description	140 °C	165 °C	180 °C
GDL Porosity (-)	0.5	0.5	0.5
GDL Permeability (m^2)	3 x 10^{-12}	3 x 10^{-12}	3 x 10^{-12}
Anode Inlet Flow Rate (mol s^{-1})	7.71x10^{-5}	7.71x10^{-5}	7.71x10^{-5}
Cathode Inlet Flow Rate (mol s^{-1})	3.05x10^{-4}	3.05x10^{-4}	3.05x10^{-4}
Anode Inlet Velocity (m s^{-1})	0.832	0.882	0.913
Cathode Inlet Velocity (m s^{-1})	3.295	3.494	3.614
Anode Viscosity (kg m^{-1} s^{-1}) [53]	1.101x10^{-5}	1.144x10^{-5}	1.169x10^{-5}
Cathode Viscosity (kg m^{-1} s^{-1}) [53]	2.382x10^{-5}	2.465x10^{-5}	2.545x10^{-5}
Cell Temperature (K)	413	438	453
Outlet Pressure (Pa)	1.2x10^5	1.2x10^5	1.2x10^5
Cell Voltage (V)	0.6	0.6	0.6
O$_2$ Ref. Concentration(mol m^{-3})[22]	40.88	40.88	40.88
H$_2$ Ref. Concentration (mol m^{-3})[22]	40.88	40.88	40.88
Membrane Conductivity (S m^{-1})	6.08	7.11	9.41

Figure 5.3 shows the polarization curves obtained by using the proton conductivity values 6.08 S m^{-1} at 140 °C, 7.11 S m^{-1} at 165 °C and 9.41 S m^{-1} at 180 °C. For the operation voltage larger than 0.6 V, the performance of HT-PEMFC do not affected by operation temperature. On the other hand, the performance of HT-PEMFC differs as the operation voltage decreases. At 180 °C, there is a substantial decrease in the performance. The expected trend is not achieved in the current model, in which developing MEA is used. This trend can be explained by the proton conductivity of commercial and developing PBI membranes, since the latter is not affected by the temperature as the commercial one. This may result in an insignificant change in the ohmic losses, since change in the proton conductivity of the electrolyte differs slightly. However, the difference in the performance is observed especially at higher current densities. At this region, the mass transport limitation becomes dominating. The maximum performance is obtained at the operation temperature of 165 °C and

the minimum performance is obtained at 180 °C. This results can be explained by the physical parameters used in the modeling. As the operation temperature increases viscosity and velocity of the gases increase. At higher operation temperatures, the cathode feed is insufficient to attain higher fuel cell performance. This results in a decrease in the fuel cell performance at 180 °C.
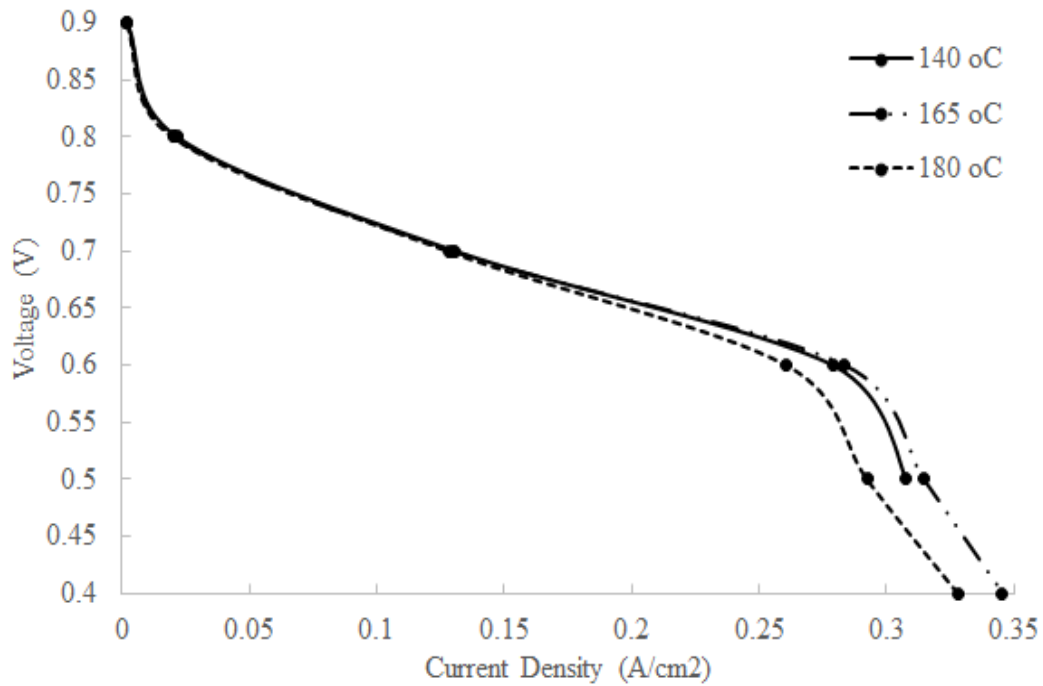
Figure 5.3 Polarization curve of models obtained for different operation temperatures for triple mixed serpentine models at 1.2 bar

Figure 5.4, Figure 5.5 and Figure 5.6 shows the pressure variation along cathode flow channels at the operation voltage 0.6 V. The pressure drop values are determined as 6007 Pa, 6383 Pa and 6065 Pa at 140 °C, 165 °C and 180 °C, respectively. Although the pressure drop increases as the operation temperature is increased from 140 °C to 165 °C, there is a decrease in the pressure drop when the operation temperature is increased from 165 °C to 180 °C. These pressure drop values directly affect the fuel cell performance as it is seen from Figure 5.3.
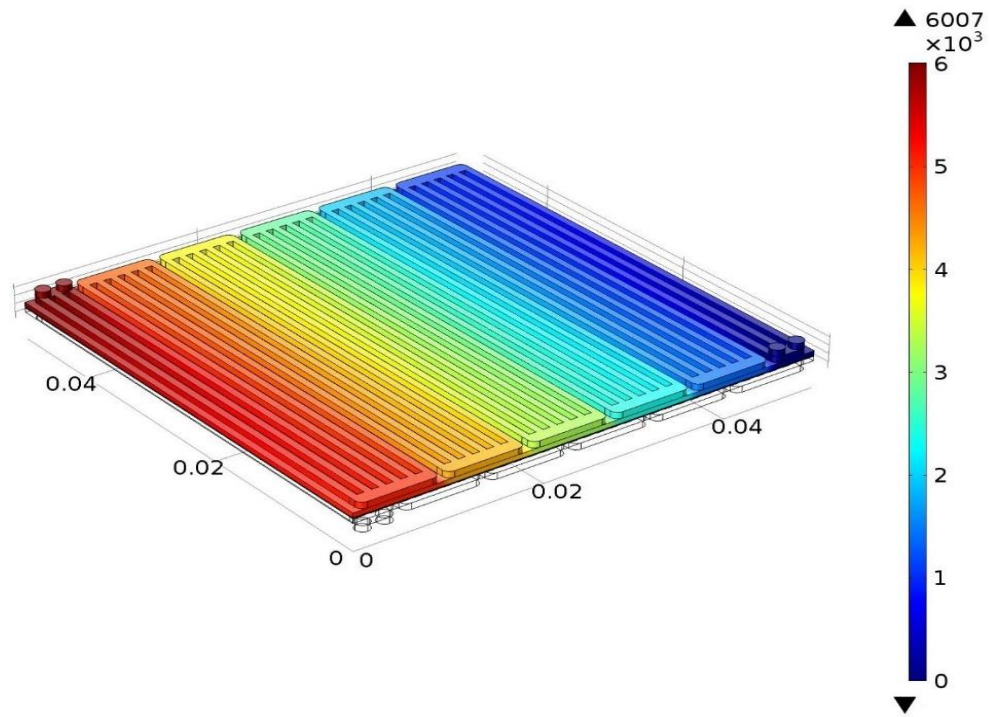
Figure 5.4 Pressure profile along cathode flow channels at V=0.6 V and 1.2 bar
backpressure at 140 °C
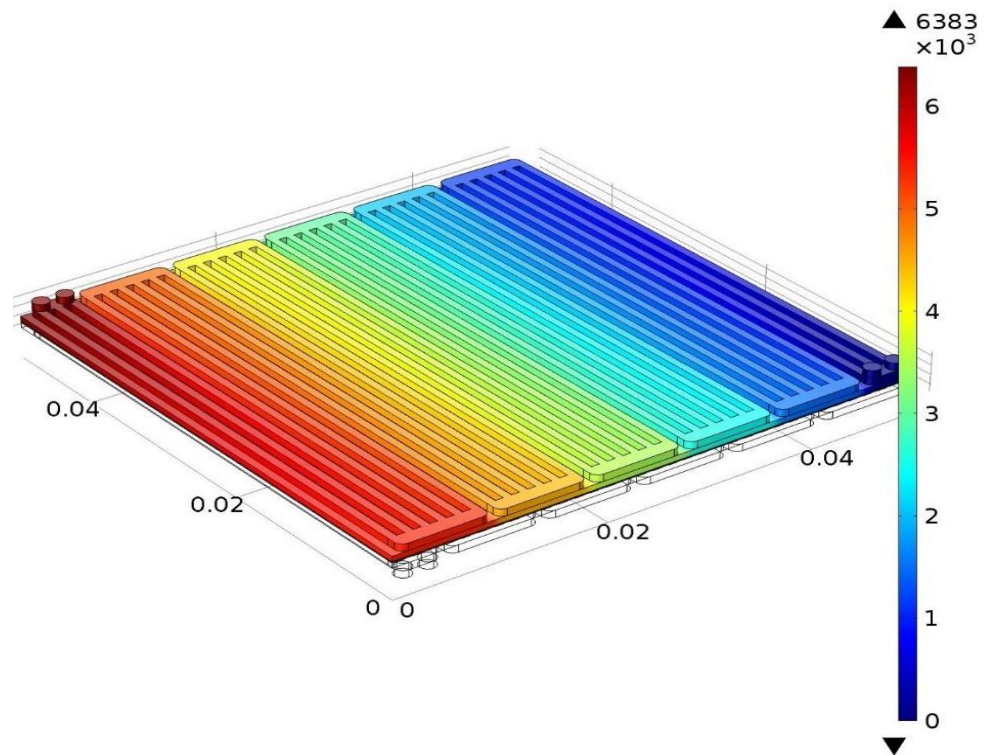
Figure 5.5 Pressure profile along cathode flow channels at V=0.6 V and 1.2 bar
backpressure at 165 °C
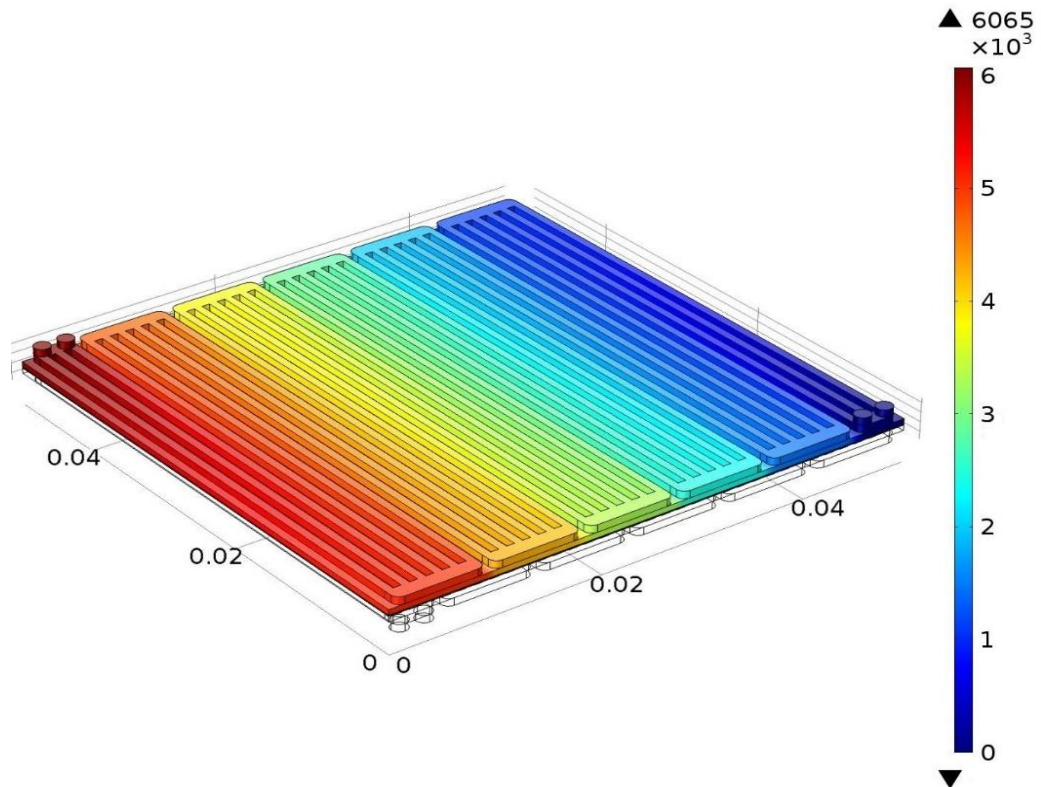
Figure 5.6 Pressure profile along cathode flow channels at V=0.6 V and 1.2 bar
backpressure at 180 °C

5.2. Influence of Operation Pressure on the Performance

Effect of operation pressure on the fuel cell performance is investigated for triple
mixed serpentine model at the operation temperature of 165 °C. Figure 5.7 shows
the performance of triple mixed serpentine model at different operation pressures,
which are 1.2 bar, 2 bar and 3 bar. These values are defined as the outlet pressure of
anode and cathode flow channels. Pressure is directly related to the concentration of
the reactants since ideal gas assumption is employed for the system. Increasing
pressure results in higher concentration of reactants, which directly effects the
concentration terms in the Butler-Volmer equation.
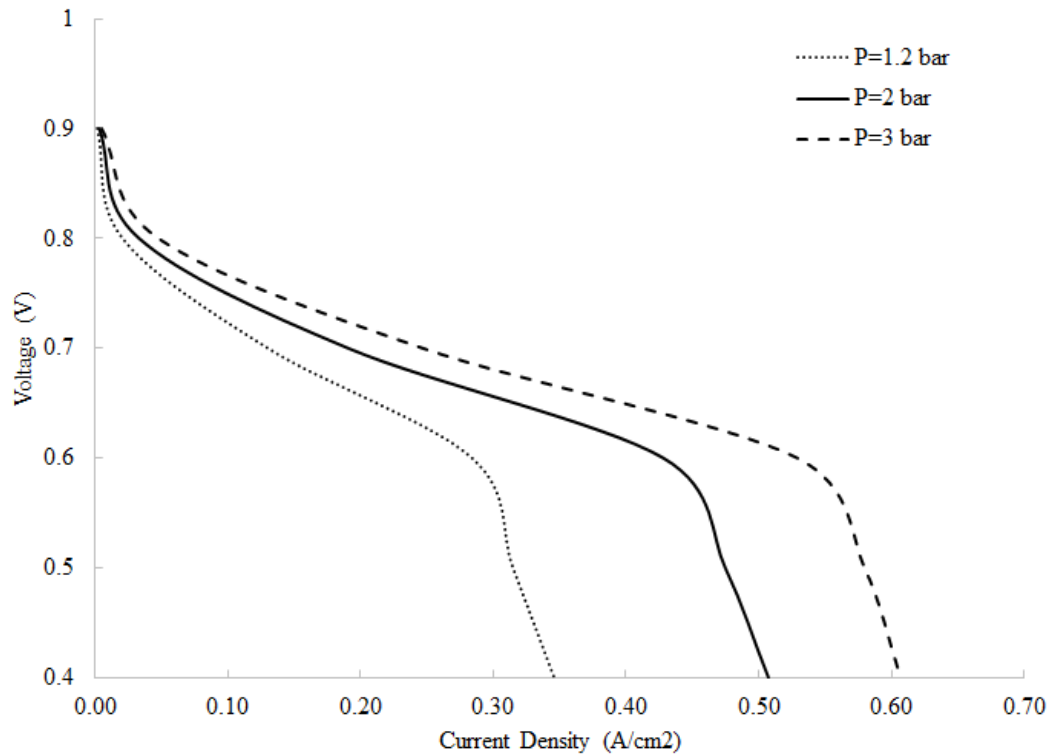
Figure 5.7 Polarization curve obtained at different operation pressures at 165 °C

5.3. Pressure and Concentration Profiles at Different Operation Voltages

Figure 5.8, Figure 5.9 and Figure 5.10 depict the change in the pressure along the cathode flow channels at different operation voltages. It is concluded that as the operation voltage decreases, the pressure drop along the flow channels increases. ΔP values for the cathode side is determined as 6414 Pa, 6383 Pa and 6260 Pa at 0.4 V, 0.6 V and 0.8 V, respectively. As the operation voltage decreases more oxygen is consumed. Half mole of oxygen produce one mole of water; therefore, total molar flow rate increases. Consecutively, the volumetric flow rate increases with the increasing number of moles. Higher volumetric flow rates yields in higher velocities along the flow channels. The pressure drop increases as the velocity of gases increases. This situation takes place especially when the operation voltage decreases, since the amount of consumed oxygen is proportional to the current and inversely proportional to the operation voltage. Therefore, decreasing operation voltage increases the pressure drop along the flow channels.

58
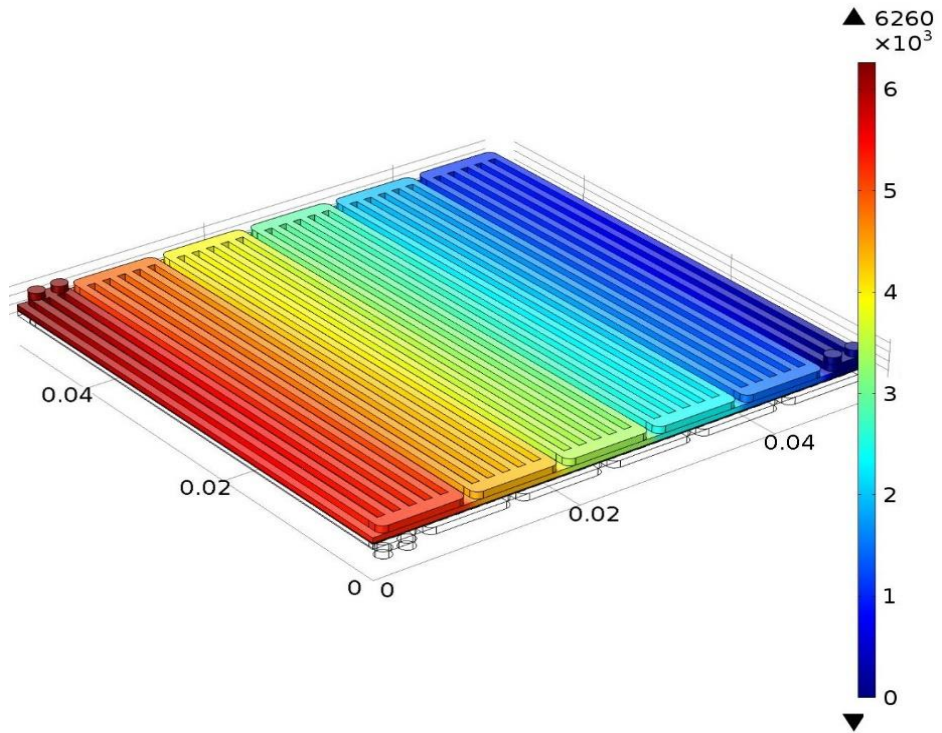
Figure 5.8 Pressure profile along the cathode flow channels at 165 °C, 0.8 V and 1.2 bar (absolute, Pa)
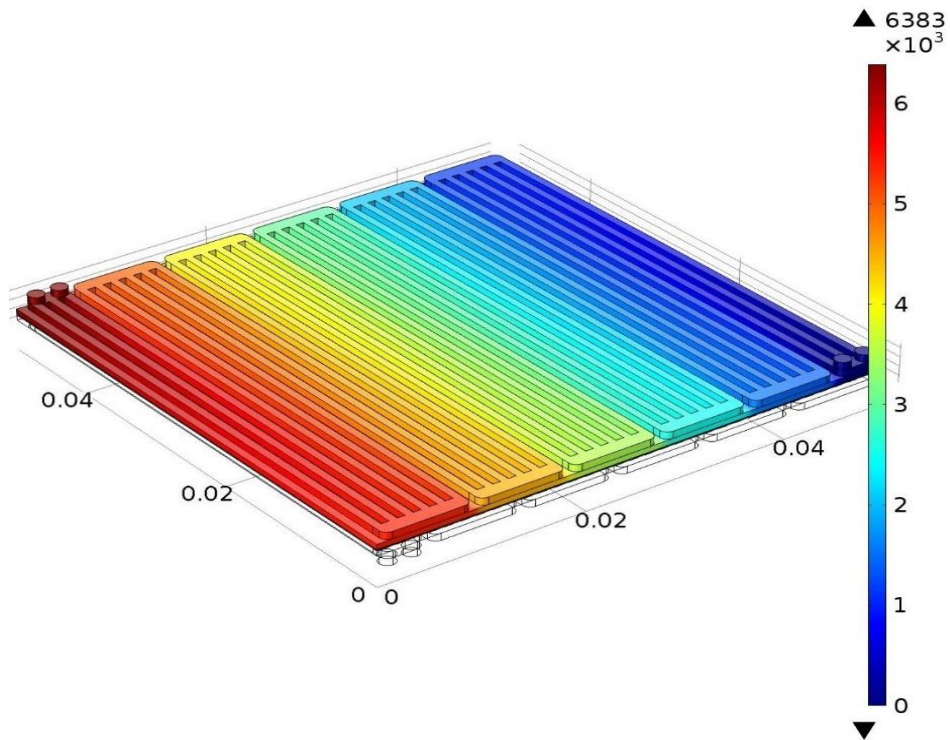
Figure 5.9 Pressure profile along the cathode flow channels at 165 °C, 0.6 V and 1.2 bar (absolute, Pa)
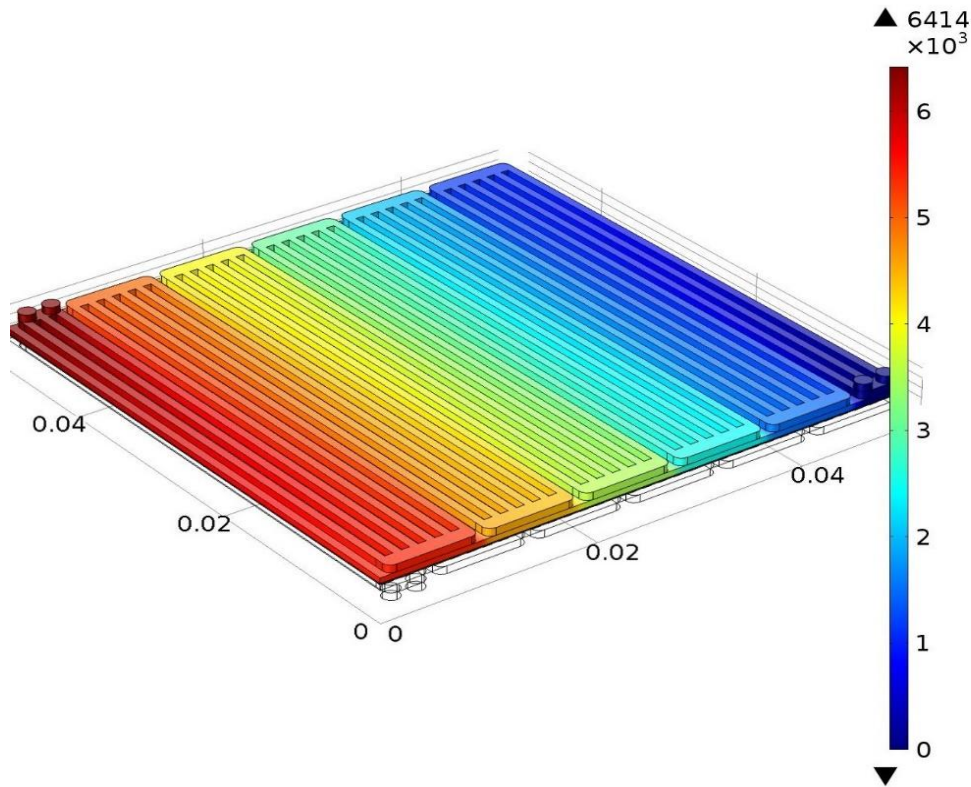
Figure 5.10 Pressure profile along the cathode flow channels at 165 °C, 0.4 V and 1.2 bar (absolute, Pa)

Change of oxygen concentration along the cathode flow channels at different operating voltages can be seen from Figure 5.11, Figure 5.12 and Figure 5.13. The rapid decrease in the concentration at 0.4 V is because of high current density at the inlet region. The change in the concentration is smoother when it is compared with the 0.4 V, since the average and local current density values at the inlet region is much more less. There is a steady decrease in the concentration along the flow channels at 0.8 V. The concentration change is not significant at 0.8 V, since the amount of reacted gas is less compared to the lower operation voltages resulting in an insignificant difference between inlet and outlet concentrations.
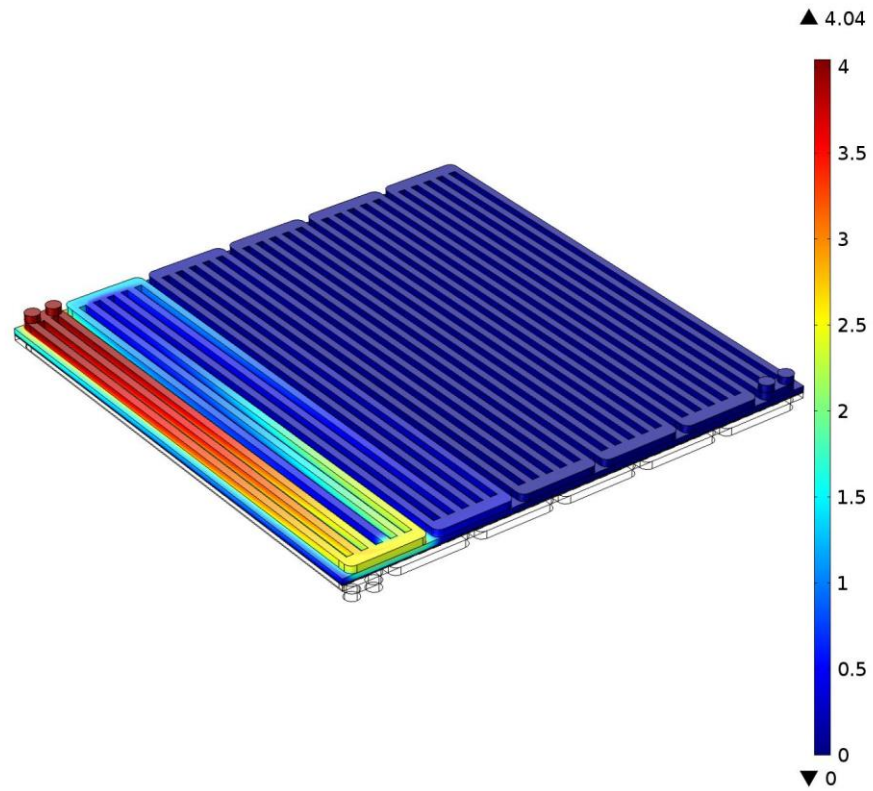
Figure 5.11 Oxygen concentration along cathode flow channels 0.4 V and 1.2 bar backpressure (mol m^{-3})
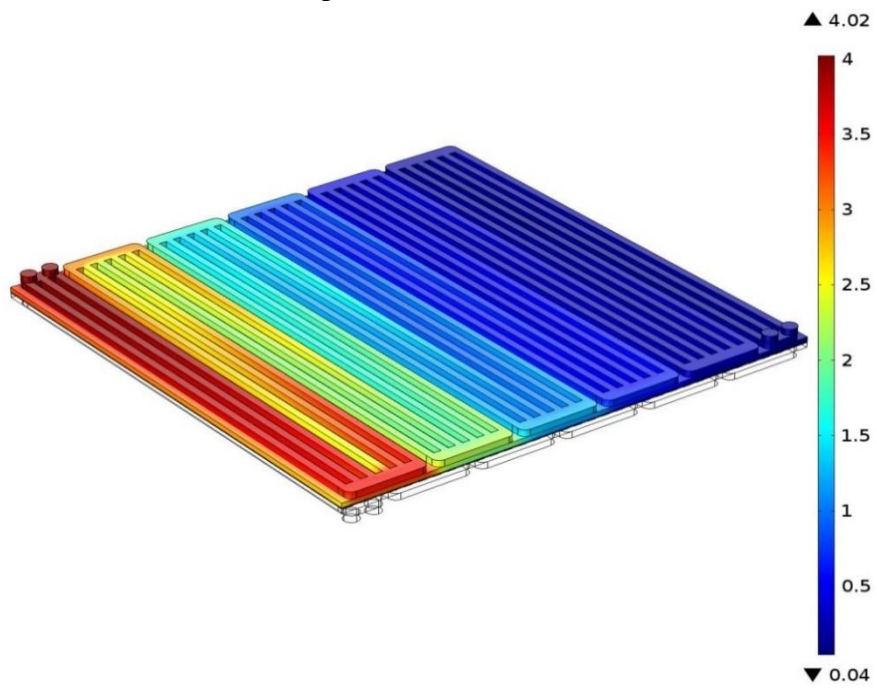
Figure 5.12 Oxygen concentration along cathode flow channels at 0.6 V and 1.2 bar backpressure (mol m^{-3})
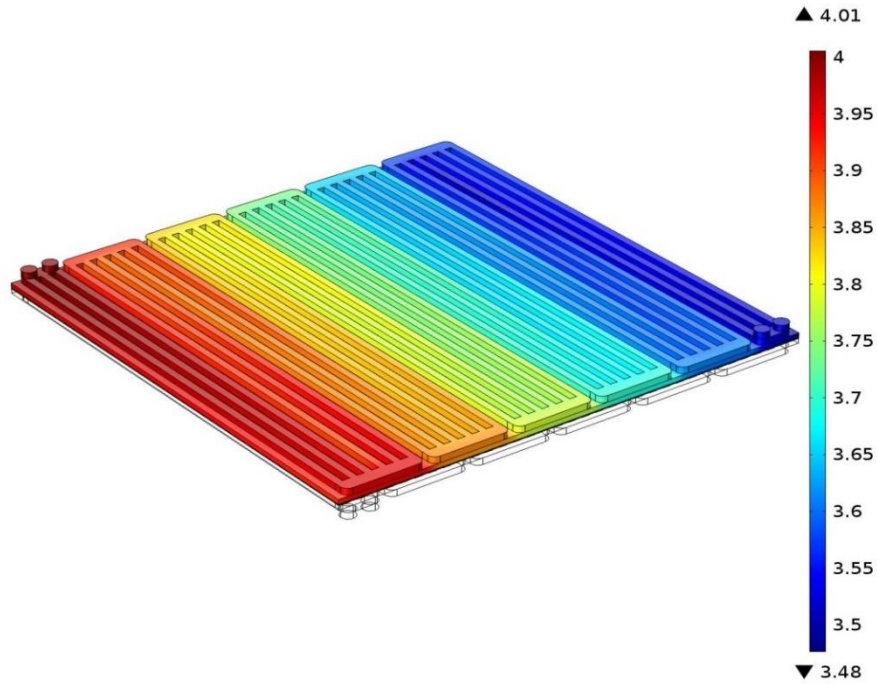
Figure 5.13 Oxygen concentration along cathode flow channels at 0.8 V and 1.2 bar backpressure (mol m^{-3})

The current density distributions at different operating voltages are given in Figure 5.14, Figure 5.15 and Figure 5.16. The current density distribution at high operating voltages is almost uniform; on the other hand, there is a continuous change in the current density at 0.6 V along the flow channels. The red part, which is the highest current density region, corresponds to the anode and cathode inlet. The decrease in the current density is due to the decrease in the concentration of species. Reactants are consumed very fast due to the higher current density at 0.4 V; however, the drastic decrease in the reactant concentration yields in lower current density and non-uniform distribution along the channels.
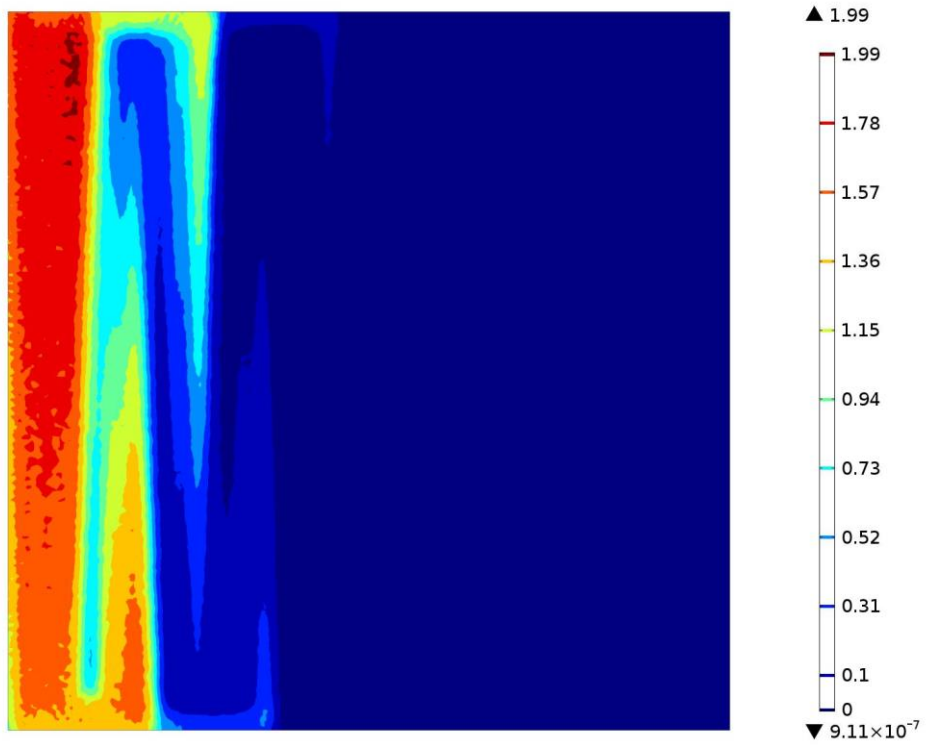
Figure 5.14 Membrane current density distribution at 165 °C, 1.2 bar and 0.4 V (A cm^{-2})
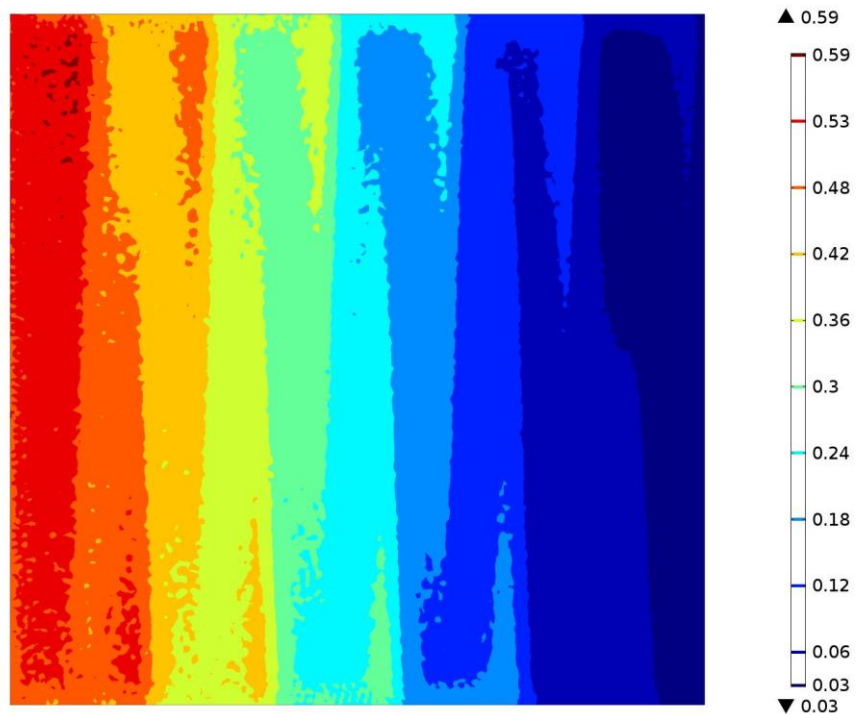
Figure 5.15 Membrane current density distribution at 165 °C, 1.2 bar and 0.6 V (A cm^{-2})
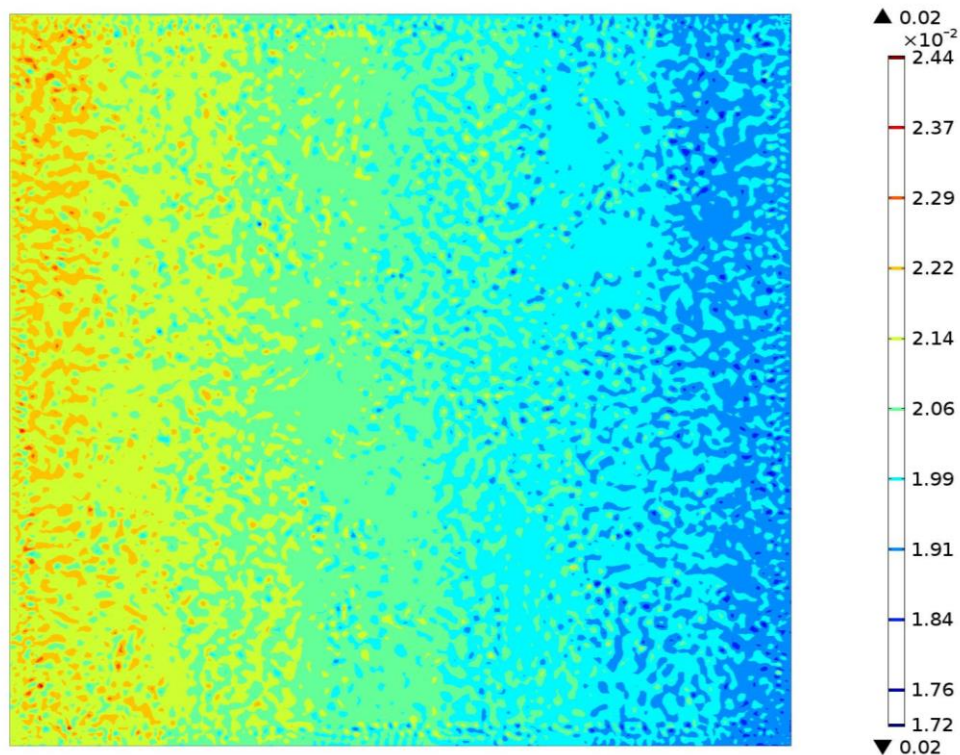
Figure 5.16 Membrane current density distribution at 165 °C, 1.2 bar and 0.8 V (A cm^{-2})

5.4. Influence of Flow Channel Geometry on the Performance

In order to observe the effect of flow channel geometry on the fuel cell performance, two HT-PEMFC models having an active area of 25 cm^2 are built. The flow channel geometries are determined as triple mixed serpentine and serpentine. Figure 5.17 illustrates the comparison of the performances of the fuel cell models with triple mixed serpentine and serpentine flow channel. It is seen that the performances of both cells do not differ significantly at high operation voltages; on the other hand, the performance of serpentine model gives higher current density at low operation voltages compared to the triple mixed serpentine. The concentrations of reactant gases in triple mixed serpentine are not sufficient especially at higher current densities, resulting in a drastic drop in the performance.
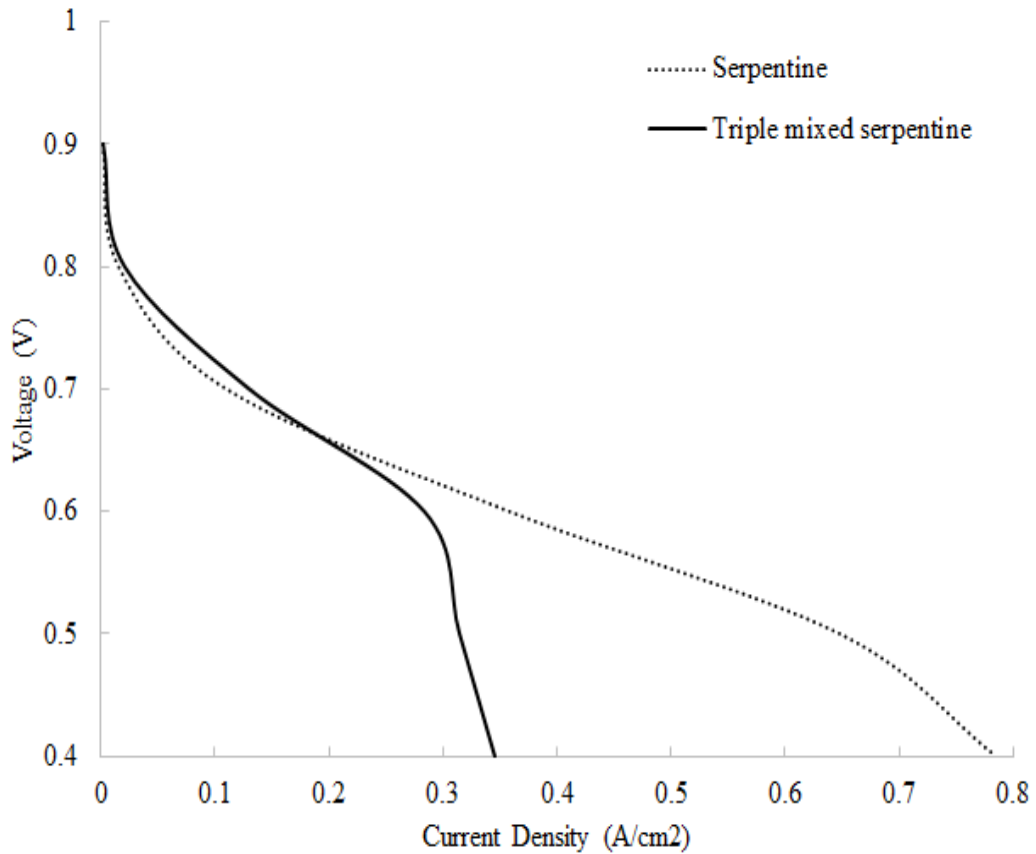
Figure 5.17 Polarization curve for triple mixed serpentine and serpentine models at 1.2 bar and 165 °C

5.5. Model Results of Serpentine Flow Channel

Figure 5.18 reveals the comparison of experimental data with model results of serpentine flow channel geometry. As it is seen this figure, serpentine flow channel model results gives better match with the experimental data [51]. Therefore, serpentine flow channel model can be taken as a good approximation for the performance of HT-PEMFC with commercial MEA.
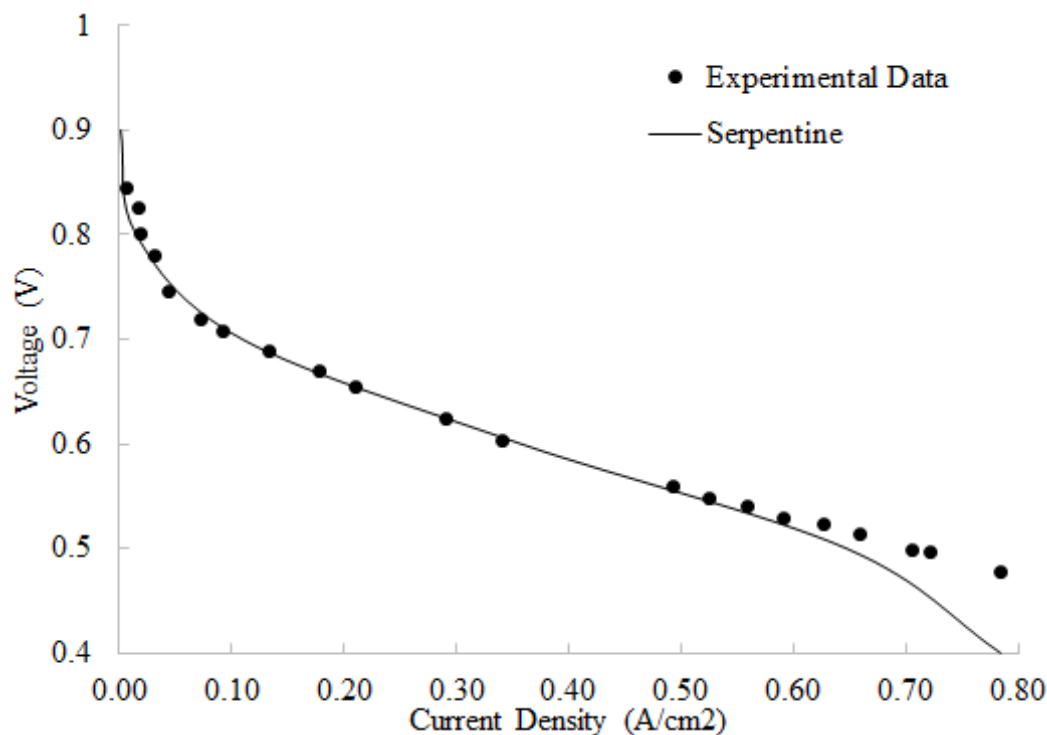
Figure 5.18 Comparison of serpentine model results with experimental data at 165 °C

Figure 5.19 shows the change in the pressure along the cathode flow channels. The pressure drop at the cathode compartment is found as 925 Pa. The pressure drop for the triple mixed serpentine flow channel geometry is approximately 6383 Pa with same molar flow rate. The lower pressure drop in the serpentine flow channel geometry is mainly caused by the lower velocity of gases. Volumetric flow rate of inlet gas streams are the same both for triple mixed serpentine and serpentine flow channel geometries, since the inlet conditions such as temperature and pressure are the same. Therefore, the inlet velocity of the anode and cathode compartments are calculated by dividing the volumetric flow rate of reactants to the cross-sectional area of the flow channels. In the triple mixed serpentine model, the inlet velocity is much higher than the serpentine model. Moreover, shorter path is followed in serpentine flow channel geometry compared to triple mixed serpentine. Both higher velocity and longer path yield in higher pressure drop in triple mixed serpentine flow channel geometry.

66
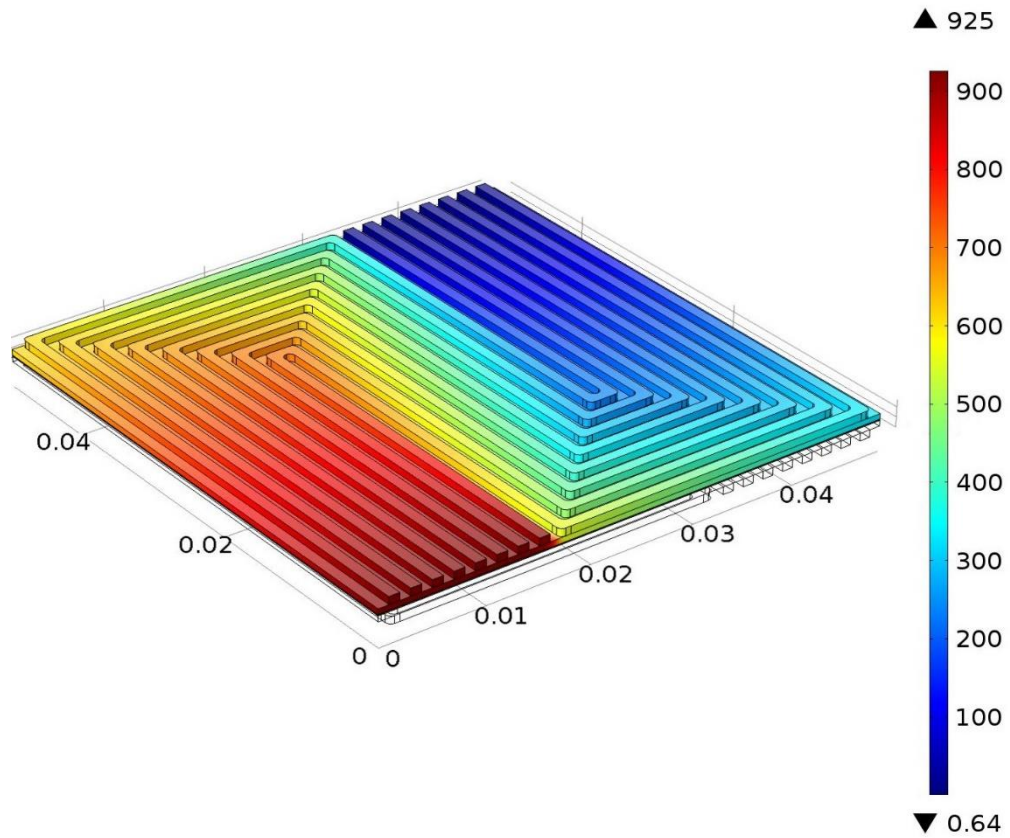
Figure 5.19 Pressure profile along cathode flow channel at 0.6 V and 165 °C for serpentine flow channel geometry (Pa)

The concentration profile of oxygen along cathode flow channels are given in Figure 5.20. As it is seen, the concentration decreases along the cathode flow channels from 3.84 mol m^{-3} to 1.31 mol m^{-3}. Oxygen concentration decreases from flow channels to catalyst layer due to the diffusion of species through a porous media.
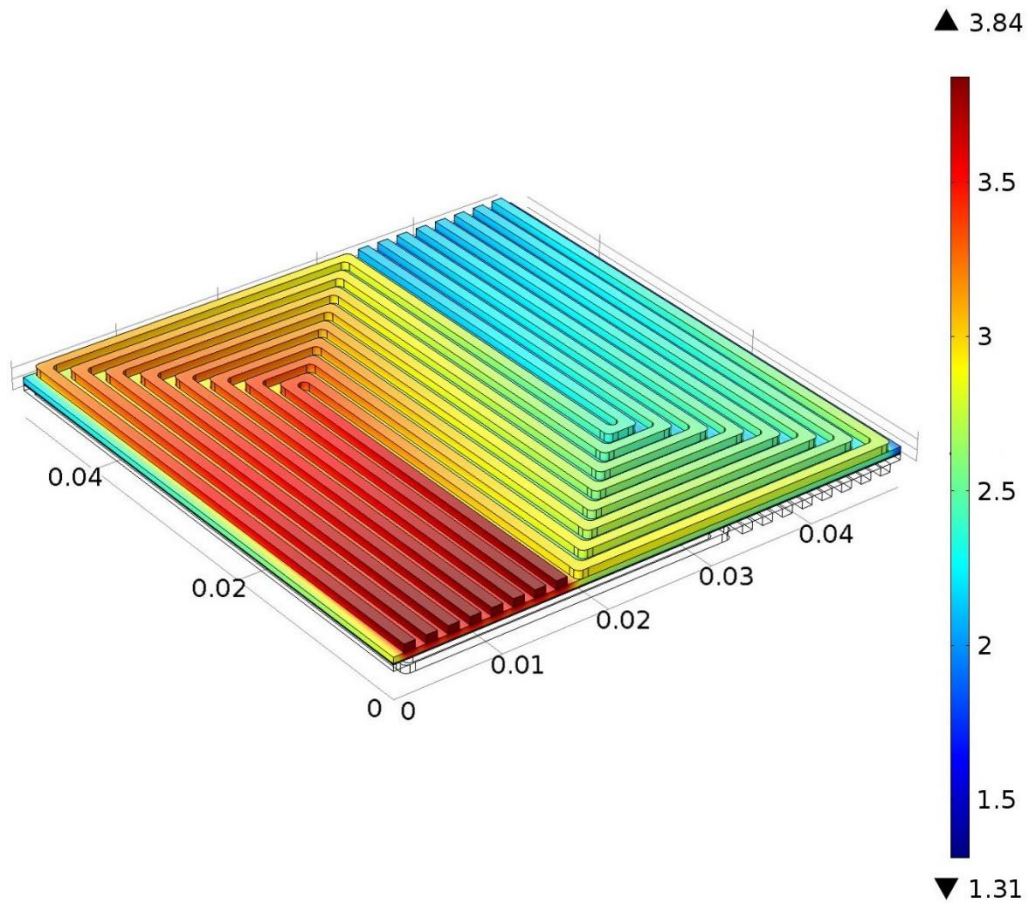
Figure 5.20 Concentration profile of oxygen at 165 °C and 0.6 V for serpentine flow channel geometry (mol m^{-3})

Figure 5.21 shows the membrane current density distribution at 165 °C and 0.6 V for serpentine flow channel geometry. The current density attains its maximum value at the inlet, and it continuously decreases along the flow channels. This is mainly because of decrease in the concentration of the reactants due to the reaction.
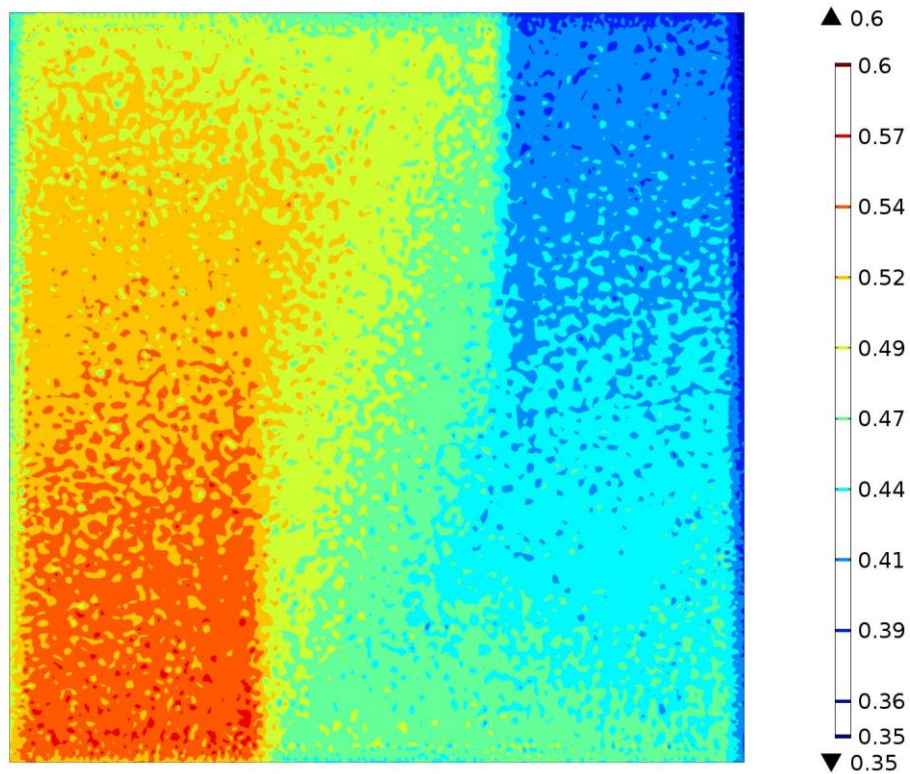
Figure 5.21 Membrane current density distribution at 165 $^{\circ}$C and 0.6 V for serpentine flow channel geometry (A cm^{-2})

Figure 5.22 illustrates the membrane current density distribution obtained at the operation temperature of 165 $^{\circ}$C for serpentine flow channel geometry at different operation voltages. There is a uniform current density distribution at 0.8 V with lower current density values compared to the 0.6 V. On the other hand, non-uniformities is observed in the current density distribution at 0.4 V due to the consumption of the reactants. The current density at the inlet part is 1.9 A cm^{-2}, whereas, this value decreases down to 0.07 A cm^{-2} at the outlet. This difference is mainly because of the drastic decrease in the concentration of reactants. It is seen that the current density is higher under the flow channels when it is compared with the ribs. This is mainly because of the diffusion of components from flow channels through the GDL.
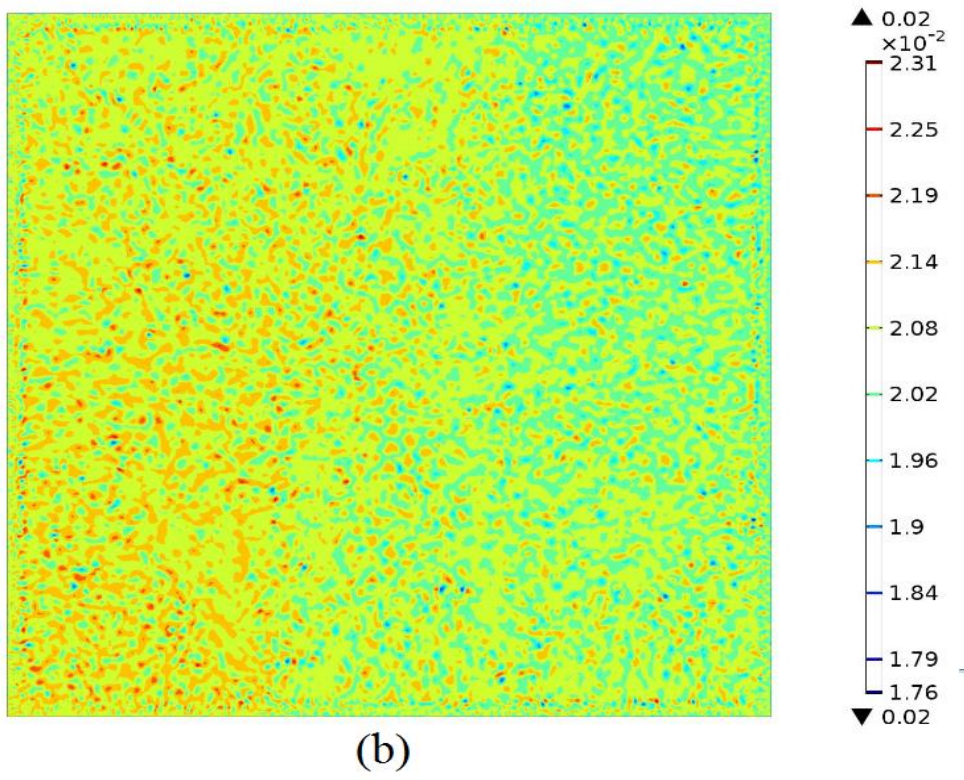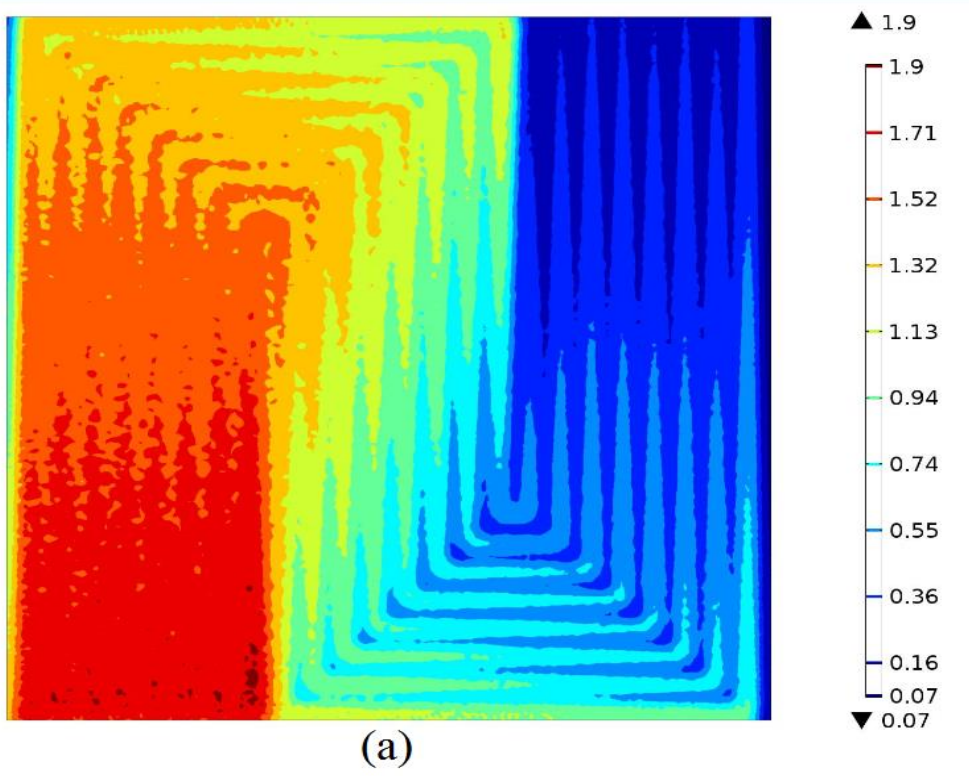
Figure 5.22 Membrane current density distribution at 165 °C for serpentine flow channel geometry (a) 0.4 V, (b) 0.8 V (A cm^{-2})

CHAPTER 6

6. THREE-DIMENSIONAL NON-ISOTHERMAL MODEL

In this chapter, a non-isothermal three-dimensional model is developed in order to obtain the temperature profile in HT-PEMFC. The temperature increase in a single cell is less than 1 $^{\circ}$C according to the model results. For the operation voltages of 0.6 V and 0.45 V, the average current density values are determined as 0.224 A cm-2 and 0.313 A cm-2, respectively. Figure 6.1 shows the temperature difference in single cell when the operation voltage is taken as 0.6 V. Figure 6.2 shows the temperature difference in single cell when the operation voltage is taken as 0.45 V. It is seen than at the operation voltage of 0.6 V the maximum temperature difference is 0.18 $^{\circ}$C, whereas this value increases to 0.31 $^{\circ}$C at 0.45 V. In their study, Samsun et al. [34] developed a model for a 5 kW fuel cell system working with reformate gas. Their simulation results reveals that the effluent temperature of both anode and cathode compartments attain 160 $^{\circ}$C, when the inlet temperatures of anode and cathode reactants are taken as 151 and 160 $^{\circ}$C, respectively. In addition, in their mathematical model having an active area of 200 cm^2 Kvesic et al. [46] found that the temperature difference does not exceed 10 $^{\circ}$C. For the current density of 0.3 A cm^{-2}, the temperature difference is found to be approximately 2 $^{\circ}$C, whereas this value increases to 5 $^{\circ}$C for 0.6 A cm^{-2}. Luke et al. [32] found the temperature gradient to be approximately 3 $^{\circ}$C at 0.4 A cm^{-2} for a 200 cm^2 HT-PEMFC modeled with cooling. The temperature difference decreases with increasing amount of coolant. Taking into account the active area; thus the evolved heat within the system, the results agree reasonably well.
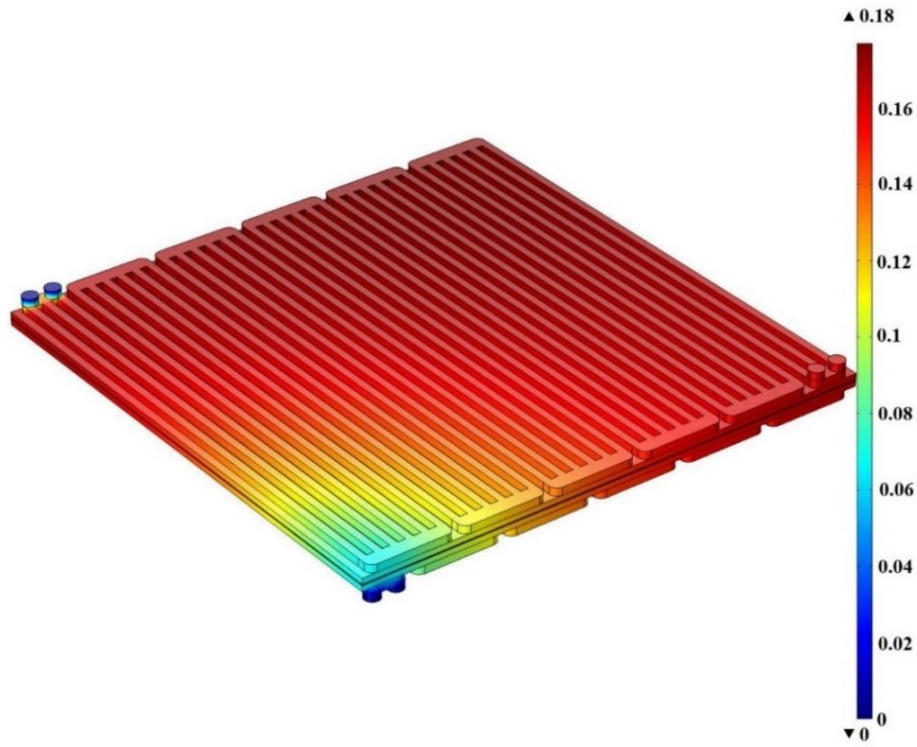
Figure 6.1 Temperature difference in a single cell, inlet reactant temperature is at
165 °C for V=0.60 V (K)
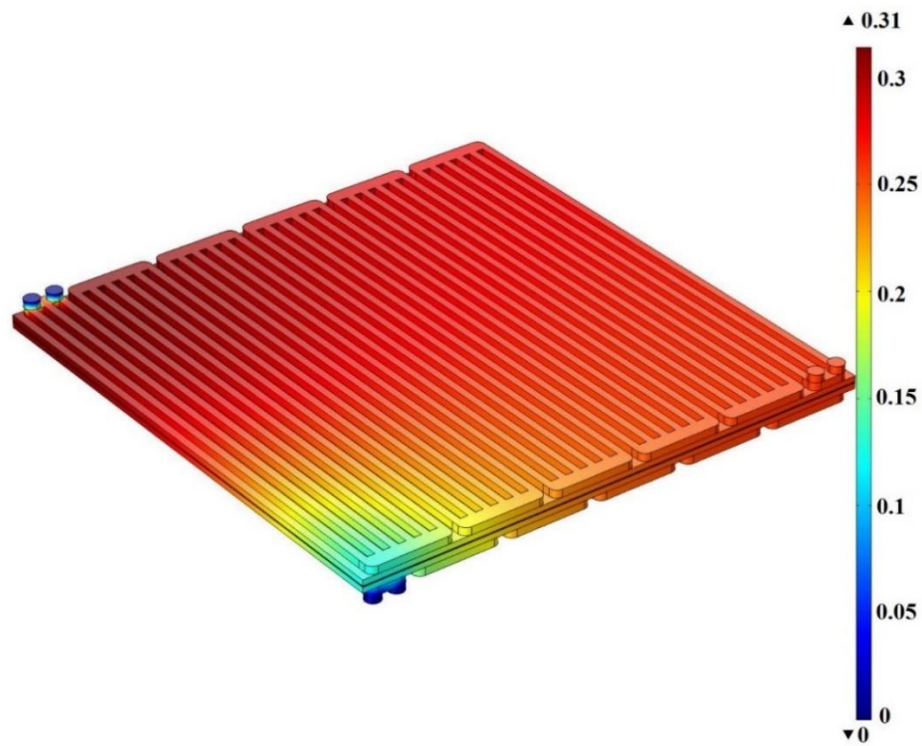
Figure 6.2 Temperature difference in a single cell, inlet reactant temperature is at
165 °C for V=0.45 V (K)

Figure 6.3 reveals the model results as temperature isocontours at 0.6 V and 0.45 V. The temperature attains its maximum value at the outlets, whereas it is 165 ^{o}C at the channel inlets. As it is expected, temperature gradient is larger at 0.45 V, since the current density increases with decreasing operation voltage. Increase in the current raises value of the generation term in the conservation of energy. When the anode and cathode inlets are compared, cathode inlet and its surrounding has higher temperature gradient, since the cathode compartment dominates the reaction.
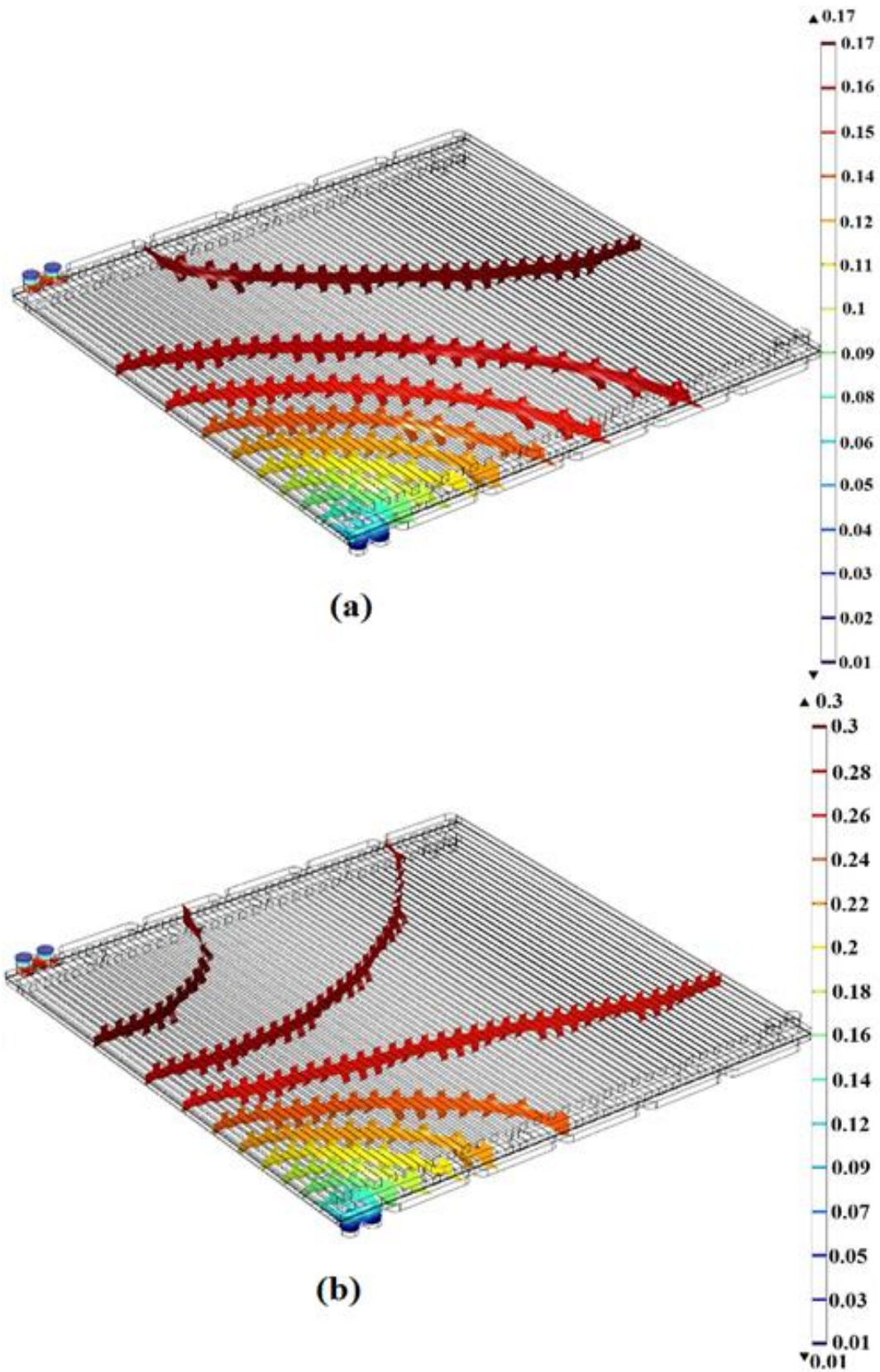
Figure 6.3 Temperature isocontours on the cell with inlet reactant temperature 165 °C, at different operation voltages (a) 0.6 V, (b) 0.45 V (K)

Figure 6.4 shows the pressure profile along cathode flow channels at 0.6 V with inlet reactant temperature of 165 °C. The pressure drop in isothermal model is approximately 6400 Pa; on the other hand, it increases to 6500 Pa in the non-isothermal model.
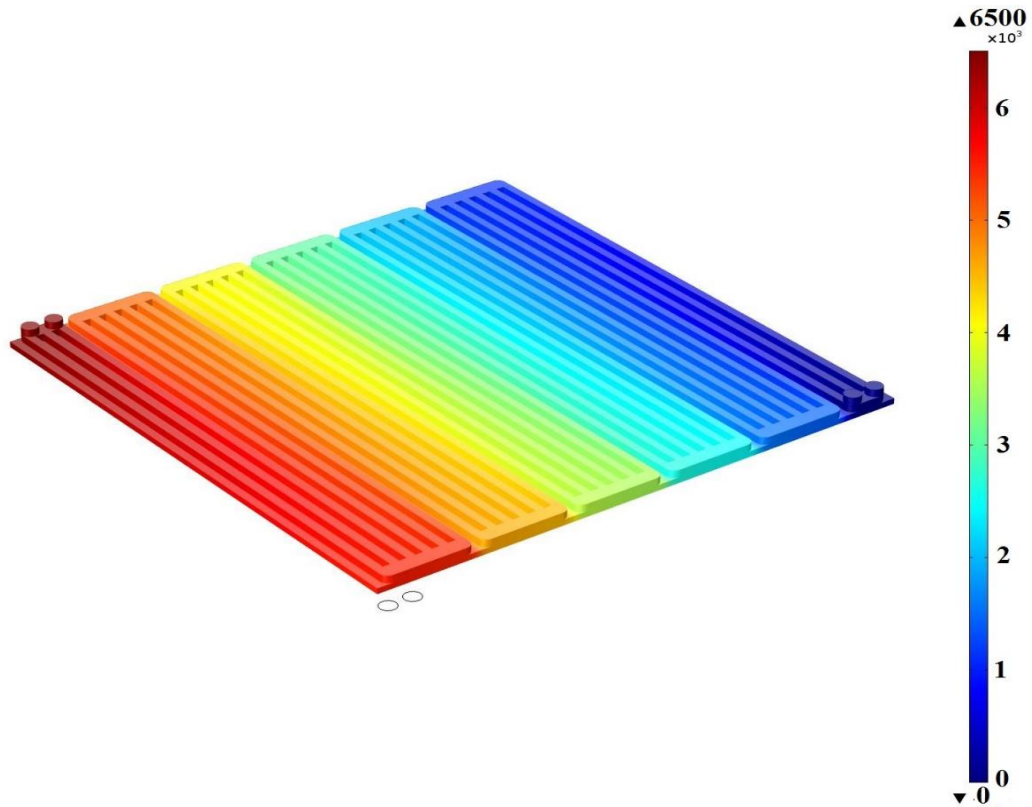
Figure 6.4 Pressure drop along the cathode flow channels with inlet reactant temperature of 165 °C and 0.6 V (Pa)

Figure 6.5 reveals the membrane current density distribution at 0.6 V with the inlet reactant temperature of 165 °C. Same trend as the isothermal model is observed in the non-isothermal model, which is current density is maximum around the inlet manifold of the cathode compartment. However, in the non-isothermal case the current density distribution is more uniform when it is compared with the isothermal model results given in Figure 5.15.
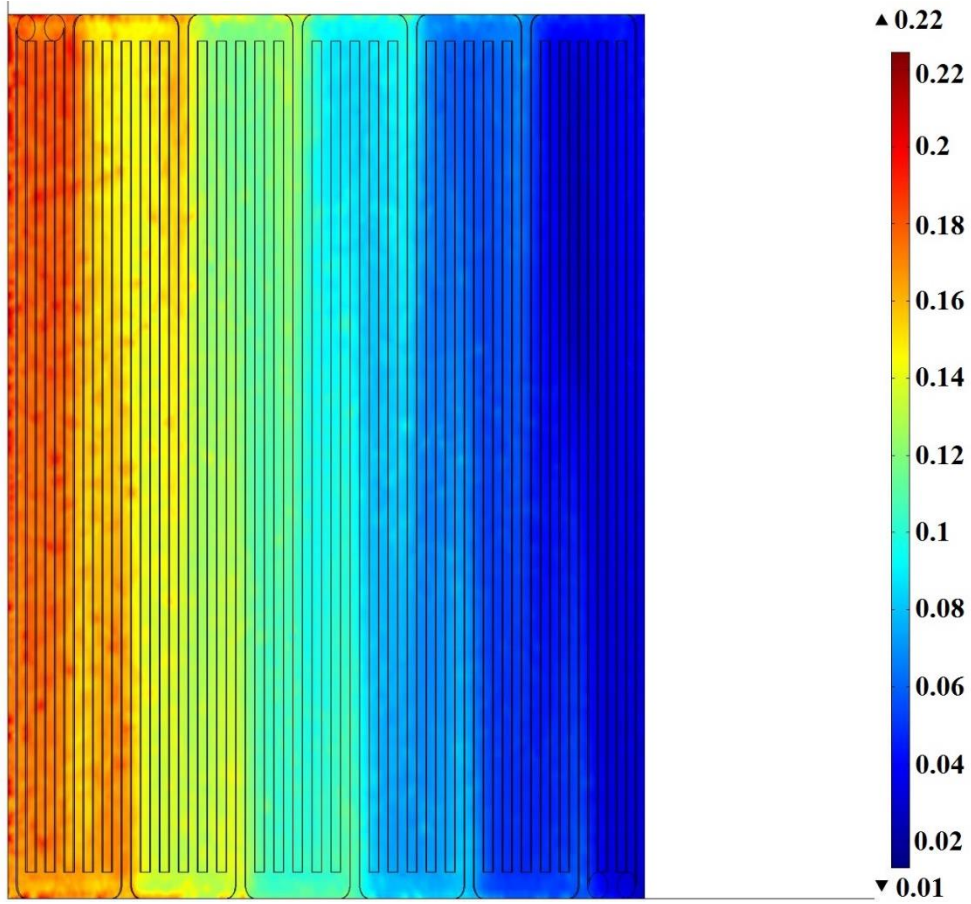
Figure 6.5 Membrane current density distribution at 0.6 V with inlet reactant temperature of 165 $^{\circ}$C (A cm^{-2})

CHAPTER 7

7. CONCLUSION AND RECOMMENDATIONS

In the scope of this study, three-dimensional mathematical models of HT-PEMFC are developed both for isothermal and non-isothermal operations. Modeling is an important tool especially in the design of a system, since it elaborates the system behavior in shorter time period compared to the experiments. Moreover, low cost and future predictability are the other advantages of modeling. With an appropriate model, one can easily determine the response of the system to the possible variations in the operation conditions.

The proton conductivities of the PBI membrane is taken from Danish Power Systems to investigate the effect of operation temperature in the temperature range of 100-180 ^{o}C. It is concluded that higher operation temperature enhances the fuel cell performance because of faster reaction kinetics and higher membrane proton conductivity. The effect of temperature is more pronounced between 100-120 ^{o}C when it is compared with 160-180 ^{o}C. Influence of the flow channel geometry on the HT-PEMFC performance is also investigated. It is seen that power density of the serpentine flow channel geometry is higher than the triple mixed serpentine model. The difference between the performances is more pronounced at high current densities. Membrane current density distribution is obtained for 0.4, 0.6 and 0.8 V at 165 ^{o}C. It is seen that the current density is non-uniform at lower operation voltages because of higher reactant consumption. As the consumption increases, the concentration of the reactants decreases, which affect the current density obtained by using Butler-Volmer equation. On the other hand, the current density is almost uniform at 0.8 V, since the amount of reacted gases does not change significantly. In addition, influence of the operation pressure is also studied. Higher operation pressure enhances the performance of HT-PEMFC. The pressure drop in the cathode

flow channels obtained at 140 and 165 °C is found to be 6020 Pa and 6397 Pa, respectively. Higher operation temperature causes higher pressure drop due to the increased velocity of gases and higher viscosities.

A non-isothermal three-dimensional model is developed for triple mixed serpentine flow channel geometry. The inlet temperature of anode and cathode reactants is taken as 165 °C. The models are simulated at two operation voltages 0.6 V and 0.45 V in order to observe the effect of voltage on the temperature profile along a single cell. Higher temperature gradient is observed at the operation voltage of 0.45 V, since the current density increases with decreasing operation voltage. The current density is directly related to the generation term within the conservation of energy. Increasing current density yields in higher generation. However, the difference between the maximum temperature and the inlet is 0.18 °C and 0.31 °C at 0.6 V and 0.45 V, respectively. Since the temperature does not change significantly, isothermal assumption can be used in the modeling of single HT-PEMFC.

In future studies, modeling of multiple cells with cooling channels should be developed in order to design the appropriate cooling strategy such as flow channel geometry of cooling plates, influence of co-flow and counter-flow of coolant. Moreover, it would be possible to determine whether the temperature is uniform in each cell or not by a short stack model. Moreover, acid leaching is not taken into consideration in this study. The model could be improved with a relation between acid leaching and proton conductivity.

REFERENCES

[1]   Günümüzde Kullanılan Alternatif Enerji Kaynakları Ve Kullanım Alanları n.d. http://www.enerji.gov.tr/tr-TR/Sayfalar/Temiz-Enerji (accessed May 31, 2016).

[2]   Barbir F. Pem Fuel Cells Theory and Practice. Burlington: Elsevier Academic Press; 2005. doi:10.1016/B978-0-12-387710-9.01001-8.

[3]   Pukrushpan JT, Stefanopoulou AG, Huei P. Control of Fuel Cell Power Systems. 1st ed. London: Springer; 2004.

[4]   Steele BC, Heinzel A. Materials for fuel-cell technologies. Nature 2001;414:345–52. doi:10.1038/35104620.

[5]   Revankar S, Majumdar P. FUEL CELLS Principles, Design, and Analysis. CRC Press; 2014.

[6]   Zhang J, Xie Z, Zhang J, Tang Y, Song C, Navessin T, et al. High temperature PEM fuel cells. J Power Sources 2006;160:872–91. doi:10.1016/j.jpowsour.2006.05.034.

[7]   Ergun D, Devrim Y, Bac N, Eroglu I. Phosphoric acid doped polybenzimidazole membrane for high temperature PEM fuel cell. J Appl Polym Sci 2012;124:E267–77. doi:10.1002/app.36507.

[8]   Hjuler HA, Steenberg T, Terkelsen C, Holst T, Garcia HR, Cooper K. Performance of the HT-PEM Membrane Electrode Assembly. 222nd Electrochem. Soc. Meet., Honolulu: 2012.

[9]   Bouchet R, Siebert E. Proton conduction in acid doped polybenzimidazole. Solid State Ionics 1999;118:287–99. doi:10.1016/S0167-2738(98)00466-4.

[10]   Pu H, Meyer WH, Wegner G. Proton transport in polybenzimidazole blended with H3PO4 or H2SO4. J Polym Sci Part B Polym Phys 2002;40:663–9. doi:10.1002/polb.10132.

[11]   Fontanella J., Wintersgill M., Wainright J., Savinell R., Litt M. High pressure electrical conductivity studies of acid doped polybenzimidazole. Electrochim Acta 1998;43:1289–94. doi:10.1016/S0013-4686(97)10032-9.

[12]   Glipa X, Bonnet B, Mula B, Jones DJ, Rozière J. Investigation of the conduction properties of phosphoric and sulfuric acid doped polybenzimidazole. J Mater Chem 1999;9:3045–9. doi:10.1039/a906060j.

[13]   Kawahara M, Morita J, Rikukawa M, Sanui K, Ogata N. Synthesis and proton conductivity of thermally stable polymer electrolyte: Poly(benzimidazole) complexes with strong acid molecules. Electrochim Acta 2000;45:1395–8. doi:10.1016/S0013-4686(99)00349-7.

[14]   He R, Li Q, Xiao G, Bjerrum NJ. Proton conductivity of phosphoric acid doped polybenzimidazole and its composites with inorganic proton conductors. J Memb Sci 2003;226:169–84. doi:10.1016/j.memsci.2003.09.002.

[15]   Ma Y-L, Wainright JS, Litt MH, Savinell RF. Conductivity of PBI Membranes for High-Temperature Polymer Electrolyte Fuel Cells. J Electrochem Soc 2004;151:A8. doi:10.1149/1.1630037.

[16]   Hjuler H a., Steenberg T, Terkelsen C, Holst T, Garcia HR, Cooper K. Performance of the HT-PEM Membrane Electrode Assembly. ECS Trans 2013;50:1127–35. doi:10.1149/05002.1127ecst.

[17]   Zeis R. Materials and characterization techniques for high-temperature polymer electrolyte membrane fuel cells. Beilstein J Nanotechnol 2015;6:68–83. doi:10.3762/bjnano.6.8.

[18]   Korsgaard AR, Refshauge R, Nielsen MP, Bang M, K?? SK. Experimental characterization and modeling of commercial polybenzimidazole-based MEA performance. J Power Sources 2006;162:239–45. doi:10.1016/j.jpowsour.2006.06.099.

[19]   Hu J, Zhang H, Hu J, Zhai Y, Yi B. Two dimensional modeling study of PBI/H3PO4 high temperature PEMFCs based on electrochemical methods. J Power Sources 2006;160:1026–34. doi:10.1016/j.jpowsour.2006.02.026.

[20]   Zhang J, Tang Y, Song C, Zhang J. Polybenzimidazole-membrane-based PEM fuel cell in the temperature range of 120-200 °C. J Power Sources 2007;172:163–71. doi:10.1016/j.jpowsour.2007.07.047.

[21]   Scott K, Pilditch S, Mamlouk M. Modelling and experimental validation of a high temperature polymer electrolyte fuel cell. J Appl Electrochem 2007;37:1245–59. doi:10.1007/s10800-007-9414-1.

[22]   Ubong EU, Shi Z, Wang X. Three-Dimensional Modeling and Experimental Study of a High Temperature PBI-Based PEM Fuel Cell. J Electrochem Soc 2009;156:B1276. doi:10.1149/1.3203309.

[23]   Wannek C, Lehnert W, Mergel J. Membrane electrode assemblies for high-temperature polymer electrolyte fuel cells based on poly(2,5-benzimidazole) membranes with phosphoric acid impregnation via the catalyst layers. J Power Sources 2009;192:258–66. doi:10.1016/j.jpowsour.2009.03.051.

[24]   Wannek C, Konradi I, Mergel J, Lehnert W. Redistribution of phosphoric acid in membrane electrode assemblies for high-temperature polymer electrolyte fuel cells. Int J Hydrogen Energy 2009;34:9479–85. doi:10.1016/j.ijhydene.2009.09.076.

[25]   Parrondo J, Venkateswara Rao C, Ghatty SL, Rambabu B. Electrochemical Performance Measurements of PBI-Based High-Temperature PEMFCs. Int J Electrochem 2011;2011:1–8. doi:10.4061/2011/261065.

[26]   Su a., Ferng YM, Hou J, Yu TL. Experimental and numerical investigations of the effects of PBI loading and operating temperature on a high-temperature PEMFC. Int J Hydrogen Energy 2012;37:7710–8. doi:10.1016/j.ijhydene.2012.02.004.

[27]   Steenberg T, Hjuler HA, Terkelsen C, Sánchez MTR, Cleemann LN, Krebs FC. Roll-to-roll coated PBI membranes for high temperature PEM fuel cells. Energy Environ Sci 2012;5:6076. doi:10.1039/c2ee02936g.

[28]   Bezmalinović D, Strahl S, Roda V, Husar A. Water transport study in a high temperature proton exchange membrane fuel cell stack. Int J Hydrogen Energy 2014;39:10627–40. doi:10.1016/j.ijhydene.2014.04.186.

[29]   Sun H, Xie C, Chen H, Almheiri S. A numerical study on the effects of temperature and mass transfer in high temperature PEM fuel cells with ab-PBI membrane q. Appl Energy 2015;160:937–44. doi:10.1016/j.apenergy.2015.02.053.

[30]   Devrim Y, Devrim H, Eroglu I. Polybenzimidazole/SiO2 hybrid membranes for high temperature proton exchange membrane fuel cells. Int J Hydrogen Energy 2016;41:10044–52. doi:10.1016/j.ijhydene.2016.02.043.

[31]   Li Q, Jensen JO, Savinell RF, Bjerrum NJ. High temperature proton exchange membranes based on polybenzimidazoles for fuel cells. Prog Polym Sci 2009;34:449–77. doi:10.1016/j.progpolymsci.2008.12.003.

[32]   Lüke L, Janßen H, Kvesić M, Lehnert W, Stolten D. Performance analysis of HT-PEFC stacks. Int J Hydrogen Energy 2012;37:9171–81. doi:10.1016/j.ijhydene.2012.02.190.

[33]   Janßen H, Supra J, Lüke L, Lehnert W, Stolten D. Development of HT-PEFC stacks in the kW range. Int J Hydrogen Energy 2013;38:4705–13. doi:10.1016/j.ijhydene.2013.01.127.

[34]   Samsun RC, Pasel J, Janßen H, Lehnert W, Peters R, Stolten D. Design and test of a 5kWe high-temperature polymer electrolyte fuel cell system operated with diesel and kerosene. Appl Energy 2014;114:238–49. doi:10.1016/j.apenergy.2013.09.054.

[35]   Cheddie D, Munroe N. Mathematical model of a PEMFC using a PBI membrane. Energy Convers Manag 2006;47:1490–504. doi:10.1016/j.enconman.2005.08.002.

[36]   Cheddie D, Munroe N. Parametric model of an intermediate temperature PEMFC. J Power Sources 2006;156:414–23. doi:10.1016/j.jpowsour.2005.06.010.

[37]   Peng J, Lee SJ. Numerical simulation of proton exchange membrane fuel cells at high operating temperature. J Power Sources 2006;162:1182–91. doi:10.1016/j.jpowsour.2006.08.001.

[38]   Lobato J, Cañizares P, Rodrigo MA, Pinar FJ, Mena E, Úbeda D. Three-dimensional model of a 50 cm2 high temperature PEM fuel cell. Study of the flow channel geometry influence. Int J Hydrogen Energy 2010;35:5510–20. doi:http://dx.doi.org/10.1016/j.ijhydene.2010.02.089.

[39]   Kvesić M, Reimer U, Froning D, Lüke L, Lehnert W, Stolten D. 3D modeling of a 200 cm2 HT-PEFC short stack. Int J Hydrogen Energy 2012;37:2430–9. doi:10.1016/j.ijhydene.2011.10.055.

[40]   Krastev VK, Falcucci G, Jannelli E, Minutillo M, Cozzolino R. 3D CFD modeling and experimental characterization of HT PEM fuel cells at different anode gas compositions. Int J Hydrogen Energy 2014;39:21663–72. doi:10.1016/j.ijhydene.2014.09.015.

[41]   Sun H, Xie C, Chen H, Almheiri S. A numerical study on the effects of temperature and mass transfer in high temperature PEM fuel cells with ab-PBI membrane. Appl Energy 2015. doi:10.1016/j.apenergy.2015.02.053.

[42]   Cheddie DF, Munroe NDH. Three dimensional modeling of high temperature PEM fuel cells. J Power Sources 2006;160:215–23. doi:10.1016/j.jpowsour.2006.01.035.

[43]   Cheddie DF, Munroe NDH. A two-phase model of an intermediate temperature PEM fuel cell. Int J Hydrogen Energy 2007;32:832–41. doi:10.1016/j.ijhydene.2006.10.061.

[44]   Siegel C, Bandlamudi G, Heinzel A. Systematic characterization of a PBI/H3PO4 sol-gel membrane - Modeling and simulation. J Power Sources 2011;196:2735–49. doi:10.1016/j.jpowsour.2010.11.028.

[45]   Harikishan Reddy E, Jayanti S. Thermal management strategies for a 1 kWe stack of a high temperature proton exchange membrane fuel cell. Appl Therm Eng 2012;48:465–75. doi:10.1016/j.applthermaleng.2012.04.041.

[46]   Kvesić M, Reimer U, Froning D, Lüke L, Lehnert W, Stolten D. 3D modeling of an HT-PEFC stack using reformate gas. Int J Hydrogen Energy 2012;37:12438–50. doi:10.1016/j.ijhydene.2012.05.113.

[47]   Chippar P, Ju H. Numerical modeling and investigation of gas crossover effects in high temperature proton exchange membrane (PEM) fuel cells. Int J Hydrogen Energy 2013;38:7704–14. doi:10.1016/j.ijhydene.2012.07.123.

[48]   Lang S, Kazdal TJ, Kühl F, Hampe MJ. Experimental investigation and numerical simulation of the electrolyte loss in a HT-PEM fuel cell. Int J Hydrogen Energy 2015;40:1163–72. doi:10.1016/j.ijhydene.2014.11.041.

[49]   Kazdal TJ, Lang S, Kühl F, Hampe MJ. Modelling of the vapour-liquid equilibrium of water and the in situ concentration of H3PO4 in a high temperature proton exchange membrane fuel cell. J Power Sources 2014;249:446–56. doi:10.1016/j.jpowsour.2013.10.098.

[50]   Elden G, Çelik M, Genç G, Yapıcı H. The effects of temperature on transport phenomena in phosphoric acid doped polybenzimidazole polymer electrolyte membrane fuel cell. Energy 2016;103:772–83. doi:10.1016/j.energy.2016.02.137.

[51]   Sezgin B, Caglayan DG, Devrim Y, Steenberg T, Eroglu I. Modeling and sensitivity analysis of high temperature PEM fuel cells by using Comsol Multiphysics. Int J Hydrogen Energy 2016;41:10001–9. doi:10.1016/j.ijhydene.2016.03.142.

[52]   Caglayan DG, Sezgin B, Devrim Y, Eroglu I. Three-dimensional modeling of a high temperature polymer electrolyte membrane fuel cell at different operation temperatures. Int J Hydrogen Energy 2016;41:10060–70. doi:10.1016/j.ijhydene.2016.03.049.

[53]   Yang X, Li W. A novel theoretical approach to the temperature–viscosity relation for fluidic fuels. Fuel 2015;153:85–9. doi:10.1016/j.fuel.2015.02.115.

[54]   Welty JR, Wicks CE, Wilson RE, Rorrer GL. Fundamentals of Momentum, Heat, and Mass Transfer. 5th ed. Danvers: John Wiley & Sons; 2008. doi:10.1016/0017-9310(70)90063-3.

[55]   Wu H, Berg P, Li X. Non-isothermal transient modeling of water transport in PEM fuel cells. J Power Sources 2007;165:232–43. doi:10.1016/j.jpowsour.2006.11.061.

[56]   Ju H, Meng H, Wang CY. A single-phase, non-isothermal model for PEM fuel cells. Int J Heat Mass Transf 2005;48:1303–15. doi:10.1016/j.ijheatmasstransfer.2004.10.004.

[57]   Li Q, Jensen JO, Savinell RF, Bjerrum NJ. High temperature proton exchange membranes based on polybenzimidazoles for fuel cells. Prog Polym Sci 2009;34:449–77. doi:10.1016/j.progpolymsci.2008.12.003.

[58]   Sousa T, Mamlouk M, Scott K. A non-isothermal model of a laboratory intermediate temperature fuel cell using PBI doped phosphoric acid membranes. Fuel Cells 2010;10:993–1012. doi:10.1002/fuce.200900178.

[59]   Li Q, He R, Jensen J, Bjerrum N. Approaches and recent development of polymer electrolyte membranes for fuel cells operating above 100 C. Chem Mater 2003:4896–915. doi:10.1021/cm0310519.

[60]   Qi Z. Effect of CO in the anode fuel on the performance of PEM fuel cell cathode. J Power Sources 2002;111:239–47. doi:10.1016/S0378-7753(02)00300-2.

[61]   Kongstein OE, Berning T, Børresen B, Seland F, Tunold R. Polymer electrolyte fuel cells based on phosphoric acid doped polybenzimidazole (PBI) membranes. Energy 2007;32:418–22. doi:10.1016/j.energy.2006.07.009.

[62]   Xing B, Savadogo O. The effect of acid doping on the conductivity of polybenzimidazole (PBI). J New Mater Electrochem Syst 1999;2:95–101.

[63]   Najafi B, Haghighat Mamaghani A, Baricci A, Rinaldi F, Casalegno A. Mathematical modelling and parametric study on a 30 kWel high temperature PEM fuel cell based residential micro cogeneration plant. Int J Hydrogen Energy 2015;40:1569–83. doi:10.1016/j.ijhydene.2014.11.093.

[64]   Cheddie D, Munroe N. Review and comparison of approaches to proton exchange membrane fuel cell modeling. J Power Sources 2005;147:72–84. doi:10.1016/j.jpowsour.2005.01.003.

[65]   Hjuler HA, Steenberg T, Terkelsen C, Holst T, Garcia HR. Performance of the HT_PEM Membrane Electrode Assembly. 222nd Electrochem. Soc. Meet., Honolulu: 2012.

APPENDIX A

PHYSICS IN COMSOL MULTIPHYSICS FOR THE MODELS

The definitions used in Comsol Multiphysics are given Figure A.1. The domains drawn in geometry section are referred as specific components of the system by using "Definition" section in the Model Builder.
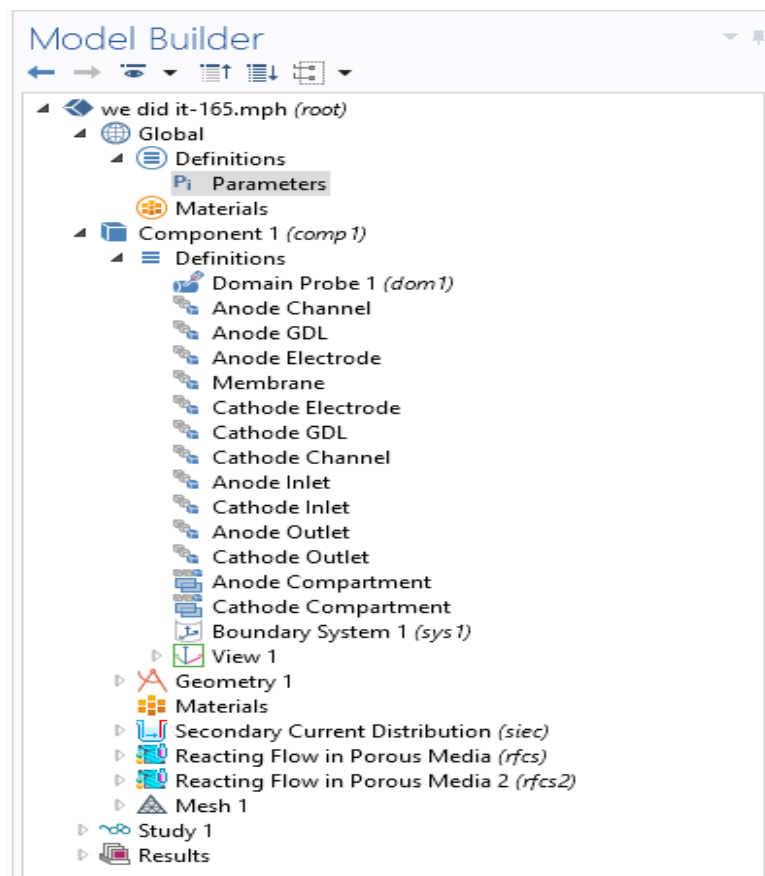
Figure A.1 Definitions used in Comsol Multiphysics

The items used in drawing of the model geometry are available in Figure A.2. MEA is drawn by using blocks; on the other hand, in the drawing of flow channel geometry extrude command is employed.
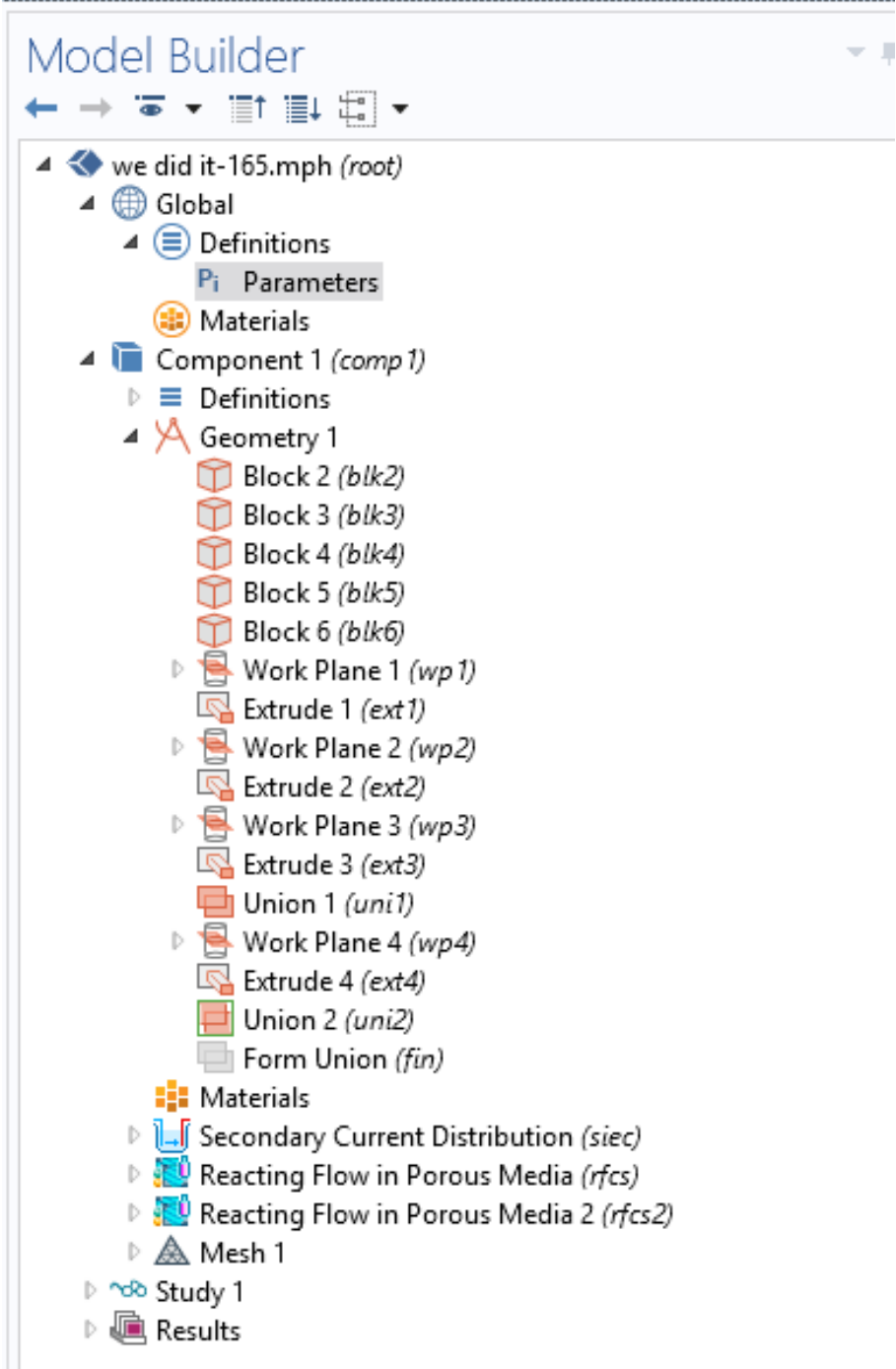
Figure A.2 Items used in geometry section

Secondary current distribution is the physics used in the determination of the charge transport. The boundary conditions used in secondary current distribution is available in the Figure A.3.
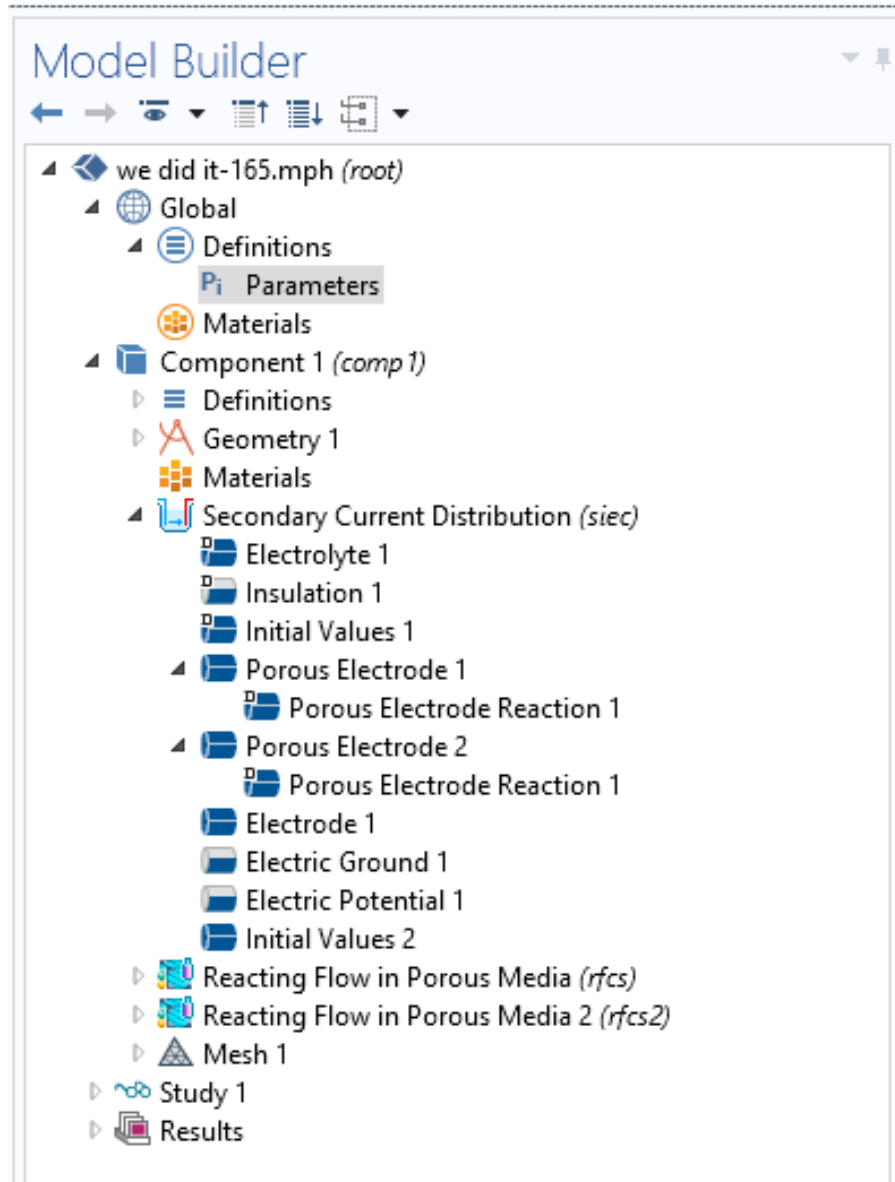
Figure A.3 Initial and boundary conditions employed in secondary current distribution

Reacting flow in porous media is the physics used in the modeling of mass and momentum transport. The boundary conditions used in reacting flow in porous media is illustrated in Figure A.4.
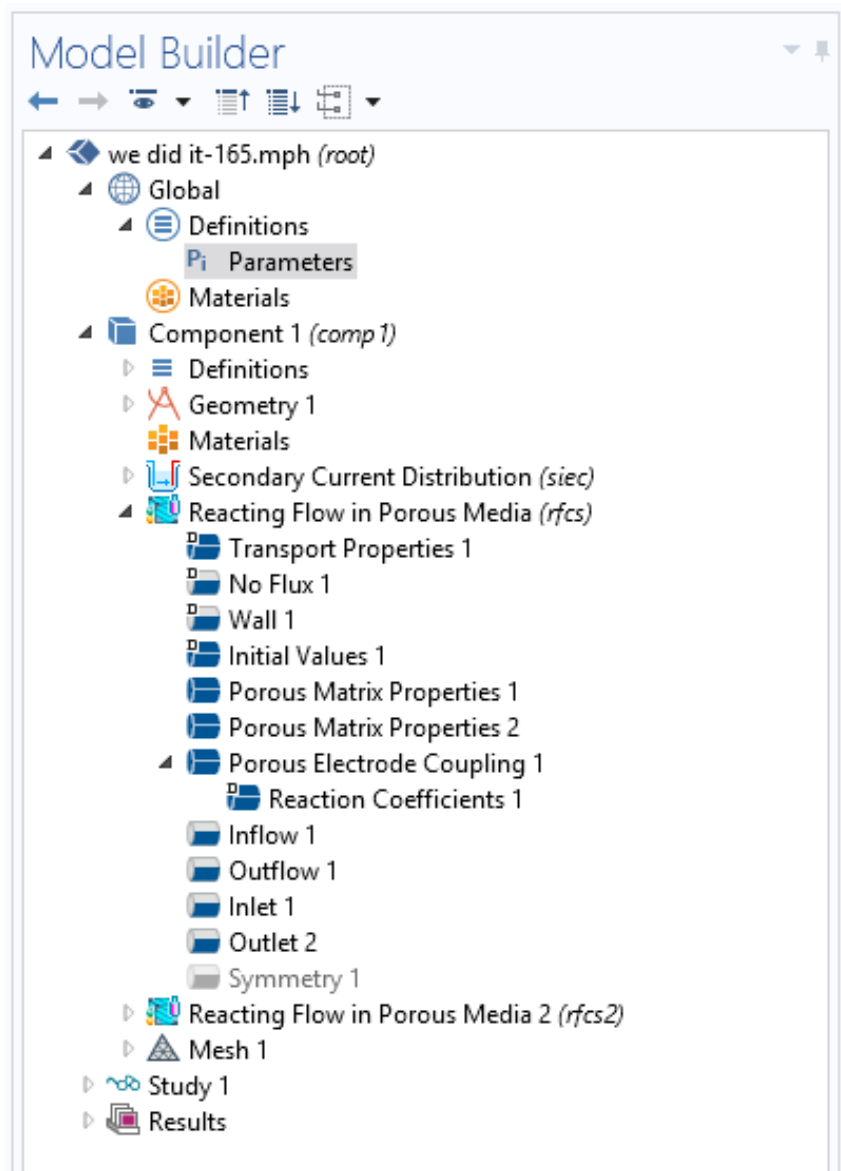
Figure A.4 Initial and boundary conditions employed in reacting flow in porous media

Study tool is used in the solution of governing equations. For steady-state problems, stationary solver is employed. The tabs in the study tool can be shown in Figure A.5. Direct solver utilizes LU decomposition method in the solution algoritm.
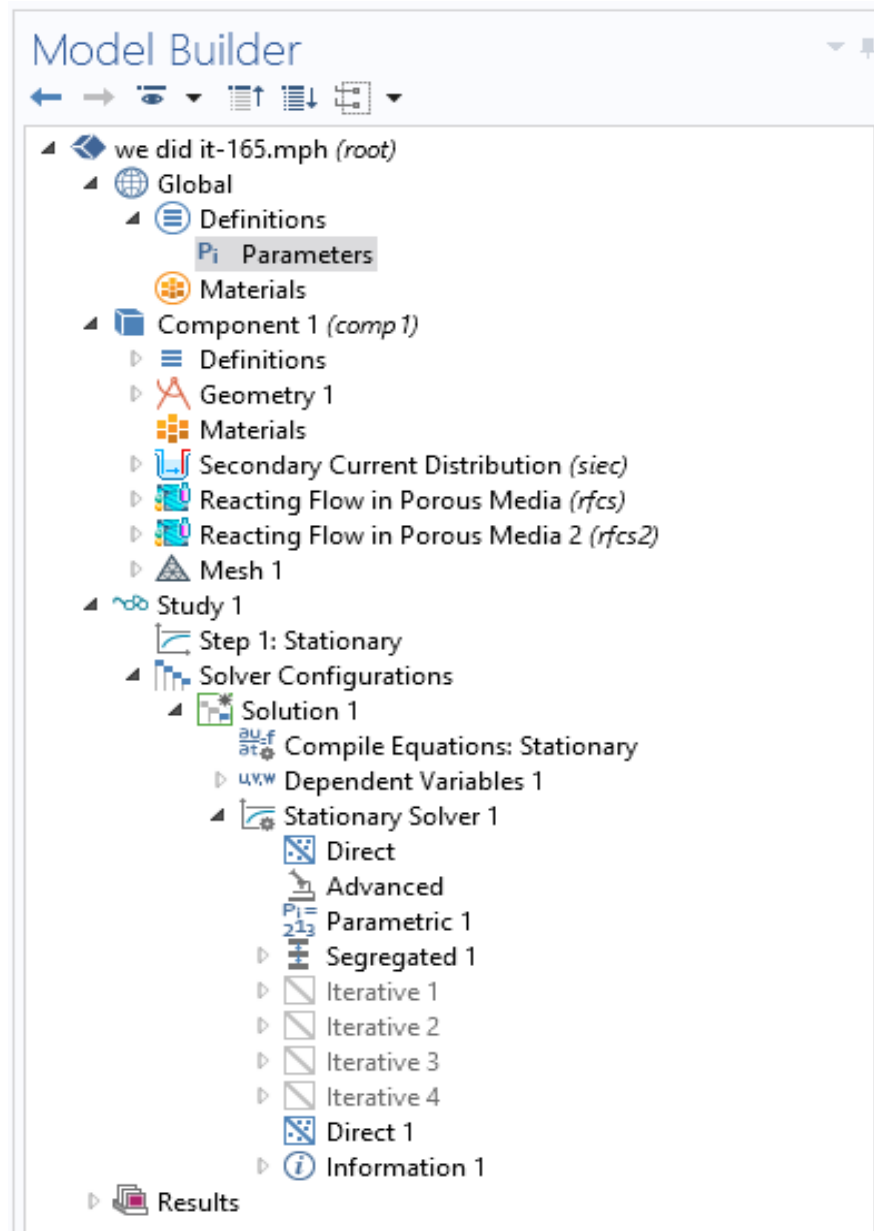
Figure A.5 Tabs used in study tool

Results tool is used to obtain 1D, 2D and 3D plots of parameters defined in the equations. In Figure A.6, results tool used in Comsol Multiphysics is shown.
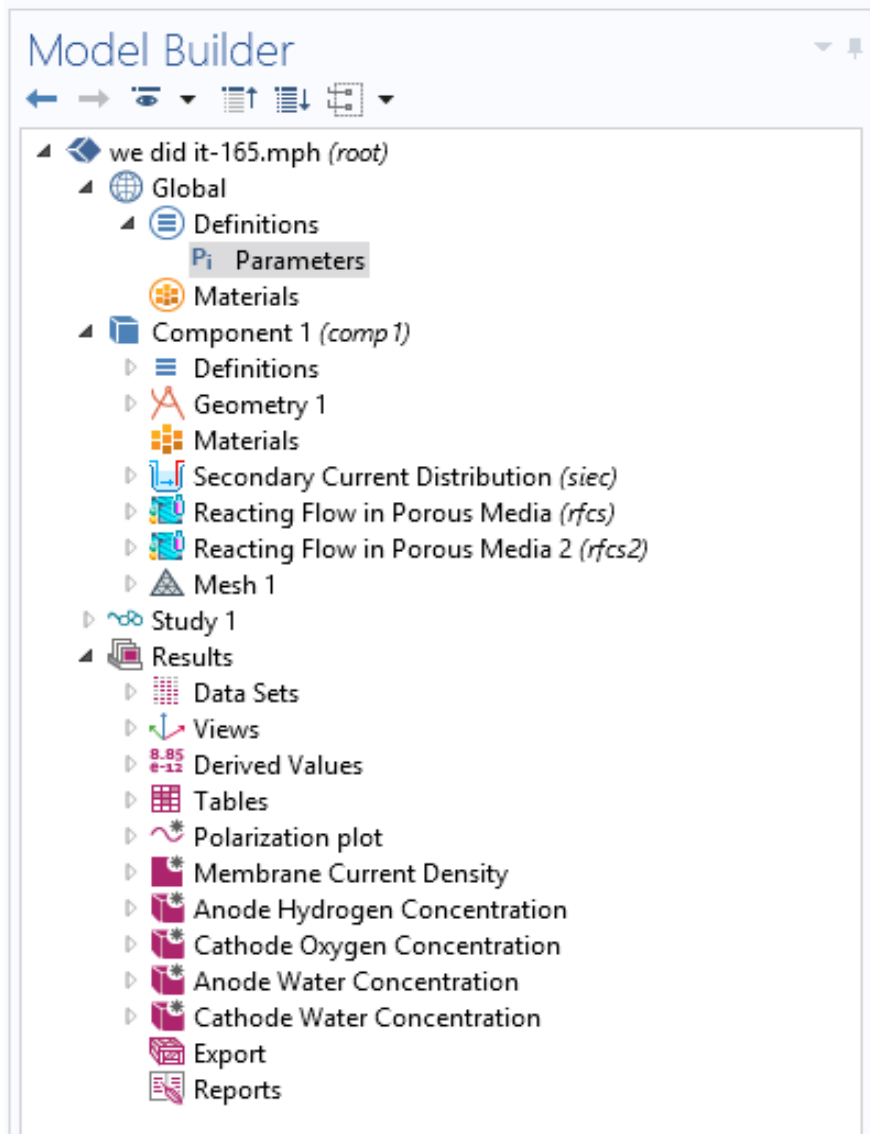
Figure A.6 Results tool in Comsol Multiphysics

Heat Transfer in Porous Media physics is added to the model in order to take into account the conservation of energy for the entire domain. The initial and boundary conditions in this physics are given in Figure A.7
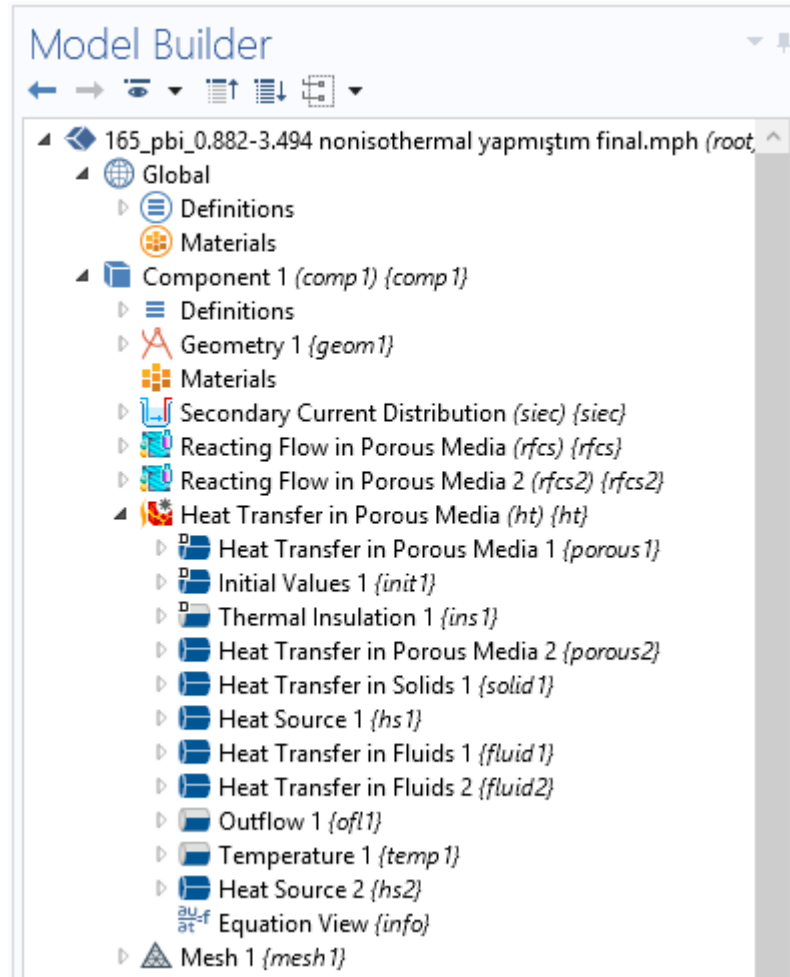
Figure A.7 Initial and boundary conditions in heat transfer in porous media

APPENDIX B

COMPUTER SPECIFICATIONS

Brand/Model Information	Dell XPS 8700

Processor Specifications	Processor Intel Processor Cache 8 MB Processor Speed 4.00 GHz Processor Model Intel Core i7-4790 Processor Type 4. Generation Intel Core i7
Operating System	Licensed Windows 8.1 64-Bit
Display Card	Display Card Memory 4GB Display Card Model nVidia GeForce GTX 745 Display Card Type External Display Card

Memory Properties	Memory Frequency
	1600Mhz
	Memory Capacity
	16GB
	Memory Type
	DDR3
	Memory Bank
	4 Slot
Disk Properties	Disk Speed
	7200 rpm
	Disk Capacity
	2TB
	Disk Type
	SATA
Extension Slot Properties	PCI
	Mini-PCIe : 2 Slot
	PCI Express x1
	PCIe x1: 2 slot
	PCI Express x16
	PCIe x16 (Graphics): 1 slot
Link Properties	Bluetooth
	Yes
	Display Output
	VGA, HDMI
	Ethernet
	10/100/1000
	Wireless Card
	Dell Wireless 1703
	Card Reader

Yes

Other Properties	Keyboard & Mouse
	Dell KM632 Wireless Mouse and Keyboard
	Optical Reader
	Yes
	Power Supply
	460W up to 85 Efficient

APPENDIX C

EXPERIMENTAL METHODS

Membrane Electrode Assembly Preparation

The electrodes having an active surface area of 25 cm2 were prepared by using the ultrasonic spraying machine, Sonotec Exactacoat. The catalytic ink is sprayed over the entire active area of the microporous layer of the GDL. Platinum loadings on anode/cathode were 1.5/1.5 mg/cm^2 for Pt/C. In the preparation of the MEA, commercial PBI membrane produced by Danish Power Systems, Dapozol®, was used. Acid doping of the membrane was achieved by immersing the membrane in 85% phosphoric acid for an hour at a temperature of 40 ^{o}C. Acid doping level of the membrane, which is defined as the number of moles of phosphoric acid per repeated unit of PBI, was 10. This value was sufficient to provide phosphoric acid from membrane to catalyst layer by diffusion. Hot-pressing is used in assembling of the electrodes and the membrane. The hot-press is performed at the temperature of 200 ^{o}C and pressure of 4 MPa for 3 minutes. The conductivity measurements were performed with four-probe conductivity cell under air with no humidification [51].

HT-PEMFC Performance Tests

The performance tests are performed by using a single cell with an active area of 25 cm^2. The bipolar plates are made of graphite material with serpentine flow channel geometry. The inlet flow rates of anode and cathode feeds were 0.14 and 0.55 slpm, respectively. This value corresponds to 1.5 and 2.5 stoichiometric ratios for anode and cathode, respectively. Attaining steady-state operation, current-voltage data is

taken starting from OCV. For each data point the load is changed. Figure C.1 shows the test station where performance tests are performed.

Figure C.1 A photograph of the test station used by Danish Power Systems

APPENDIX D

COMPUTATIONAL DOMAIN AND MESHING

The domain used in Comsol Multiphysics consist of gas flow channels, GDL for anode and cathode compartments and the electrolyte as shown in the previous chapters including model development. Meshing applied to the computational domains for triple mixed serpentine and serpentine flow channel geometries are different due to the dissimilarities in their geometry. The triple mixed serpentine model consists of 1283045 elements with minimum quality 1.272E-5 and with an average quality of 0.5953. The meshed computational domain for triple mixed serpentine is given in Figure D.1. There are 1281735 tetrahedral elements, 1310 pyramid elements, 398347 triangular elements, 41082 edge elements and 784 vertex elements within the system.
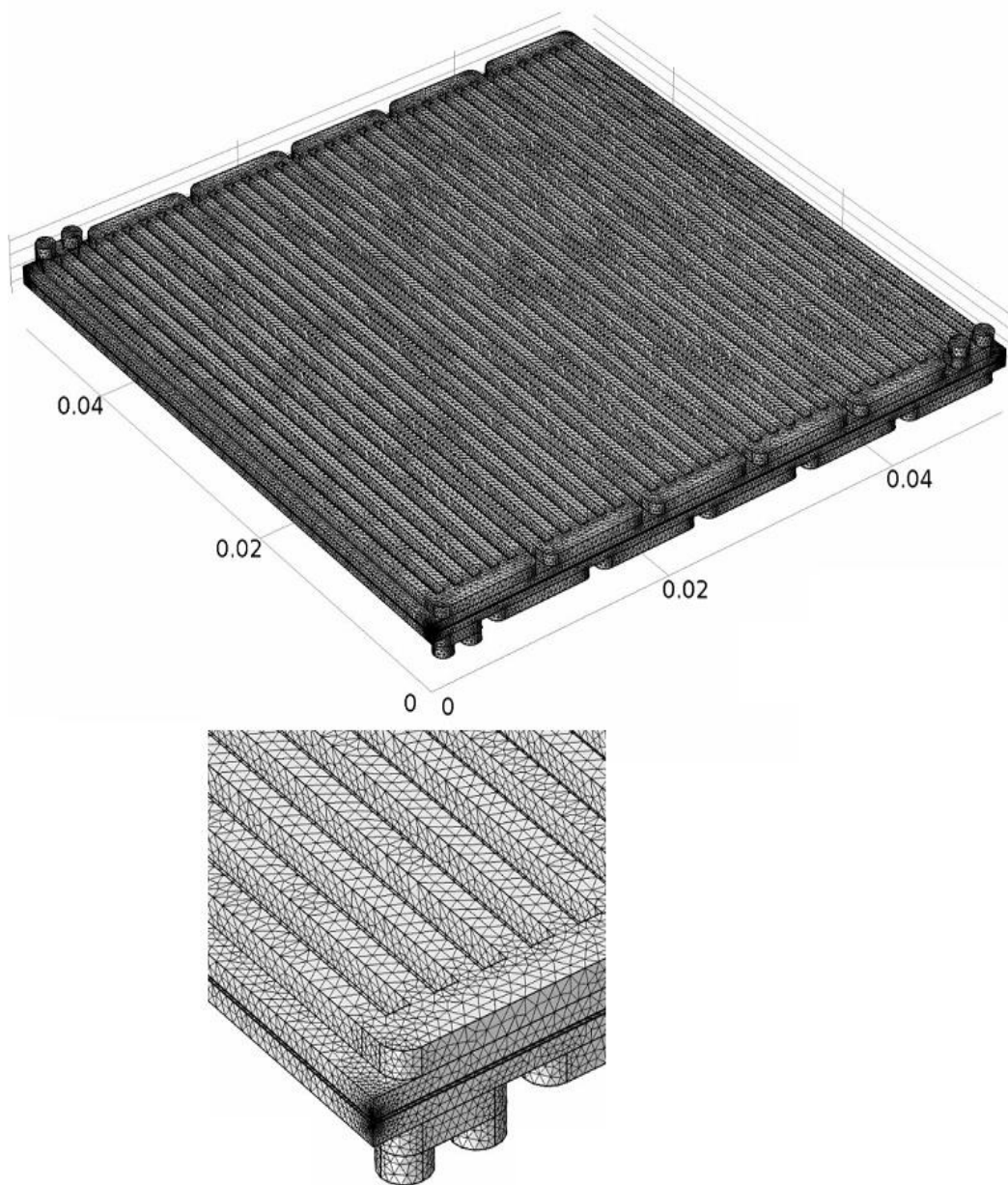
Figure D.1 Meshed computational domain for triple mixed serpentine model

The serpentine model consists of 1550773 elements with minimum quality 1.324E-5 and with an average quality of 0.606. The meshed computational domain for serpentine flow channel geometry is given in Figure D.2. There are 1549679 tetrahedral elements, 1094 pyramid elements, 447852 triangular elements, 38409 edge elements and 902 vertex elements within the system.
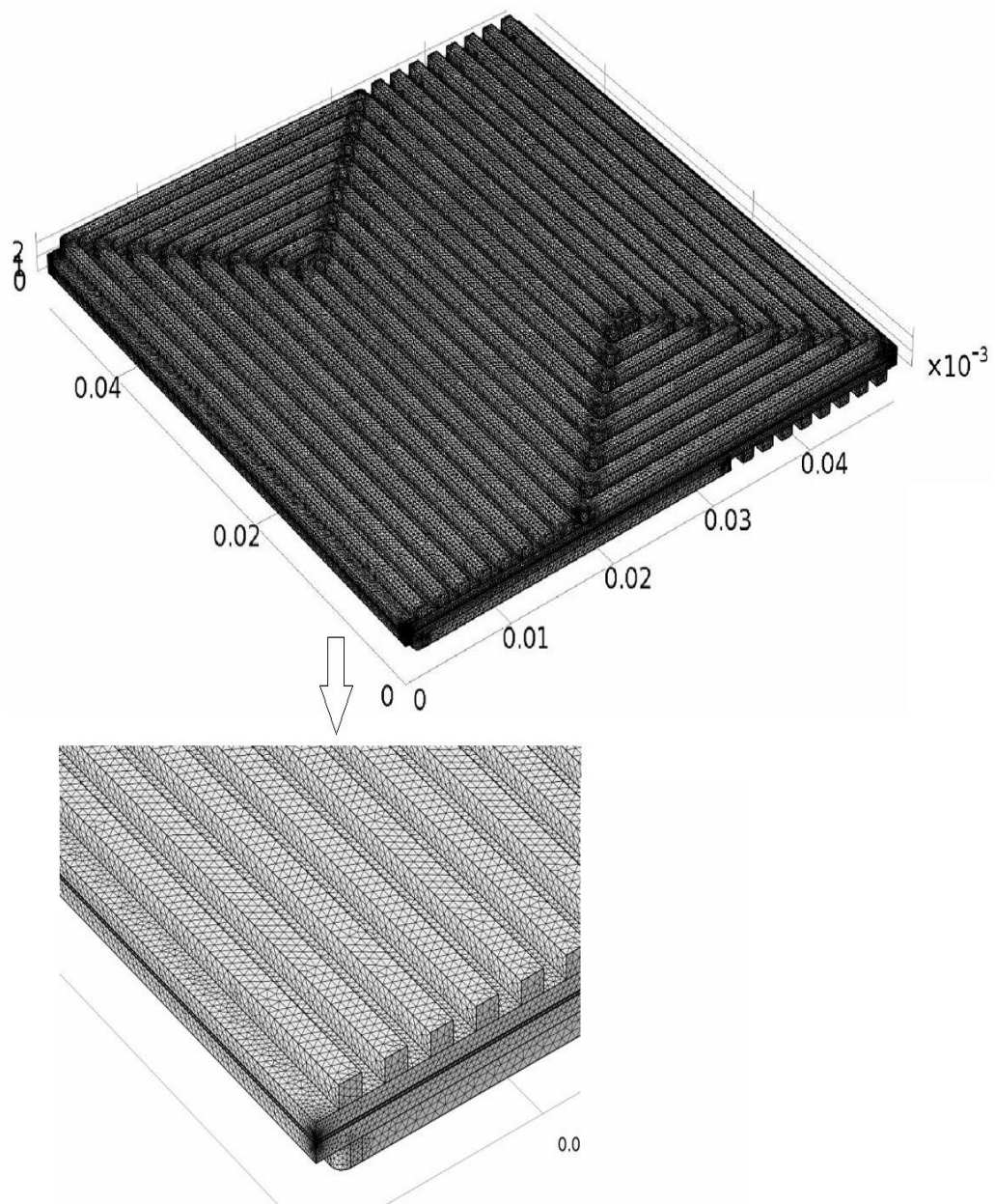
Figure D.2 Meshed computational domain for serpentine model

The solvers used in the solution of the mathematical models is based on "Direct" methods, which uses Lower Upper (LU) decomposition method for the matrices. Direct methods have several solver such as MUMPS, PARDISO and SPOOLES. PARDISO and SPOOLES sparse direct linear solver running in parallel, whereas MUMPS takes the advantage of shared memory parallelism. MUMPS and PARDISO solvers benefit from available disk space to solve large models not fitting in the available memory. Cluster computing is supported by MUMPS solver. There

is no need for large amount of RAM for direct solvers; however, MUMPS and PARDISO have the property of storing the solution out-of-core. In other words, a part of the problem can be offloaded onto the hard disk. For the finite element problems, the main advantage of these solvers is to obtain the same answer for the well-conditioned ones. For this reason, it does not differ which solver is chosen. The difference between the solvers is their relative speed. Therefore, in this study MUMPS solver is used for the solution of finite element problem [66].